

TESTING NEW WEAK LENSING MEASUREMENT TECHNIQUES WITH THE  
DARK ENERGY SURVEY

Christina Irene Krawiec

A DISSERTATION

in

Physics and Astronomy

Presented to the Faculties of the University of Pennsylvania

in Partial Fulfillment of the Requirements for the Degree of Doctor of Philosophy

2018

Supervisor of Dissertation

Graduate Group Chairperson

---

Gary Bernstein  
Reese W. Flower Professor of Astronomy and  
Astrophysics

---

Joshua R. Klein  
Edmund J. and Louise W. Kahn Professor of  
Physics and Astronomy

Dissertation Committee:

Cullen Blake, Assistant Professor of Physics and Astronomy

Adam Lidz, Associate Professor of Physics and Astronomy

Masao Sako, Associate Professor of Physics and Astronomy

Evelyn Thomson, Associate Professor of Physics and Astronomy

*For Frank, my partner in all things; and for my parents, who made all  
things possible.*

# Acknowledgments

I would like to thank my advisor Gary Bernstein, who has been nothing but kind and supportive during my graduate career, for his guidance in completing this dissertation. I also would like to thank my thesis committee: Cullen Blake, Adam Lidz, Masao Sako, and Evelyn Thomson, for taking their valuable time to review my work and attend my defense.

I am also very grateful to the members of the Dark Energy Survey who have helped me make use of such a wonderful dataset over the past five years. I especially thank my collaborators Arya Farahi, Ravi Gupta, Andrés Plazas, and Rachel Wolf, who care deeply about education and outreach and put forth a great effort to conduct research that will be meaningful to future science collaborations.

I would also like to acknowledge my wonderful officemates who have supported me emotionally through the years with plenty of laughter and boosts of confidence. Thanks Ashley Baker, Alyssa Barlis, Dillon Brout, Johanna-Laina Fischer, John Fischer, Saul Kohn, Jessie Taylor, and Rachel Wolf.

I am grateful for the faculty and postdocs in the Physics & Astronomy department at the University of Pennsylvania for providing an environment in which to learn and grow as a scientist.

And none of my work at Penn could have been completed without the love and encouragement of my fiancé Frank and my family - Chip, Laurie, Stephanie, and Theresa.

## ABSTRACT

### TESTING NEW WEAK LENSING MEASUREMENT TECHNIQUES WITH THE DARK ENERGY SURVEY

Christina Krawiec

Gary Bernstein

In this dissertation, we first present an analysis on the effect of wind at the Blanco Telescope, the home of the Dark Energy Camera (DECam), on Dark Energy Survey (DES) image quality. We find it to have a likely negligible impact on the weak gravitational lensing measurements conducted with images taken during high wind.

We then present the methods and validation of two new techniques in weak lensing shear and magnification measurement. We demonstrate highly accurate recovery of weak gravitational lensing shear using an implementation of the Bayesian Fourier Domain (BFD) method, proposed by Bernstein and Armstrong [2014], extended to correct for selection biases. The BFD formalism is rigorously correct for Nyquist-sampled, background-limited, uncrowded image of background galaxies. We conduct initial tests of this code on  $\approx 10^9$  simulated lensed galaxy images and recover the simulated shear to a fractional accuracy of  $m = (2.1 \pm 0.4) \times 10^{-3}$ , substantially more accurate than has been demonstrated previously for any generally applicable shear measurement method.

We also introduce a new Bayesian method for selecting high-redshift galaxies and calculating their magnification around foreground lenses. We apply this method to galaxies from DES Science Verification (SV).

Finally, we share the results of a survey conducted with DES collaborators on the collaboration itself, in which we find positive attitudes towards education and public outreach (EPO) in physics and astronomy. We also provide recommendations for current and future surveys on how to increase EPO engagement by scientists.

# Contents

<b>Dedication</b>	ii
<b>Acknowledgments</b>	iii
<b>Abstract</b>	iv
<b>List of Tables</b>	viii
<b>List of Figures</b>	ix
<b>1 Introduction</b>	1
1.1 Cosmology . . . . .	1
1.1.1 Dark Energy . . . . .	2
1.2 Gravitational Lensing . . . . .	3
1.2.1 Shear . . . . .	8
1.2.2 Magnification . . . . .	9
1.2.2.1 Systematics . . . . .	12
1.2.3 High Redshift Sources . . . . .	13
1.2.3.1 Lyman-break Galaxies . . . . .	13
1.3 The Dark Energy Survey . . . . .	17
<b>2 Analyzing the Impact of Wind on DES Image Quality</b>	20
2.1 Introduction . . . . .	20
2.2 Data . . . . .	22
2.2.1 Anemometer . . . . .	22
2.2.2 Accelerometer . . . . .	23
2.2.3 Telescope Control System and Guider . . . . .	25
2.3 Results . . . . .	26
2.4 Conclusions . . . . .	28
<b>3 Testing the Bayesian Fourier Domain Shear Measurement Method</b>	31
3.1 Introduction . . . . .	31
3.1.1 How BFD Works . . . . .	33

3.1.2	Simplest case . . . . .	33
3.1.3	Detection and selection . . . . .	37
3.1.4	Galaxy populations: postage stamp case . . . . .	40
3.1.5	Poisson-distributed galaxies . . . . .	44
3.1.6	Sampling the template space . . . . .	45
3.2	Implementation . . . . .	47
3.2.1	Computational shortcuts . . . . .	48
3.2.2	$k$ -d tree algorithm . . . . .	48
3.2.3	Weights and PSFs . . . . .	50
3.3	Validation Tests . . . . .	51
3.3.1	Gauss tests . . . . .	52
3.3.2	GALSIM Tests . . . . .	52
3.4	Testing approximations . . . . .	56
3.4.1	Nyquist sampling . . . . .	57
3.4.2	Stationary noise . . . . .	57
3.4.3	Convex galaxies . . . . .	58
3.4.4	Uncrowded galaxies . . . . .	59
3.4.5	Weak lensing limit . . . . .	59
3.4.6	Noiseless, unlensed templates . . . . .	61
3.4.7	Complete template set . . . . .	62
3.5	Future developments . . . . .	63
3.5.1	Interferometric data . . . . .	63
3.5.2	Multi-image analysis and multi-band data . . . . .	63
3.5.2.1	Multiple observing bands . . . . .	64
3.5.3	Star-galaxy discrimination . . . . .	65
3.5.4	Magnification . . . . .	66
3.5.5	Lensing tomography and photometric redshifts . . . . .	67
3.6	Conclusion . . . . .	70
3.7	BFD on DES . . . . .	74

<b>4</b>	<b>A New Method for Measuring the Cosmic Magnification of High Redshift Galaxies</b>	<b>78</b>
4.1	Magnification in the Dark Energy Survey . . . . .	79
4.2	Source Selection . . . . .	81
4.3	Testing the Bayesian Source Selection . . . . .	82
4.3.1	Flux Errors . . . . .	83
4.3.2	Probability Accuracy . . . . .	85
4.4	Object Classification . . . . .	87
4.5	Obtaining $P(H G)$ and $k$ . . . . .	89
4.6	Estimating Magnification $\mu(\theta)$ . . . . .	90
4.7	Conclusion . . . . .	91

<b>5 Magnification of High Redshift Galaxies in the Dark Energy Survey</b>	<b>97</b>
5.1 Previous DES WL Results . . . . .	97
5.2 Targets: SVA1 Gold . . . . .	99
5.3 Templates . . . . .	100
5.3.1 Stars . . . . .	101
5.4 Target Classification . . . . .	102
5.5 BALROG . . . . .	103
5.6 Results . . . . .	106
5.7 Discussion . . . . .	108
<b>6 Astronomers' and Physicists' Attitudes Towards Education &amp; Public Outreach: A Case Study with The Dark Energy Survey</b>	<b>111</b>
6.1 Introduction . . . . .	111
6.2 Methods . . . . .	114
6.2.1 Survey Structure . . . . .	114
6.2.2 Respondents . . . . .	115
6.3 Results . . . . .	118
6.3.1 Types of Engagement and Time Commitment to EPO . . . . .	118
6.3.2 Motives and Deterrents . . . . .	122
6.3.3 Centralization . . . . .	124
6.3.3.1 Views of EPO Across the DES Collaboration . . . . .	125
6.3.3.2 Centralized Support for EPO Engagement . . . . .	127
6.4 Conclusions . . . . .	128
<b>Appendices</b>	<b>134</b>
<b>Appendices</b>	<b>134</b>
<b>A Full list of survey item options for responses presented in Figures 6.3 and 6.4.</b>	<b>135</b>
<b>Bibliography</b>	<b>138</b>

# List of Tables

3.1	Parameters and results of the baseline validation tests . . . . .	53
5.1	The six groups of redshift ranges and number of templates for each group.	101
5.2	. . . . .	102
5.3	$k_{HG} = \frac{d \log n_H}{d \mu_G}$ calculated by counting the change in the number of SIM objects in each class $H$ when input BALROG objects with matched COSMOS photo-z in $z_G$ are artificially magnified. . . . .	107
5.4	$P(H G)$ measured from the D10/DFULL/COSMOS matched field for each $H/G$ pair. . . . .	107
6.1	Current (a) and desired (b) time commitment to EPO. . . . .	121
6.2	Responses for the Likert survey item: “Rank how much you think the following DES groups value EPO.” Respondents were asked to rank on a 5-point scale: 1=“Very Little” to 5=“Very Much.” Respondents were also given the opportunity to answer “I Don’t Know.” Percentages listed in the table correspond to the fraction from the total responses using the Likert scale only. . . . .	126
A.1	Complete list of possible answers for the survey item presented in Figure 6.3. Responses are listed in descending order, i.e., A1 was the most popular response, rather than the order in which they were presented in the survey item. . . . .	136
A.2	Complete list of possible answers for the survey item presented in Figure 6.4. Responses are listed in descending order, i.e., B1 was the most popular response, rather than the order in which they were presented in the survey item. . . . .	137

# List of Figures

1.1	The light we see from distant objects shows us how the universe was at different times in the past. . . . .	4
1.2	Schematic of the light path distortion from gravitational lensing. (Image: one-minute astronomer) . . . . .	4
1.3	Figure from Bartelmann and Schneider [2001] detailing the source-lens-observer system for gravitational lensing. . . . .	5
1.4	The effects of convergence and shear in isolation. Figure from Bartelmann and Narayan [1995]. . . . .	6
1.5	The galaxy cluster Abel 2218 lenses several background galaxies which appear as arcs in this image. . . . .	7
1.6	The effect of magnification bias on galaxy number counts. . . . .	10
1.7	Simulated $z = 3.15$ LBG spectrum [Giavalisco, 1998]. Here, the Lyman break is observed at $912 \text{ \AA} \times (1+z) \approx 3800 \text{ \AA}$ . . . . .	15
1.8	Figure from Morrison et al. [2012]. LBG selection for B-dropouts in the Deep Lens Survey (DLS) is shown here by the black bounding box. The three tracks denoted by $\beta$ show model LBGs with different UV continuum slopes at redshifts indicated along the track. Density contours are DLS galaxies with a B-band S/N > 2 detection. Green points are stars detected in DLS. The black track is the evolution of an elliptical galaxy template from redshift $0 < z < 2$ . The blue track is a sample quasar spectrum redshifted from $z = 3\text{-}5$ . . . . .	16
1.9	(Images: Reidar Hahn, Fermilab) . . . . .	18
1.10	DES observing strategy [Abbott et al., 2016]. . . . .	19
2.1	The anemometer (inset) and its position and orientation (blue arrow) on the telescope. . . . .	23
2.2	Two different nights in anemometer data. . . . .	24
2.3	Photos by Kevin Reil. . . . .	25
2.4	The process for converting the unfiltered voltage readings from the accelerometer into the actual displacement incurred on the telescope. . . . .	25
2.5	The night of May 9th, 2014. . . . .	27
2.6	Total rms displacements vs. rms wind speeds for each exposure included in this study. The median values are shown in black. . . . .	28

2.7	.....	30
3.1	A sample of the target (left) and template (right) simulated galaxies used in the validation test. Targets are marked here with an X in the upper left of their stamp if they were cut for low (red) or high (blue) $S/N$ . . . . .	54
3.2	The recovered multiplicative bias using the second-order BFD formalism, as a function of input shear. The grey band shows the desired accuracy of $m < 10^{-3}$ . The dashed line is a fit of the data to the expected quadratic dependence on $g$ , with coefficient $\alpha \approx 2$ for the Gauss tests and $\alpha \approx 0.5$ for the GALSIM tests. . . . .	61
3.3	Top: the multiplicative bias in shear inferred from simulations where we add noise to the template galaxies. The $x$ axis gives the noise variance on the templates relative to the noise variance on the target observations. Bottom: the multiplicative bias recovered when template galaxies have an applied shear that is either constant or drawn from a Gaussian of given RMS value. The grey band shows the desired accuracy of $m < 10^{-3}$ , which we see is retained when the templates have $\lesssim 10\%$ of the noise power of the targets, and the RMS shear on templates is $\lesssim 0.04$ . . . . .	75
3.4	The multiplicative bias recovered as a function of the number of initial template galaxies before adding rotated/translated copies (top) and as a function of $N_{\text{sample}}$ (bottom), the number of subsampled templates used to evaluate the integrals for each target galaxy. The grey band shows the desired accuracy of $ m  < 10^{-3}$ . . . . .	76
3.5	The number of templates used in the integration of $P(D_i g)$ for each galaxy as a function of its flux moment $M_f$ in the GALSIM tests. The central line is the median, the shaded region bounds the 10–90 percentile range. . . . .	77
4.1	DES throughput overlaid with the Lyman break at various redshifts. . . . .	79
4.2	Figures from Davies et al. [2013] showing the simulated color tracks for massive galaxies at high redshifts compared to those of various nearby galaxies and stars in DES. . . . .	80
4.3	Histograms of D04/D10 flux deviation from DFULL in units of reported flux error. The dotted line is a $1\sigma$ Gaussian distribution, i.e. what we expect if DFULL is the true flux, and the errors are reported exactly correctly. . . . .	84
4.4	Custom error distribution (shown in blue) of the mock catalog used to test the assumptions made in the posterior probability calculation. It differs in shape from a $1\sigma$ Gaussian distribution (shown in black) in a manner exaggerated from that found in the real data. . . . .	86
4.5	.....	92
4.6	Posterior probability accuracy for objects in the DES D10 catalog when the prior consists of their counterparts in the matched DFULL/COSMOS catalog. . . . .	93

4.7	DES $g - r$ vs. $r - i$ (a) and $r - i$ vs. $i - z$ (b) for objects in our DFULL/COSMOS matched catalog, colored by their ZMINCHI2 value. . . . .	93
4.8	DES $g - r$ vs. $r - i$ for objects in the D10 catalog. Each panel's points are colored according to their posterior probability of membership in different redshift bins ( $P[z_{min}, z_{max}]$ ). . . . .	94
4.9	DES $r - i$ vs. $i - z$ for objects in the D10 catalog. Each panel's points are colored according to their posterior probability of membership in different redshift bins ( $P[z_{min}, z_{max}]$ ). . . . .	95
4.10	Left: Objects labeled by their true redshift (these are unknown to us). Right: The same objects classified into groups $A$ , $B$ , and $C$ (low, medium, and high redshift classes) by some combination of their posterior probabilities. Not all objects will be classified into the correct group, i.e. a red object may be classified as group $A$ despite being at very high $z=5.1$ . . . . .	96
5.1	Spectroscopic vs. photometric redshifts for a subset of the redMaGiC catalog. Figure from Rozo et al. [2016]. . . . .	98
5.2	Figure from Clampitt et al. [2017]. Left: Differential surface mass density $\Delta\Sigma$ measured from WL shear around redMaGiC lenses in three redshift bins (as labeled). Best-fit model curves are also shown for each sample. Right: The same, but showing the tangential shear $\gamma_t$ . . . . .	98
5.3	Figure from Garcia-Fernandez et al. [2018]. Measured two-point angular cross-correlation functions for the samples $r < 23.0$ , $i < 22.5$ and $z < 22.0$ , left to right respectively. Dots use the optimal weighting [Scranton et al., 2005], where each galaxy is weighted by its corresponding $\alpha(m) - 1$ value, whereas squares are equally weighted. The green line is their theoretical prediction. The red dashed line is zero. . . . .	99
5.4	Density of objects in the SVA1 Gold Catalog. . . . .	101
5.5	DES $g - r$ vs. $r - i$ for the SVA1 Gold targets that pass the probability cuts for each class as described in Table 5.2. . . . .	103
5.6	DES $r - i$ vs. $i - z$ for the SVA1 Gold targets labeled by their classifications as described in Table 5.2. . . . .	104
5.7	Figure from Suchyta et al. [2016]. The observed distributions of MAG_AUTO $gr$ magnitudes in the BALROG SIM catalog compared with those in DES SV. . . . .	105
5.8	Angular two-point correlation functions for the five target classes and red-MaGiC lenses. . . . .	108
5.9	Estimated magnification for each of the source galaxy types. . . . .	109
6.1	Demographic information for study respondents. Here we display breakdowns by (a) gender, (b) age, (c) ethnicity, and (d) current position as self-reported in the survey. . . . .	117

6.2	Respondents were presented with 19 activities and asked 1) if they have ever engaged in the activity and 2) to rank its value (level of impact). “Value of Activity” is calculated from Eq. 6.1. The number of counted responses, $n$ , is noted in white (out of a total 131 respondents). . . . .	120
6.3	Distribution of checked motivating factors towards EPO engagement. Respondents were provided a list of possible motivating factors for EPO engagement and asked to check all that apply. Complete descriptions for provided list of factors, some of which are present in the legend, are given in Table A.1. . . . .	123
6.4	Distribution of checked factors which would encourage future EPO engagement. Respondents were provided with a list of possible incentives to encourage participation in EPO activities and asked to check all which might increase their motivation. Respondents could also write in their own responses; these have been combined into the “Other” category. Complete descriptions for provided list of factors, some of which are present in the legend, are given in Table A.2. . . . .	125

# Chapter 1

## Introduction

With every passing decade, we get closer to accurately describing the history and composition of the universe. The tools with which we look up and out have become more precise thanks to new technologies. We thus live in an exciting time for cosmological exploration. This dissertation seeks to explore just one piece of the puzzle of our existence.

### 1.1 Cosmology

The modern era of cosmology began in 1915 with Albert Einstein's publication of his theory of General Relativity. In it, he linked the curvature of spacetime - the dimensions of space and time that make up the universe - with its mass-energy content. Then, in 1922, Alexander Friedmann developed a set of equations that allows for the expansion or contraction of the universe, depending on the energy content  $\varepsilon(t)$  and curvature  $k$ :

$$\left(\frac{\dot{a}}{a}\right)^2 = \frac{8\pi G}{3c^2} \varepsilon(t) - \frac{kc^2}{R_0^2} \frac{1}{a(t)^2}, \quad (1.1)$$

where  $R_0$  is the radius of curvature of the universe, and  $a(t)$  is called the *scale factor*. We can write the actual, *proper*, distance to any object in the universe as a function of the scale factor and the *comoving* distance ( $\chi$ , which we will define later) as:

$$d_p(t) = a(t)\chi. \quad (1.2)$$

Edwin Hubble's measurement of redshift versus distance confirmed that the universe was in fact expanding in 1929. We call the factor  $H(t) \equiv (\frac{\dot{a}}{a})$  the *Hubble parameter*, which quantifies this expansion in terms of the scale factor and its time derivative. The evolution of the energy density of a given fluid is related to the Hubble parameter:

$$\Omega(t) \equiv \frac{\epsilon(t)}{\epsilon_{crit}(t)}, \quad (1.3)$$

where the *critical density* is

$$\epsilon_{crit}(t) \equiv \frac{3c^2}{8\pi G} H^2(t). \quad (1.4)$$

### 1.1.1 Dark Energy

The energy content that defines this temporal behavior consists of three main forms: radiation (relativistic particles like photons), non-relativistic matter (both baryonic and "dark"), and a *vacuum* energy. The equation of state for each of these forms of energy relates its pressure to its density,

$$w = \frac{P}{\rho}. \quad (1.5)$$

Each of the aforementioned forms of energy has its own equation of state parameter,  $w$ . We know from thermodynamics that  $w_{rad} = 1/3$  and  $w_{mat} \approx 0$ . But twenty years ago it was discovered that our universe is not only expanding, but expanding at an accelerated rate. This kind of expansion is predicted only for an energy with an equation of state parameter  $w < -\frac{1}{3}$ . This vacuum energy opposes gravity, and the current predicted value is  $w_\Lambda = -1$ , where  $\Lambda$  denotes the "cosmological constant" and refers to the constant energy density of the vacuum of space. We refer to the cause of this constant as "dark energy." Using Equation 1.1, we can then describe our universe as a function of radiation, matter, and dark energy densities:

$$\frac{H^2(t)}{H_0^2} = \frac{\Omega_{rad,0}}{a^4(t)} + \frac{\Omega_{mat,0}}{a^3(t)} + \Omega_{\Lambda,0} + \frac{1 - \Omega_0}{a^2(t)}. \quad (1.6)$$

where  $\Omega_0 = \Omega_{rad,0} + \Omega_{mat,0} + \Omega_{\Lambda,0}$ , and  $\Omega_0 = 1$  indicates a flat universe. The comoving distance to an object at a redshift  $z$  is then

$$\chi(z) = \frac{c}{H_0} \int_0^z \frac{dz'}{\sqrt{\Omega_{mat}(1+z')^3 + (1-\Omega_0)(1+z')^2 + \Omega_\Lambda}}. \quad (1.7)$$

Through the measurement of the distribution and proper distance (related to cosmology through  $\chi$  and the scale factor, see Equation 1.2) of matter densities in the universe, we can estimate the  $\Omega$  parameters described above and compare them with the predictions of various theories of cosmology - i.e. those where  $k \neq 0$  or modified gravity theories that differ from General Relativity.

Measuring this mass/energy distribution at different epochs requires telescopes with great power and precision, since objects at the earliest times are the hardest to resolve. But several important evolutionary periods occurred at these early times, as seen in Figure 1.1. And dark energy and dark matter, the dominant energies at present, are now the mysteries foremost on the minds of cosmologists, and measuring galaxy formation and evolution can teach us about their source and composition. This is the target of many astronomical surveys today. We can use several techniques to accomplish this task – such as using Type 1a supernovae to calculate distances, measuring the mass function of galaxy clusters, and gravitational lensing. The latter is one of the only tools we have to map dark matter, which does not radiate light but still interacts gravitationally.

## 1.2 Gravitational Lensing

An important prediction of General Relativity is that light from distant objects will be deflected by the gravitational potential of massive objects. We call this phenomenon "gravitational lensing." Photons follow the shortest possible distance as they propagate through spacetime. This means that observers on Earth will see light coming from locations different from those at which it was originally radiated, as demonstrated in Figure 1.2. When looking at a two-object system, the background object whose light path is distorted is called the "source," and the plane in which it lies the "source plane." Simi-

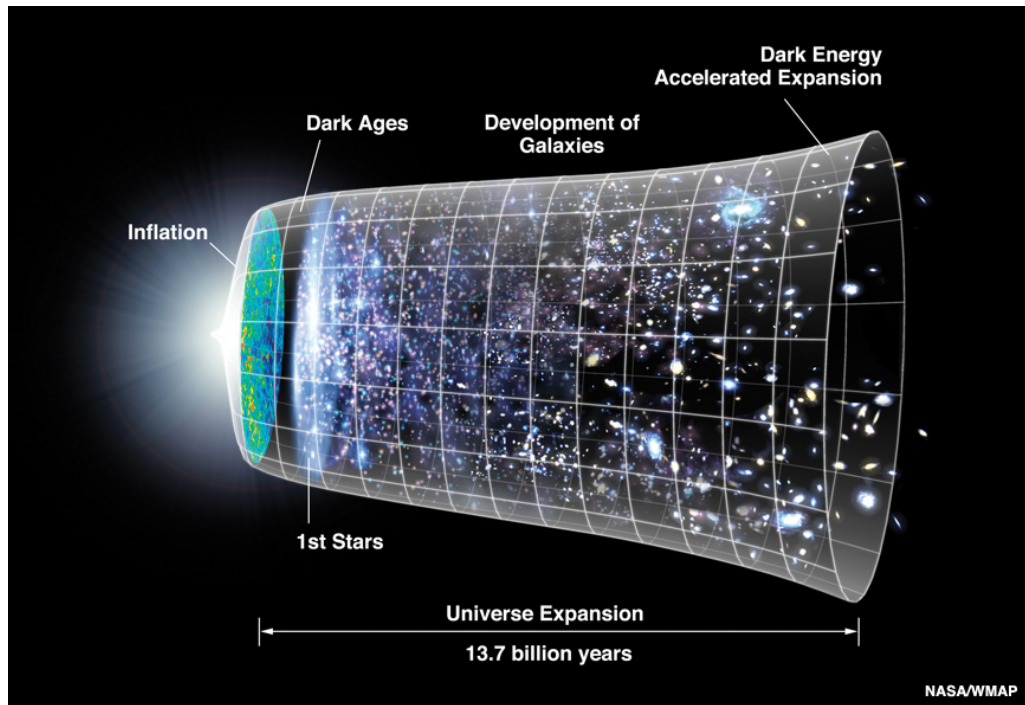


Figure 1.1: The light we see from distant objects shows us how the universe was at different times in the past.

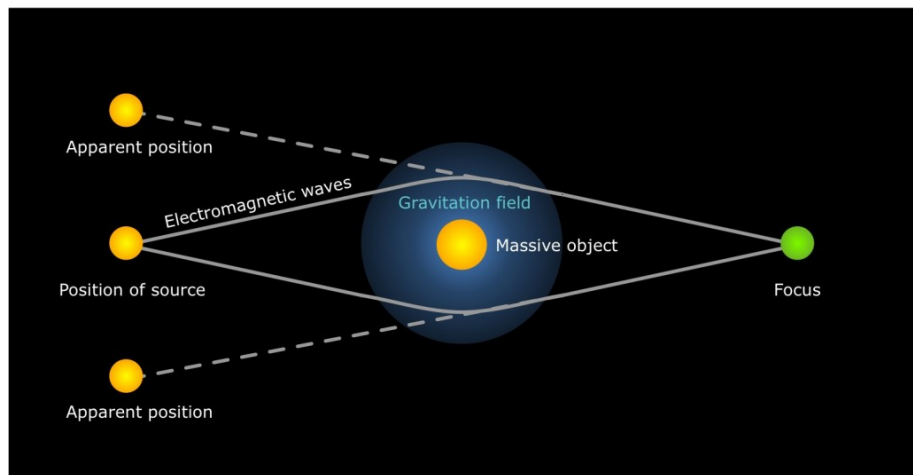


Figure 1.2: Schematic of the light path distortion from gravitational lensing. (Image: one-minute astronomer)

larly, the foreground object is called the "lens," and the plane at which we observe the source object's light the "image plane," as shown in Figure 1.3. Following the notation in

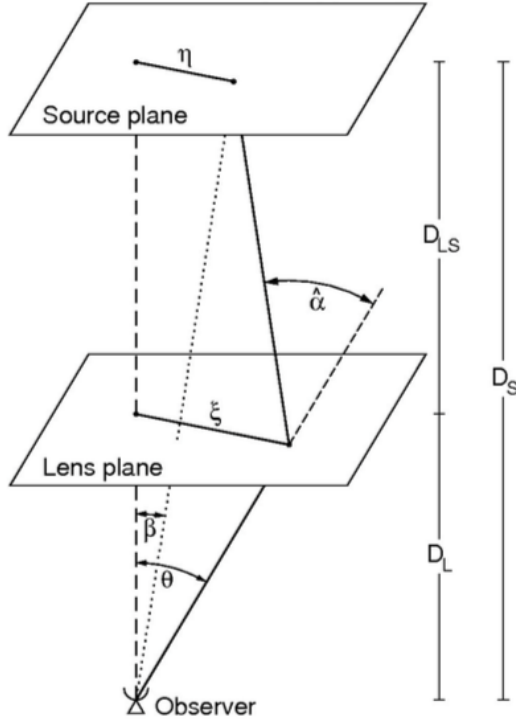


Figure 1.3: Figure from Bartelmann and Schneider [2001] detailing the source-lens-observer system for gravitational lensing.

this figure, we can describe the relation between the source and image planes due to the intervening mass:

$$\vec{\beta} = \mathbf{A} \cdot \vec{\theta} \quad (1.8)$$

$$\mathbf{A} = \begin{bmatrix} 1 - \kappa + \gamma_1 & -\gamma_2 \\ -\gamma_2 & 1 - \kappa - \gamma_1 \end{bmatrix} \quad (1.9)$$

where  $\vec{\beta}$  describes the source position and  $\vec{\theta}$  describes the image position, and  $\mathbf{A}$  is a Jacobian matrix with components  $\kappa$  and  $\vec{\gamma} = (\gamma_1, \gamma_2)$ , called convergence and shear respectively, that relate to the masses and distances of the system. These components depend on the surface mass density of the lens, which is equal to its three-dimensional mass profile flattened in the line-of-sight direction:

$$\Sigma(R) = \int \rho(R, z) dz. \quad (1.10)$$

The convergence and shear are related to this surface mass density as follows:

$$\kappa(\vec{\theta}) = \frac{\Sigma(D_l \vec{\theta})}{\Sigma_{crit}}, \quad (1.11)$$

and for a circularly symmetric lens,

$$\gamma(\vec{\theta}) = \frac{\bar{\Sigma}(D_l \vec{\theta}) - \Sigma(D_l \vec{\theta})}{\Sigma_{crit}} \quad (1.12)$$

where  $D_l$  is the angular diameter distance to the lens, which for a flat universe is related to the comoving distance  $\chi$  as such:

$$D = \frac{\chi(z)}{1+z}, \quad (1.13)$$

and  $\Sigma_{crit}$  is the "critical mass density" of the observer-lens-source system:

$$\Sigma_{crit} = \frac{c^2}{4\pi G D_{ls} D_l}. \quad (1.14)$$

Thus if we can quantify the convergence and shear of sources at different radii from a foreground lens, we have an estimate of the radial mass profile of said lens.

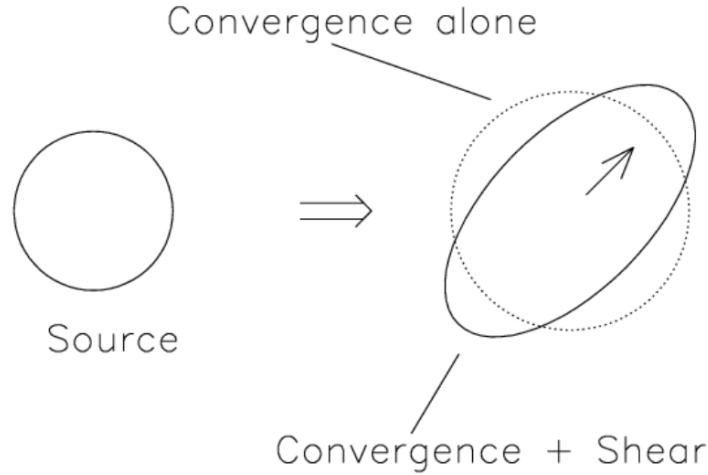


Figure 1.4: The effects of convergence and shear in isolation. Figure from Bartelmann and Narayan [1995].

How can we estimate these effects? The convergence and shear distort the source image as shown in Figure 1.4. The isotropic vs. anisotropic effects can be made more clear if we rewrite the distortion matrix  $\mathbf{A}$  as

$$\mathbf{A} = (1 - \kappa) \begin{bmatrix} 1 & 0 \\ 0 & 1 \end{bmatrix} - \gamma \begin{bmatrix} \cos 2\phi & \sin 2\phi \\ \sin 2\phi & -\cos 2\phi \end{bmatrix}. \quad (1.15)$$

where  $\gamma = \sqrt{\gamma_1^2 + \gamma_2^2}$  and  $\phi$  is the position angle of the image. If we can measure the change in size and shape of a galaxy image due to lensing alone, we can estimate  $\kappa$  and  $\vec{\gamma}$  and relate them back to the mass profile of the lens, and possibly make estimates of the geometry of the universe through the comoving distances involved. Not only can we

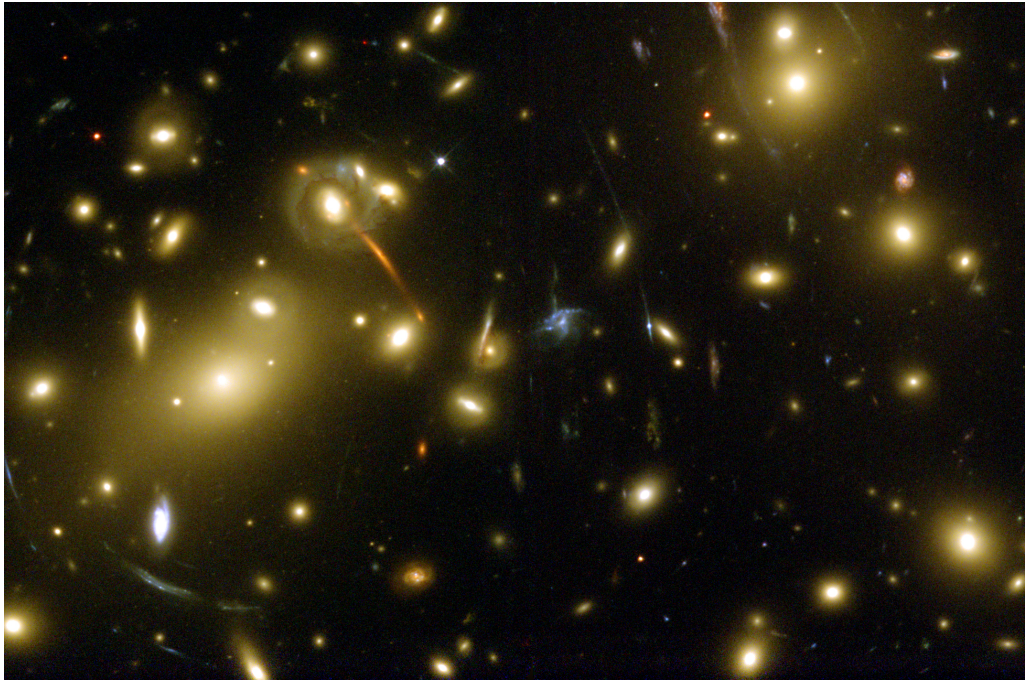


Figure 1.5: The galaxy cluster Abel 2218 lenses several background galaxies which appear as arcs in this image.

measure the radial mass profiles of large structures like clusters, using the strong distortion of galaxies behind them as in Figure 1.5, we can also make statistical measurements using much weaker distortions. We refer to the limit where  $\kappa, \gamma \ll 1$  as the regime of "weak

lensing." In this regime, the magnification of a source can be approximated as such:

$$\mu = \frac{1}{\det A} = \frac{1}{(1 - \kappa)^2 - \gamma^2} \approx 1 + 2\kappa \quad (1.16)$$

and the shear can be approximated by the "reduced shear" -

$$\vec{g} = \frac{\vec{\gamma}}{(1 - \kappa)} \approx \vec{\gamma} \quad (1.17)$$

which represents the shape change while ignoring size.

For an ensemble of sources, the average ellipticity in the absence of lensing should be zero since there is no preferred orientation of galaxy inclinations with respect to the observer. For a circular source with unit radius, the ellipticity of its image after lensing has semi-major and -minor axes  $a = (1 - \kappa - \gamma)^{-1}$  and  $b = (1 - \kappa + \gamma)^{-1}$  respectively. The expectation of the ellipticity is then directly related to the reduced shear:

$$\langle \epsilon \rangle = \left\langle \frac{1 - \frac{b}{a}}{1 + \frac{b}{a}} \right\rangle \approx \left\langle \frac{\gamma}{1 - \kappa} \right\rangle = \langle g \rangle. \quad (1.18)$$

The ellipticity of a galaxy image is therefore an unbiased estimate of the shear. Once estimated through magnification and ellipticity measurements, correlations of  $\kappa$  and  $\vec{\gamma}$  with galaxy mass can be compared directly to theory through the mass-density power spectrum of the universe which depends on the cosmological parameters  $\Omega_{mat}$  and  $\Omega_\Lambda$  and also  $\sigma_8$ , the amplitude of mass fluctuations on an 8 Mpc/h scale. These comparisons can help us differentiate between universes as noted in the previous section.

We will now discuss how we can estimate shear and magnification separately, as each type of analysis involves very different expectations and systematics.

### 1.2.1 Shear

Traditionally, shear measurements are the main product of weak lensing studies. As mentioned, shear estimators typically rely on some calculation of galaxy ellipticity. The biggest uncertainty in this calculation is the shape noise - the intrinsic galaxy ellipticity distribution has rms values of 0.3-0.4 [Casaponsa et al., 2013]. But we also would

like to limit the *cosmic* variance, an uncertainty arising due to how the mass density, and thus lensing, fluctuates across the sky. We therefore need numerous sources, preferably over a large continuous patch of sky. Because we need so many source galaxies to get a statistically significant measurement of lensing shear, analyses focusing on weak lensing only became possible during the 1990's when telescope/survey technology permitted this task. Over the years there have been a series of simulations to test shear measurement techniques such as the GREAT(3,08,10) challenges [Bridle et al., 2009]. Commonly, the competing techniques involve finding the maximum likelihood of shear given measured galaxy ellipticities. We present a new technique for shear measurement that differs from the mainstream estimations in Chapter 3.

As sources get more distant, their shapes become less resolvable. For analyses at high redshift, magnification estimation becomes more profitable, as only size and flux information are needed. Other systematics also become less important, and if magnification and shear can be measured for the same set of lenses, some degeneracies in the lensing estimation can be broken by their combination.

### 1.2.2 Magnification

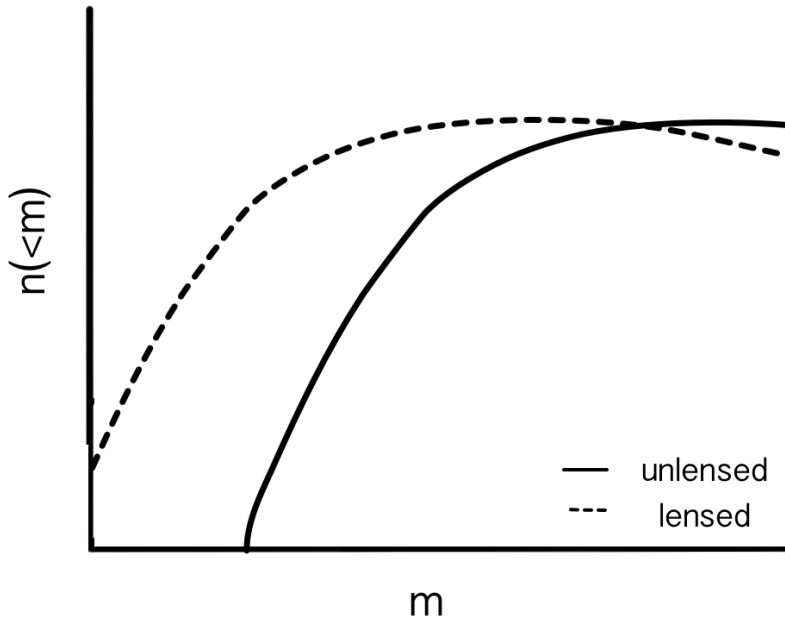
Magnification causes an increase in the surface area of the source. Since surface brightness is conserved in lensing, the flux changes accordingly. Changes in either the flux or size of sources can be measured to estimate magnification. "Magnification bias" is the resulting amplification or reduction in source number density due to these changes. It is a function of the source magnitude,

$$n(< m, \theta) = \mu(\theta)^{\alpha(m)-1} n_0(< m), \quad (1.19)$$

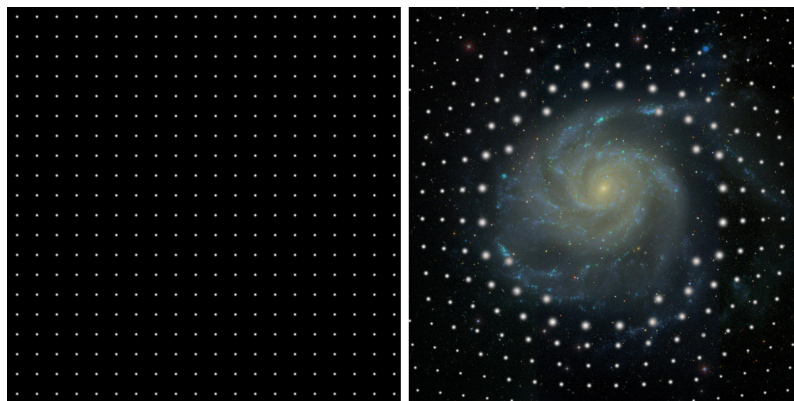
where  $n_0(< m)$  is the unlensed number density of galaxies brighter than  $m$ , and

$$\alpha(m) = 2.5 \frac{d \log n(m)}{dm}. \quad (1.20)$$

The effect of this bias is illustrated in Figure 1.6. Since the number density is altered



(a) The increase in flux and solid angle causes changes in the observed number density of galaxies around lenses. Brighter galaxies will appear more numerous, while fainter ones will be sparser depending on the detection limit of the survey.



(b) For a grid of point-like sources, a foreground lens will act to spread out the light, making them appear larger, brighter, and sparser. (Image: Joerg Colberg, Ryan Scranton, Robert Lupton, SDSS)

Figure 1.6: The effect of magnification bias on galaxy number counts.

around foreground lens galaxies, a correlation  $w_{ls}(\theta)$  is induced between the lenses and sources that relates to the magnification  $\mu(\theta)$ ,

$$w_{ls}(\theta) = \frac{n_s(\theta)}{\langle n_s \rangle} - 1 = \mu(\theta)^{\alpha(m)-1} - 1, \quad (1.21)$$

where the number density of sources  $n_s(\theta)$  is described by Equation 1.19. Taylor expanding in the weak lensing limit gives:

$$w_{ls}(\theta) \approx (\alpha(m) - 1)(\mu(\theta) - 1) \approx 2(\alpha(m) - 1)\kappa(\theta), \quad (1.22)$$

which shows  $w_{ls}(\theta)$  is proportional to  $\kappa(\theta)$  and thus relates directly to the density distribution of the lensing mass.

However, the measurement of density, flux, and size changes due to magnification is complicated by several factors. While the average ellipticity of galaxies in the universe is expected to be zero, their average flux and size have intrinsic (unlensed) values that are harder to divine. This makes magnification measurements in general more noisy than those of shear, and for this reason magnification analyses have lagged behind in the literature. However, magnification does have *some* advantages over shear. For one, it is much harder to measure shapes and size at high redshift because their angular size becomes too small to be resolved. In the age of ever-increasing reach in astronomy, flux magnification becomes an appealing probe of matter at earlier epochs. Magnification and shear also have different radial dependencies on the spatial matter distribution, as shown in Equations 1.11 and 1.12. Since magnification can be used to make an independent measurement of the matter distribution, it may improve the cosmological constraints obtained with shear (Waerbeke [2010]; Rozo and Schmidt [2010]). Measurements of  $\kappa$  can be used to lift the mass-sheet degeneracy that exists when measuring the reduced shear – the addition of a constant "sheet" of mass to Equation 1.12 leaves the result unchanged. Thus one can obtain an estimation of local surface mass density from  $\mu + \vec{g}$  measurements, reducing uncertainty on the reconstruction of the matter distribution from shear alone [Jain, 2002]. The amplitude and angular shape of the cross-correlation function  $w(\theta)$

also contain information about cosmological parameters and the galaxy bias factor [Ménard and Bartelmann, 2002], which describes how well galaxy positions trace dark matter over-densities.

### 1.2.2.1 Systematics

A ground-based survey is not done all at once. Each exposure is taken with different *seeing* conditions, due to changes in the atmosphere, and varying aspects of the telescope arrangement. We quantify the effect of these elements on the shape and size of images using the point-spread function (PSF), a measure of how much images of point sources like stars are blurred by this complicated system. An analysis of how wind specifically can be detrimental to a ground-based telescope’s PSF is discussed in Chapter 2. The PSF can be anisotropic and masquerade as shear, so it is important to accurately measure and categorize it both temporally and spatially across the survey. Seeing affects shape and size more than flux, but flux measurements need accurate photometry. This, as well as accurate error estimation of these properties, can be important for source and lens selection, since redshift and flux are tightly related.

Galaxies can also appear denser in fields where the survey is deeper. For this reason it is important to account for survey depth when calculating correlations and galaxy counts. Moreover, lensing is not the only phenomenon that can cause correlations between background and foreground galaxies. Matter is not just randomly distributed in our universe – galaxies tend to cluster around other galaxies and can also have intrinsic alignments in their orientations. These are the exact signals we seek to disentangle from magnification and shear, respectively. If galaxies are sufficiently close in redshift, there will be a physical correlation in their positions that far exceeds (by an order of magnitude) the correlation induced by magnification. This places great importance on having a confidently separated set of lenses and sources. Photometric redshift distributions are most commonly used for this separation, and thus their reliability is of major concern to any lensing analysis. As with shear, we can choose certain lens and source populations

that minimize the risk of physical overlap. This can be easier with magnification since we can probe higher source redshifts.

### 1.2.3 High Redshift Sources

Let us explore some options for high redshift sources, since they may be beneficial to measuring a magnification signal. Lyman-break galaxies and quasars, for example, are good source candidates for measuring magnification because of their large distances (affecting  $\Sigma_{crit}$  as in Equation 1.14) and steep number densities (increasing  $\alpha(m)$ ). Several landmark studies have been conducted using each of these types of sources, which must be selected carefully to ensure they are at high redshift and not actually nearby stars – the other unresolved objects that litter the sky.

Scranton et al. [2005] were the first to measure cosmic magnification with a large sample of quasars from the Sloan Digital Sky Survey (SDSS). The ~200,000 quasars were selected using a binary quasar/star classifier, calculated by comparing the 4D SDSS colors to two training samples of each type. They further trimmed the sample to prevent physical correlations with lenses using photometric redshifts. They obtained an  $8\sigma$  measurement of cosmic magnification using a lens sample consisting of ~13 million galaxies over  $\sim 3800 \text{ deg}^2$ . The amplitude, angular dependence, and magnification bias matched theoretical expectations from the observed quasar number counts. They performed a series of checks to confirm systematics did not hamper the robustness of their measurement.

#### 1.2.3.1 Lyman-break Galaxies

Lyman-break Galaxies (LBGs) are young galaxies that existed in the early universe, and their light is thus strongly redshifted on its way to us. The robust star formation they host emits continuum radiation in the ultraviolet (UV) regime of the electromagnetic spectrum. LBGs are about an order of magnitude more numerous than quasars at the same flux level, but only recently have researchers been able to select these objects confidently [Steidel et al., 1996] and in great enough numbers [van der Burg et al., 2010] to use them for

reliable magnification measurements. Their selection depends on the existence of the "Lyman break" they are named for. This spectral break occurs at the Lyman limit - the wavelength at which neutral hydrogen absorbs all higher energy light, which is 912 Å in the rest frame. Any radiation with energy higher than the Lyman limit is attenuated by neutral Hydrogen in its path to observation – whether found surrounding the source galaxy itself or in intervening galaxies or clouds. The flux we observe from an object will appear truncated at the observed-frame energy of the limit, and this spectral plateau is called the Lyman break. These objects at high redshift will therefore tend to "drop out" of images taken with telescope filters whose bandwidth is blueward of the redshifted Lyman break. Their spectrum will remain somewhat flat at energies lower than the Lyman break, but colors including the dropout filter will be very red. For example, the LBG whose spectrum is shown in Figure 1.7 would be called a " $U_n$ -dropout," as its  $U_n$ -flux would be observed to be  $\approx 0$ . This feature makes LBGs easy to select in color-color space in the right circumstances, as they typically occupy a red corner where one can draw borders and select a mostly pure sample, as seen in Figure 1.8.

This method will obviously be complicated by naturally overlapping populations and objects whose errors cause them to scatter across this LBG border. For LBGs, the biggest concern comes from low redshift galaxies. The 4000 Å break that is found in spectra of nearby galaxies can mimic the Lyman break in high-redshift objects.

Hildebrandt et al. [2009b] claim the first detection of cosmic magnification of LBGs from the CFHTLS-Archive-Research Survey (CARS), a deep dataset compiled from the Canada-France-Hawaii Telescope Legacy Survey (CFHTLS). Using simulations that were created using the Stellar Population Synthesis (SPS) technique, they predicted the colors of high redshift LBGs and low redshift objects that may also be found in the survey. This allowed them to draw borders in  $ugriz$  color space where LBG selection efficiency was highest and low-redshift contamination was lowest. With this method they selected  $>80,000$  LBGs at redshifts  $z = 2.5 - 5$  in a total of four  $1 \text{ deg}^2$  fields. In the final correlation calculation, they remove potential physical correlations by avoiding lenses with

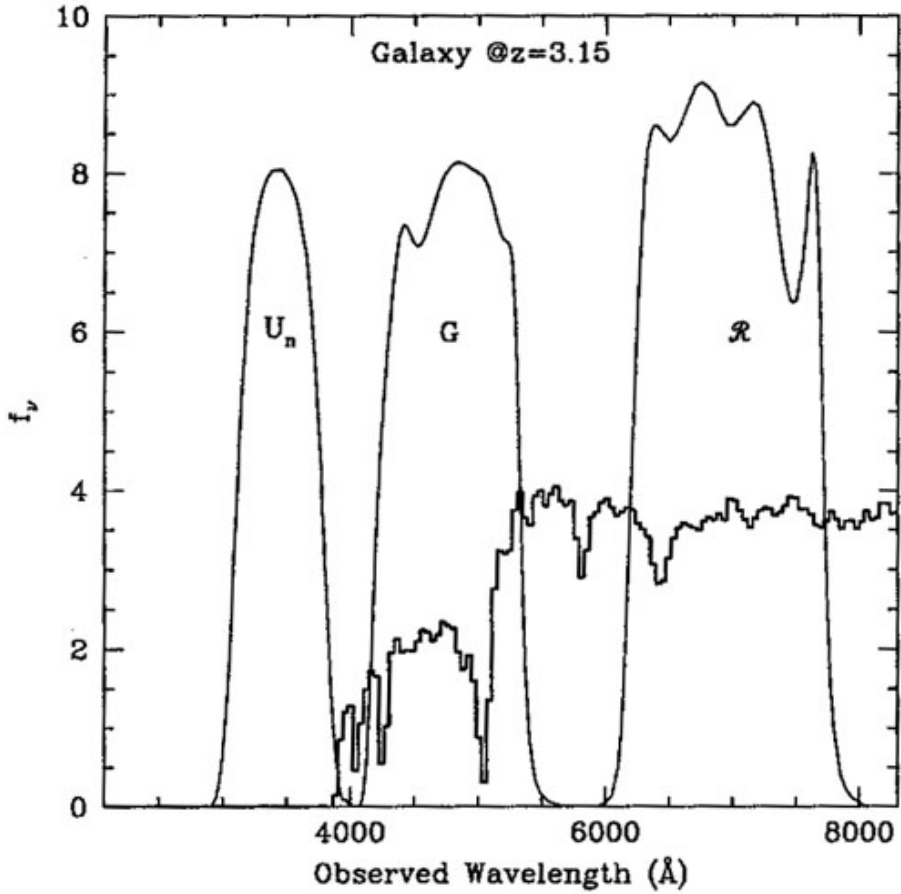


Figure 1.7: Simulated  $z = 3.15$  LBG spectrum [Giavalisco, 1998]. Here, the Lyman break is observed at  $912 \text{ Å} \times (1+z) \approx 3800 \text{ Å}$ .

photometric redshifts in the region most likely to contaminate the source LBG sample. They also conclude that the small remaining contaminants only contribute to noise in their signal because they are unaffected by lensing.

In a similar study, Morrison et al. [2012] made a measurement from five 4-deg<sup>2</sup> fields in the Deep Lens Survey (DLS). Using  $BVRz$  colors and simulated galaxy colors to select their cut region, they found  $\sim 12,000$  LBGs at redshift  $z \approx 4$ . They calculate the cross-correlation of these LBGs with  $\sim 450,000$  lenses, selected using photometric redshifts, resulting in a signal-to-noise ratio (SNR) greater than 20. They also separate the lenses into redshift bins for a tomographic measurement of the magnification, allowing

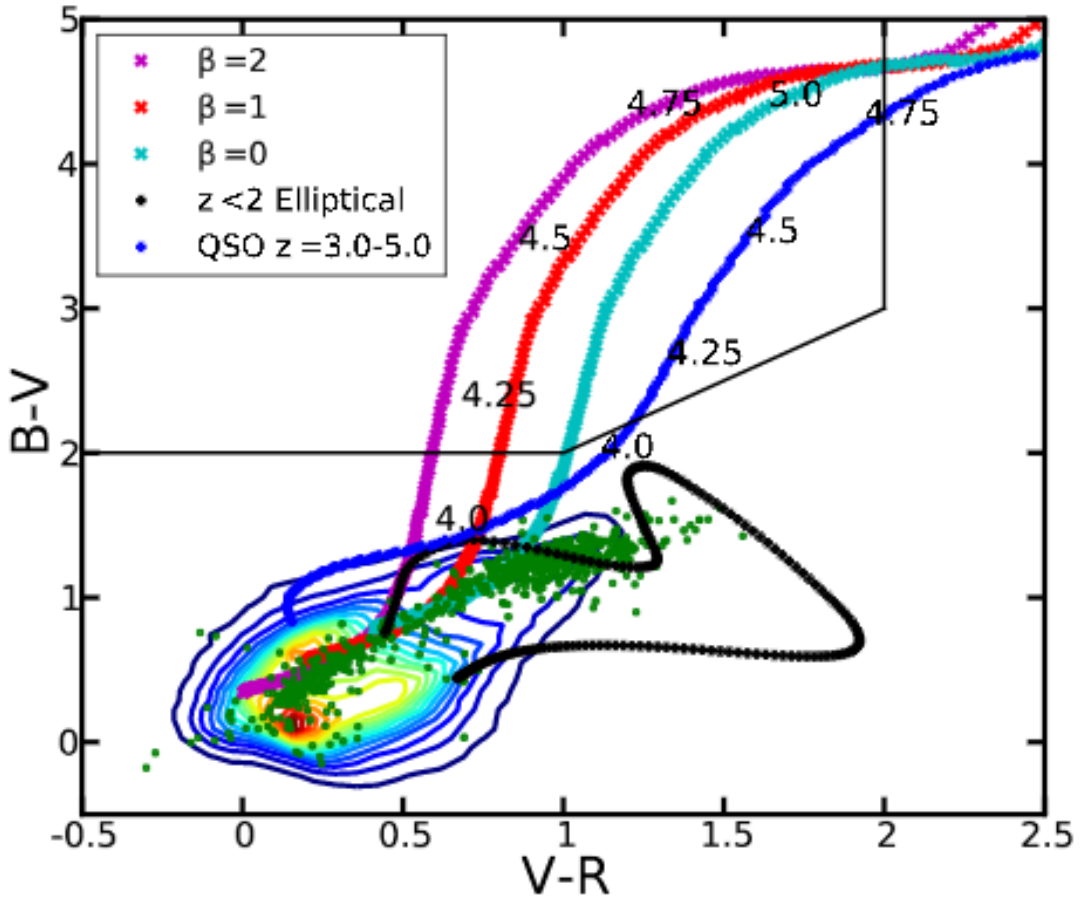


Figure 1.8: Figure from Morrison et al. [2012]. LBG selection for B-dropouts in the Deep Lens Survey (DLS) is shown here by the black bounding box. The three tracks denoted by  $\beta$  show model LBGs with different UV continuum slopes at redshifts indicated along the track. Density contours are DLS galaxies with a B-band S/N > 2 detection. Green points are stars detected in DLS. The black track is the evolution of an elliptical galaxy template from redshift  $0 < z < 2$ . The blue track is a sample quasar spectrum redshifted from  $z = 3-5$ .

for additional information about the growth of cosmic structure over time.

In Chapters 4 and 5, we will discuss a new Bayesian method for selecting LBGs using templates with known fluxes and reliable photometric redshifts instead of the box-

selection methods described above. We also detail how to use these LBGs as sources in a measurement of cosmic magnification using the Dark Energy Survey.

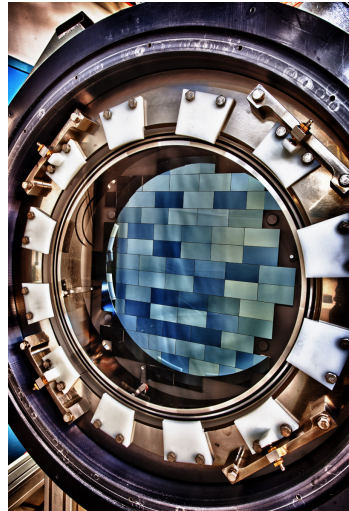
## 1.3 The Dark Energy Survey

The Dark Energy Survey (DES)<sup>1</sup> is a five-year 5,000 deg<sup>2</sup> photometric survey of the Southern sky over Chile. DES uses a 570 Megapixel camera, the Dark Energy Camera (DECam, Figure 1.9a), mounted on the Blanco 1.4-meter telescope at the Cerro Tololo Inter-American Observatory (CTIO)<sup>2</sup>. The DES collaboration consists of several hundred international scientists including graduate students, faculty, postdocs, and staff researchers and scientists. To date, DES has completed five years of observing (ending in February 2018). A partial 6th season has been scheduled. The current data products available to the collaboration consist of catalogs from the Science Verification (SV, ~150 deg<sup>2</sup>) run in 2012, and the Year 1 (Y1) and Year 3 (Y3) compilations of observations, with the SV and Y1 data available to the public. A map of the survey regions studied in these datasets is shown in Figure 1.10. The main goal of DES is to study the properties of dark energy using the three main experiments mentioned earlier: a supernovae search, galaxy cluster number counts, and weak gravitational lensing. The goal of my Ph.D. research has been to both improve and contribute to DES science, specifically in the field of weak gravitational lensing. Another effort I have put forth is that of making DES science accessible to the wider public audience. Chapter 6 of this dissertation describes the academic pursuit of surveying DES collaborators about their personal and professional relationships with science education and outreach.

---

<sup>1</sup>[darkenergysurvey.org](http://darkenergysurvey.org)

<sup>2</sup>[www.ctio.noao.edu](http://www.ctio.noao.edu)



(a) The DECam focal plane.



(b) DECam is mounted on the Blanco Telescope, shown here.

Figure 1.9: (Images: Reidar Hahn, Fermilab)

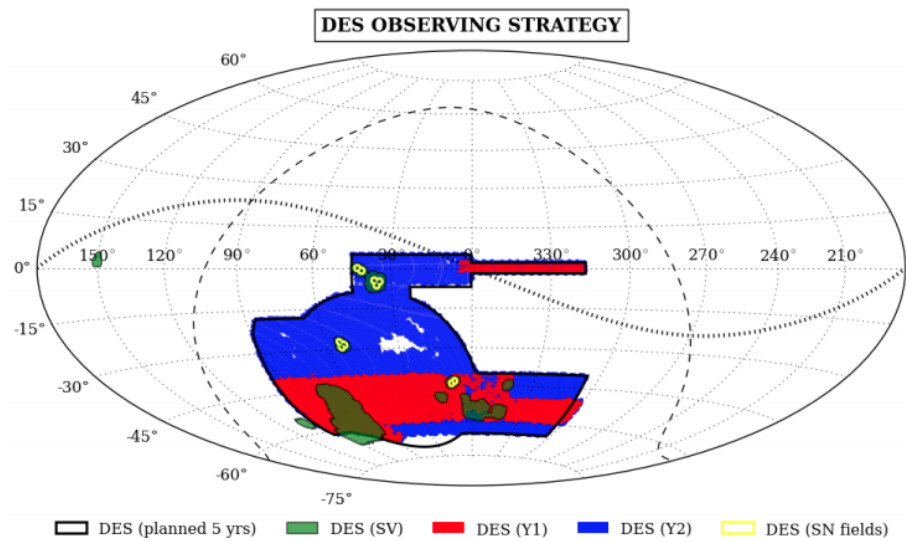


Figure 1.10: DES observing strategy [Abbott et al., 2016].

# **Chapter 2**

## **Analyzing the Impact of Wind on DES Image Quality**

### **2.1 Introduction**

The amplitude of the weak gravitational lensing effect is very small, and thus requires precise measurement. Unfortunately, telescopes on Earth deal with several handicaps in this pursuit. The distant light rays we eventually capture must first pass through our atmosphere, a thick layer of gases, just before hitting the detector. The density and movement of the atmospheric layers act to blur the recorded images. This blurring can change the appearance of objects, galaxy shapes among the most important. To try and correct for this effect - called "seeing" - and other imperfections of the telescope structure, one can look at the shapes of any stars they have observed. Since stars are effectively point sources, any distortion in their size and shape can be attributed to the state of these variations at the time of exposure. This stellar size that we measure for each image is called the point spread function (PSF). One can deconvolve this PSF from the image to try and recover the true features of a given object, but residual information from an improper fit can leak into shape measurements. Any ellipticity contribution from the PSF is typically a few percent larger than the ellipticity induced by gravitational lensing, which is of order 1%. This is

thus an important systematic to understand for cosmological analyses.

A small PSF is a good PSF, as is a well-understood one. If we as observers can minimize the PSF size before it is even measured and later used for corrections, then we can save potential small-scale information and avoid wasting exposure time on unusable data. Possibly the most basic tactic ground-based astronomers use to maximize exposure potential is to only observe on nights with good weather. There is typically standard protocol for closing a telescope's dome in the case of rain, snow, or extreme wind. When the dome is open however, there are additional rules for managing the latter. The Blanco Telescope, on which the Dark Energy Camera (DECam [Flaugher et al., 2015]) is mounted, has wind blinds that can be raised and lowered by the operations team. The current rules for DES observing teams are as follows: "When wind speeds are  $> 5 - 8$  mph (8-13 km/h)...raise the wind blind...When wind speeds are  $> 15$  mph (24 km/h)...close the louver windows around the dome floor. At low wind speeds, it's best to keep everything open to maximize ventilation of the dome."<sup>1</sup> Dome ventilation is important for keeping the air temperature around the telescope homogenous. Having the blinds and louvers in place may also cause vignetting of the images due to the physical obstruction which is obviously not ideal. The wind speeds quoted above are continuously checked by the observing team through the local weather station website. This of course gives no indication as to the state of air flow *inside* the dome. We would therefore like to decide whether interior wind conditions could ever possibly have a  $> 1\%$  effect on the PSF ellipticity, and if so, how we can avoid it.

Many previous studies have been conducted with this concern in mind. Models of internal wind flow (due to external wind interacting with the dome slit) have demonstrated that wind can excite resonant modes in the different structural elements that make up the telescope depending on the dome design and the pointing angle [Pottebaum and MacMynowski, 2006]. The image degradation that results from this jitter has the potential to contribute significantly to the telescope error budget for large ground-based telescopes

---

<sup>1</sup>DES observation wiki.

[Angeli et al., 2004]. While the Blanco Telescope (which has a 4-meter diameter primary mirror) engages in the aforementioned wind protocol, no official test has been done to determine the actual effect of wind inside the dome. Concerns about data quality were raised at a DES collaboration meeting when some interesting features were noticed in data from an accelerometer that had been installed on Blanco, such as large spikes and periodic motion. While Chile does experience some regular seismic activity, we could not find any available data of this kind to link it to the telescope motion. Since an anemometer had just been installed on the telescope, we decided to explore the effect of interior wind on its movement and whether the impact was causing the large anomalies recorded by the accelerometer. Of wider concern was to determine if any of this motion was causing significant harm to the end science goals of the survey through negative effects on image quality.

## 2.2 Data

### 2.2.1 Anemometer

There is a WindMaster [Gil, 2010]<sup>2</sup> anemometer located on the top ring of the Blanco Telescope, as shown in Figure 2.1. It measures the speed (in m/s) and direction of the wind inside the dome. We used all of the available anemometer data at the time - this consisted of time periods between April 21, 2014 to May 15, 2014 and September 17, 2014 to October 21, 2014, when we completed this work, for a total of 58 days. The anemometer data had not previously been analyzed, only fed automatically into the DES telemetry database. We were able to query this database for data within any desired time frame. We visually inspected the interior wind data for each night available in the database. Some selected days of wind data are shown in Figure 2.2.

---

<sup>2</sup><http://gillinstruments.com/data/manuals/WindMaster-and-Windmaster-Pro-Manual.pdf>

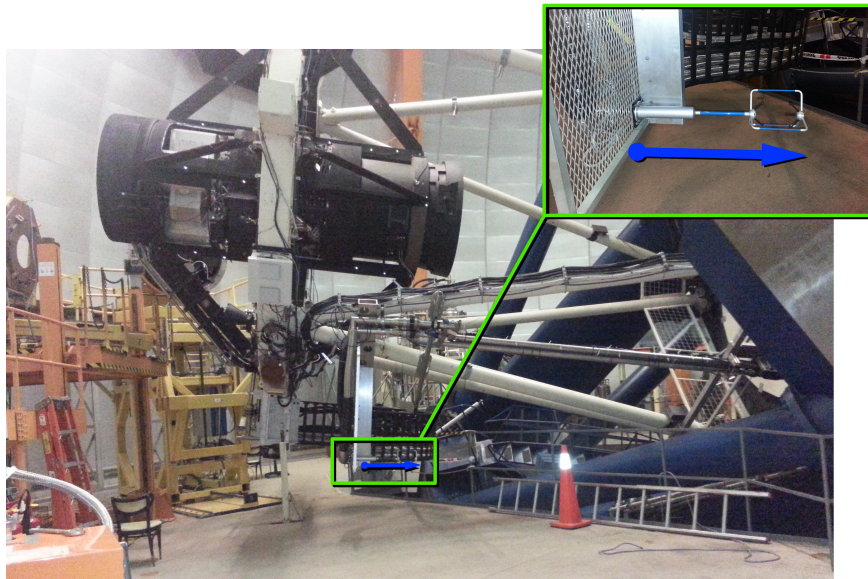
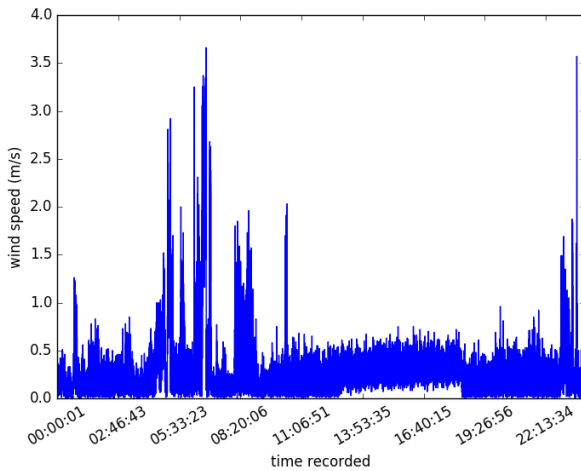


Figure 2.1: The anemometer (inset) and its position and orientation (blue arrow) on the telescope.

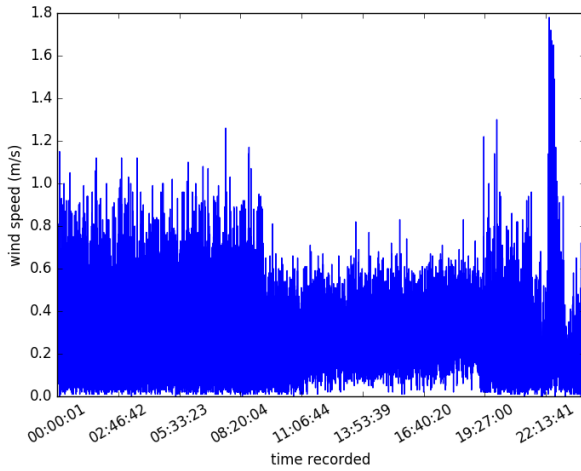
### 2.2.2 Accelerometer

There is an accelerometer fitted on the telescope as shown in Figure 2.3. The accelerometer data was not as easily accessible as the anemometer data. Through correspondence with a scientist working closely with the Blanco instrumentation, I was able to request a week's worth of accelerometer data at a time. The data is originally recorded at a sampling frequency of 500 Hz and is sensitive to motion with frequencies  $\geq 1\text{Hz}$ . I began compressing this information by averaging from the original 500 Hz sampling down to 50 Hz in each of the 3 directions (X, Y, and Z) to save disk space and computation time. The accelerometer data is collected through LabView, making it necessary to convert the data to binary FITS tables and put the raw output voltage into acceleration units. Acceleration data was ultimately compiled for 3 separate weeks (one each in May, September, and October 2014).

Since we were only interested in motion that could have a detrimental effect on the quality of the exposure being taken at the time, we then segmented the data using the



(a) Wind speed measurements for the night of May 5, 2014. This output is typical for the nights we inspected - there are usually one or two spikes visible like the one here.



(b) Wind speed measurements for the night of May 3, 2014. This was a fairly calm night - note the difference in scale from (a).

Figure 2.2: Two different nights in anemometer data.

exposure time stamps from the DES exposure database. Typical wide field exposures used for weak lensing analyses are 30 seconds long, which means that over the duration of the exposure, the accelerometer will track the change in gravity due to the telescope tracking



(a) The accelerometer.

(b) Mounted on the Blanco top ring.

Figure 2.3: Photos by Kevin Reil.

the target location on the sky. I thus subtracted a linear fit to the data across the time of the exposure. We also applied a butterworth highpass filter at 1 Hz to remove low-frequency noise. This acceleration signal was then integrated twice to get the displacement incurred on the telescope. A schematic of this reduction process is shown in Figure 2.4.

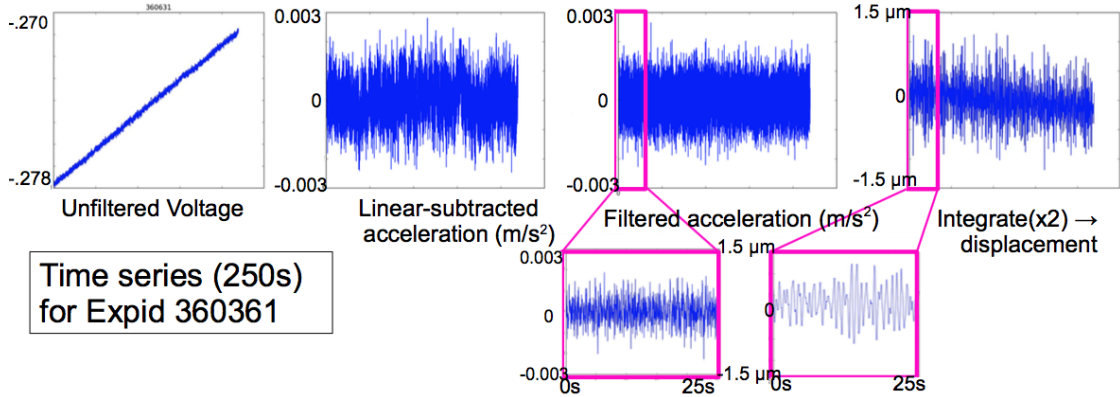


Figure 2.4: The process for converting the unfiltered voltage readings from the accelerometer into the actual displacement incurred on the telescope.

### 2.2.3 Telescope Control System and Guider

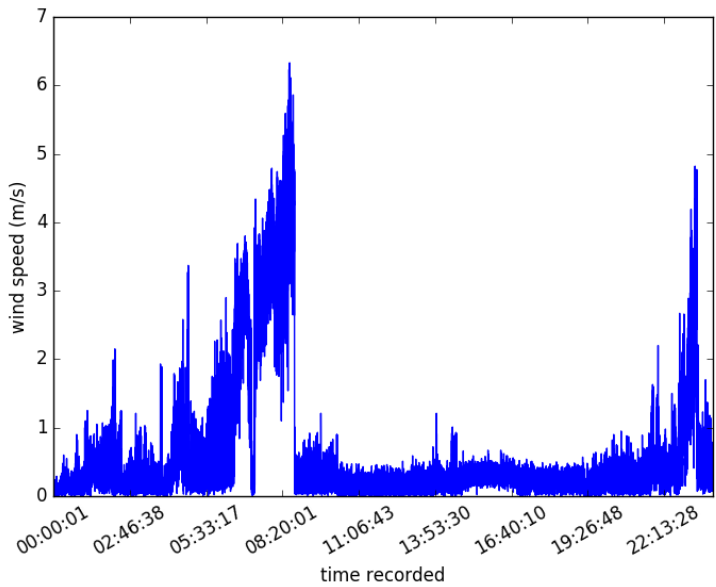
The telescope control system (TCS) is what directs the telescope to point to the desired location on the sky. It keeps track of the telescope position and velocity, recording data

at a rate of 100 Hz, and reports the means and errors of hour angle (HA) and declination (DEC) to the DES telemetry database. To ensure the precision of the telescope tracking controlled by this system, there are four 2048x2048 pixel "guider" CCDs in addition to the DECam science array. The guider CCDs are each initially focused on an isolated, high signal-to-noise reference star in the field of view. They track these stars throughout the exposure and calculate the offset between the current and original positions of the reference star. This information is fed back to the TCS so that minute changes in pointing can be made to improve accuracy. The guider also outputs this information to the telemetry database. This motion tracking is on a longer timescale than what is sampled by the accelerometer, so we can look at TCS and guider data for insight into movement at frequencies less than 1 Hz.

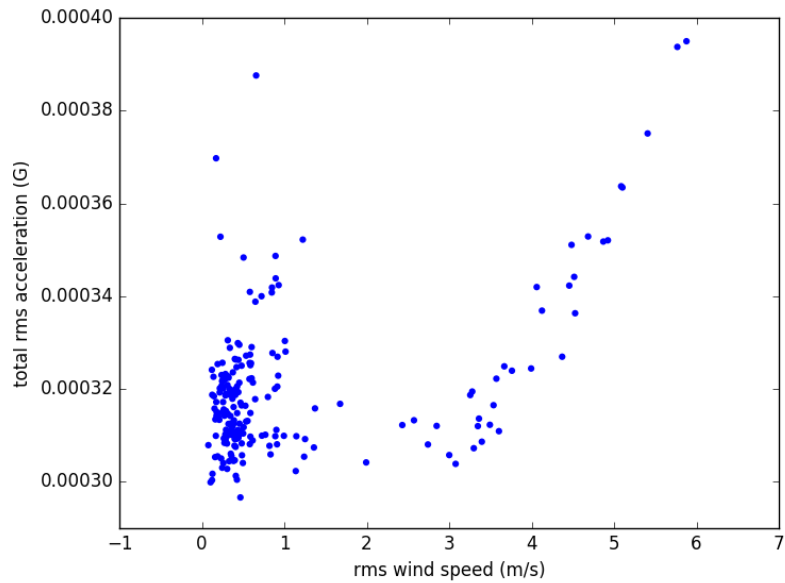
## 2.3 Results

Using information from the DES exposure database, we were able to retrieve wind statistics for each exposure using the reported timestamps. After condensing each night into a set of rms wind speeds for each exposure, we found the typical rms values to be in the range of 0-2 m/s, with a handful of nights over 3 m/s. Since we were particularly interested in excessive wind, it was important to closely examine nights such as May 9th, 2014, as shown in Figure 2.5, where the wind speed grew in magnitude over the course of the night. The right panel in Figure 2.5 shows the upward trend of acceleration and displacement with wind speed starting fairly sharply around 3 m/s.

However, looking at the totality of exposures included in this analysis, shown in Figure 2.6, typical displacements incurred rarely exceed  $1.2 \mu\text{m}$ , and have a only a slight upward trend at wind speeds above 3-4 m/s. Importantly, these high values were rarely recorded. The size of a single pixel in the DECam focal plane is  $15 \mu\text{m}$ , with a pixel scale of 0.263 arcsec/pixel [Flaugher et al., 2015]. Since the PSF size is generally around 1 arcsec, the most extreme motion seen in this analysis would generally have less than a



(a) Wind speed gradually increased to over 4 m/s during observing time.



(b) Rms acceleration vs. wind speed for each exposure.

Figure 2.5: The night of May 9th, 2014.

0.25% effect on PSF ellipticity, safely below our 1% limit.

The guider data, however, shows potentially significant movement at frequencies  $\leq 1$

Hz. The wind seems to be causing this motion almost entirely in right ascension – the  $y$  direction for the guider and the  $x$  direction for the TCS. The variance in these values are plotted in Figure 2.7.

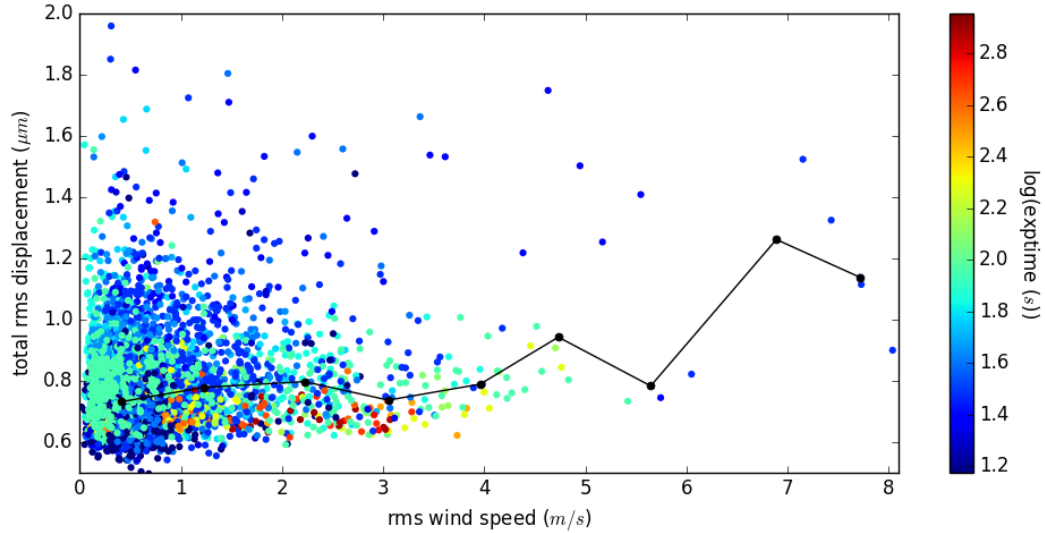


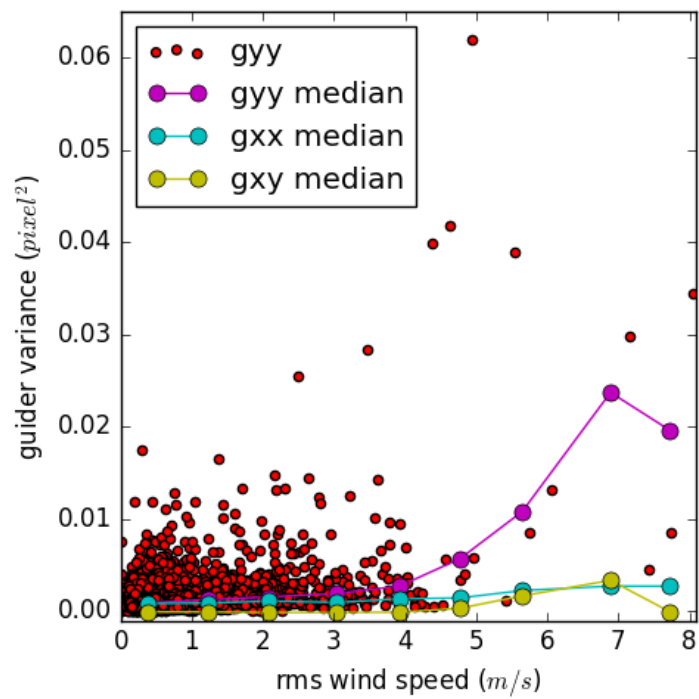
Figure 2.6: Total rms displacements vs. rms wind speeds for each exposure included in this study. The median values are shown in black.

## 2.4 Conclusions

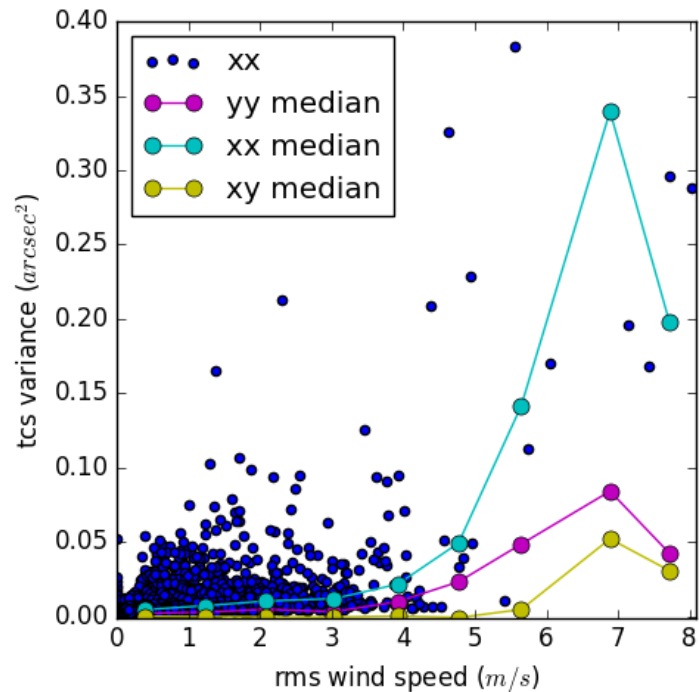
It is clear that there is large scatter in telescope movement at all wind speeds, with higher displacement values occurring at low wind speeds that are comparable to those found at high wind speeds. In conclusion, we see motion that trends positively with wind, but the highest rms wind speeds produce  $< 1\%$  ellipticity at frequencies greater than 1Hz. Thus, it would be rare for the wind to have a significant impact on image quality due to motion at high frequencies.

At lower frequencies, the guider and TCS data show that wind may have an effect on the precision of the telescope tracking. The trends discovered here were presented to the DES Operations group at a collaboration meeting in October, 2014. The group agreed

to enable monitoring of the anemometer data during observing using the DES telemetry database in the future. However, the anemometer has been only working intermittently before and since the completion of this project.



(a) Guider variance as a function of rms wind speed per exposure.



(b) TCS variance as a function of rms wind speed per exposure.

Figure 2.7

# Chapter 3

## Testing the Bayesian Fourier Domain Shear Measurement Method

This chapter is adapted from Bernstein et al. [2016].

### 3.1 Introduction

As summarized in Chapter 1, weak lensing (WL) by foreground bodies acts to transform the images of background “source” galaxies on the sky. This transformation is described by the measurable quantities  $\mu$  (magnification) and  $g$  (shear). These quantities provide a measurement of the second (and potentially higher) derivatives of the scalar gravitational potential along the line of sight to the source. WL thus provides a critical observational window into the behavior and history of the components of the Universe that consist of dark matter - matter that does not absorb or emit photons. WL can also test the laws of gravitation relating the potential to the matter.

The state-of-the-art in visible/near-IR imaging, which includes the *Dark Energy Survey (DES)* [Jarvis et al., 2016], the *Kilo-Degree Survey (KiDS)* [Kuijken et al., 2015], and the *Hypersuprime-cam Survey (HSC)* [Takada, 2010], survey thousands of square degrees of sky with measurement of WL signals from images of  $O(10^8)$  galaxies. And upcoming

surveys plan to measure  $> 10$  times this amount in the 2020's: *the Large Synoptic Survey Telescope (LSST)*<sup>1</sup>, the *Euclid* spacecraft [Laureijs et al., 2011]<sup>2</sup>, and the *Wide-Field Infrared Survey Telescope (WFIRST)*.<sup>3</sup> To have systematic errors be sub-dominant to the expected statistical uncertainty due to this large sample size, these surveys require errors in shear measurement on the order of  $|m| \lesssim 10^{-3}$  and  $c_{\text{RMS}} \lesssim 10^{-3.5}$  and below [Huterer et al., 2006, Amara and Réfrégier, 2008], where  $g_{\text{meas}} = (1 + m)g_{\text{true}} + c$ . The Bayesian Fourier Domain method (BFD) is one of the first methods to demonstrate this capability on realistic simulations.

Historically, weak lensing shape measurement has been done by estimating individual object ellipticities through the modelling of targeted galaxies as some combination of chosen light profiles, i.e. bulge+disk, and sersic or gaussian mixtures. In fact, the two shear measurement methods used in the DES Science Verification (SV) analysis [Jarvis et al., 2016], IM3SHAPE [Zuntz et al., 2013] and NGMIX [Sheldon, 2014], are of this type. There are several common sources of bias in these techniques: noise bias (IM3SHAPE calculates a correction for this bias using simulations), model bias, and selection bias. BFD is unique in that it specifically eliminates or accounts for each of these biases. What also sets BFD apart from other shear measurement techniques is that it does not make estimates of individual galaxy shape properties, but instead gives a posterior distribution of the average shear of a targeted set of galaxies.

We will estimate lensing parameters from images of galaxies, but the signal we seek is weak, with magnification and shear having RMS amplitudes of  $\approx 0.02$  on cosmological lines of sight. This low amplitude results in several hurdles to overcome. We first encounter complications arising from the point spread function (PSF) of the imaging, whose asymmetries and variation are larger than lensing signal we are trying to extract. Since the source galaxies are typically of comparable intrinsic size to the PSF, ideally we would deconvolve the PSF from the image to retrieve the true size and shape of the

---

<sup>1</sup><http://www.lsst.org>

<sup>2</sup><http://www.euclid-ec.org>

<sup>3</sup><http://wfirst.gsfc.nasa.gov>

galaxy.

### 3.1.1 How BFD Works

Our goal is to infer the lensing distortion  $g$  from the observational data vector  $D$ . Our current implementation assumes pure-shear distortions, so  $g = (g_1, g_2)$ , but the formalism is unchanged if we include magnification  $\mu$  in  $g$  as well. By Bayes' theorem

$$P(g|D) = \frac{P(D|g)P(g)}{P(D)}. \quad (3.1)$$

We will not be concerned with the normalization by the evidence  $P(D)$ . We will assume that all galaxies are viewed through a common lensing  $g$ , and that the prior  $P(g)$  is much less informative than the data and can be taken as uniform. Thus we focus on determining  $P(D|g)$ . We leave to future work the extension of the method to other circumstances, such as when  $g$  is known to follow some parametric form of position (discussed in Bernstein and Armstrong [2014], hereafter BA14), or when  $g$  is drawn from a Gaussian random field.

### 3.1.2 Simplest case

Ultimately we will need to determine  $P(D|g)$  in the case where the data contain images of an arbitrary number of galaxies at unknown locations. We will assume that the pre-seeing, pre-lensing images are drawn from a known library of “template” galaxies, indexed by  $G$ , which in practice we will obtain by observing a fraction of our survey to significantly higher  $S/N$ . We begin, however, with a simple case, in which we know we are observing a single galaxy known to have underlying template index  $G$ . The position on the sky of some reference point in the galaxy (such as its centroid) we denote as  $x_G$ . Knowing  $G$  we simulate the action of the lensing distortions and the observing process (namely the PSF and pixelization) to predict the data vector  $D^G(g, x_G)$  that we would obtain from a noiseless observation. The observed data vector is

$$D = D^n + D^G(g, x_G), \quad (3.2)$$

and we assume that we know the likelihood function  $\mathcal{L}(D^n)$  of the added noise. In the case that  $x_G$  is known, we have

$$P(D|g) = \mathcal{L}(D^n) = \mathcal{L} \left[ D - D^G(g, x_G) \right]. \quad (3.3)$$

A central strategy of BFD is to compress the pixel data to a short vector  $M$  that carries most of the information about lensing distortion. The critical requirement on the compression is that we are able to propagate the distribution of  $D^n$  into a probability  $P(M|M^G)$  of observing compressed data  $M$  given that the noiseless underlying galaxy image compresses to  $M^G$ . This is most straightforwardly accomplished by having the compression be a linear operation on  $D$  such that Equation (3.2) becomes

$$M = M^n + M^G(g, x_G), \quad (3.4)$$

and we will have, for fixed  $x_G$ ,

$$P(M|g) = \mathcal{L}(M^n) = \mathcal{L} \left[ M - M^G(g, x_G) \right]. \quad (3.5)$$

We choose for  $M$  a set of moments of the Fourier transform  $\tilde{I}^o(k)$  of the observed surface brightness  $I^o(x)$ , defined as

$$\tilde{I}^o(k; x_0) \equiv \int d^2x I^o(x) e^{-ik \cdot (x - x_0)} \quad (3.6)$$

Note that this compression requires a choice  $x_0$  of coordinate origin. In this section we will assume that we have *a priori* knowledge of  $x_G$  and can set  $x_0 = x_G$ . In the next section we will develop a treatment for the case of unknown  $x_G$ . The data  $D$  are a regular sampling of  $I^o$ , so in practice the Fourier transforms are discrete. We choose the compressed data vector

$$M(x_0) \equiv \begin{pmatrix} M_f \\ M_r \\ M_+ \\ M_\times \end{pmatrix} = \int d^2k \frac{\tilde{I}^o(k; x_0)}{\tilde{T}(k)} W(|k^2|) F; \quad F \equiv \begin{pmatrix} 1 \\ k_x^2 + k_y^2 \\ k_x^2 - k_y^2 \\ 2k_x k_y \end{pmatrix}. \quad (3.7)$$

where  $\tilde{T}(k)$  is the Fourier transform of the PSF that has convolved the observed image.  $W(|k^2|)$  is a real-valued window function applied to the integral to bound the noise, in

particular confining the integral to the finite region of  $k$  in which  $\tilde{T}(k)$  is non-zero. We calculate the moments in Fourier domain in order to simplify the removal of the effects of the PSF, but these moments are equivalent to taking radially weighted zeroth and second moments of the real-space, pre-seeing image of the galaxy.

The moments are *not* normalized, so that  $M$  remains a linear function of  $D$ . The noise moment vector, being a sum over the statistically independent noise of many pixels, will have a likelihood  $\mathcal{L}(M^n)$  rapidly tend toward a multivariate Gaussian with covariance matrix  $\mathbf{C}_M$ . We assume that *the pixel noise  $D^n$  is stationary*, in which case there is no covariance between the noise at distinct  $k$  values, and the covariance matrix elements are related to the power spectrum  $P_n(k)$  of the noise by

$$(\mathbf{C}_M)_{ij} = \int d^2k P_n(k) \left| \frac{W(|k^2|)}{\tilde{T}(k)} \right|^2 F_i(k) F_j^*(k). \quad (3.8)$$

Note that while background shot noise and detector read noise are stationary, any significant shot noise from the galaxy's photons will violate stationarity. With sensible choice of  $W$ , the moments  $M$  carry most of the information available about shear of the source [Bernstein and Jarvis, 2002]. There are many practical benefits to discarding the rest of the information in  $D$ , as will become apparent, but we highlight first that  $M^G$  is independent of the observational conditions, *i.e.* has been corrected for the PSF, so we do not need to recalculate  $M^G$  as the PSF varies, as long as we hold  $W$  fixed.

We note at this point that there is much freedom in the choice of  $W$ . As long as  $W$  leads to finite noise  $\mathbf{C}_M$  via Equation (3.8), BFD remains valid and unbiased; but the accuracy of the inference on  $g$  will depend upon the choice of  $W$ . One may choose to adjust this weight to optimize shear inference for a given set of observing conditions, but it is critical that the choice does *not* depend upon the properties of target galaxies. In this sense the BFD method is sub-optimal, in that it may not extract the most precise measure of  $g$  from both large and small galaxies simultaneously. We describe one choice for  $W$  in Section 3.2.3.

The next assumption in BFD is that *the lensing is weak, so that a second-order Taylor expansion about  $g = 0$  fully describes  $P(M|g)$  for observed values of  $g$* . In this case we

have

$$P(M|g) = P + Q \cdot g + \frac{1}{2} g \cdot \mathbf{R} \cdot g, \quad (3.9)$$

$$P \equiv P(M|g=0) = \mathcal{L}(M - M^G) = |2\pi \mathbf{C}_M|^{-1/2} \exp \left[ -(M - M^G)^T \mathbf{C}_M^{-1} (M - M^G) \right], \quad (3.10)$$

$$Q \equiv \nabla_g P(M|g)|_{g=0} = -\nabla_g M^G \cdot \nabla_M \mathcal{L}(M - M^G) \quad (3.11)$$

$$\mathbf{R} \equiv \nabla_g \nabla_g P(M|g)|_{g=0}. \quad (3.12)$$

At the end of Equation (3.11) we have assumed that *the noise likelihood is invariant under shear of the underlying galaxy G* so that we can propagate all shear derivatives into derivatives of the properties of the template galaxy. This is satisfied for background-limited images. The quantities  $Q$  and  $\mathbf{R}$  give the differential probability of observing the image under lensing distortions. If  $D$  is comprised of many independent observations  $D_i$  of the same underlying galaxy  $G$  with the same applied lensing, we can produce the quantities  $P_i, Q_i, \mathbf{R}_i$  as above for each observation, then the total posterior probability for  $g$  is given by

$$-\ln P(g|D) = (\text{const}) - \ln P(g) - \sum_i \ln P(D_i|g) \quad (3.13)$$

$$= (\text{const}) - \ln P(g) - g \cdot Q_{\text{tot}} + \frac{1}{2} g \cdot \mathbf{R}_{\text{tot}} \cdot g, \quad (3.14)$$

$$Q_{\text{tot}} \equiv \sum_i \frac{Q_i}{P_i} \quad (3.15)$$

$$\mathbf{R}_{\text{tot}} \equiv \sum_i \left( \frac{Q_i Q_i^T}{P_i^2} - \frac{\mathbf{R}_i}{P_i} \right) \quad (3.16)$$

The posterior distribution is, ignoring the prior, Gaussian in  $g$ , with inverse covariance matrix

$$\mathbf{C}_g = \mathbf{R}_{\text{tot}}^{-1} \quad (3.17)$$

and mean value

$$\bar{g} = \mathbf{R}_{\text{tot}}^{-1} Q_{\text{tot}}. \quad (3.18)$$

### 3.1.3 Detection and selection

Consider now the case where there is a galaxy present but we do not know its position  $x_G$  in advance, so we need a prescription for choosing those locations  $x_0$  about which we will compute moments. We need a *detection* process to decide if the galaxy has been observed within some small region  $\Delta^2 x$  about some position  $x_0$ . Once a detection is made, we will also require some *selection* criteria to decide which detections will be used to constrain the lensing. In this section, we will continue to assume that the unlensed appearance  $G$  of the galaxy is known, but its location is not. At each potential source location, we end up with either a successful detection and selection, plus measured moments  $M$ ; or a non-selection. We therefore need to know  $P(M, s, d|G) = P(M, s|G)$  for the former case, and  $1 - P(s|G)$  for the latter case, where  $s$  ( $d$ ) indicates successful selection (detection).

These probabilities are readily calculable if we make the detection and selection using the compressed quantities themselves. We add to our compressed data set the two weighted first moments of the source in Fourier space:

$$X(x_0) \equiv \int d^2 k \frac{\tilde{I}^o(k; x_0)}{\tilde{T}(k)} W(|k^2|) \begin{pmatrix} ik_x \\ ik_y \end{pmatrix}. \quad (3.19)$$

We choose as a criterion for detection of a source at  $x_0$  that  $X(x_0) = 0$ . Our choice of moments for  $M$  and  $X$  have these useful properties:

$$\frac{dM_f}{dx_0} = X, \quad (3.20)$$

$$\text{Cov}(M, X) = 0 \quad (\text{for stationary noise}), \quad (3.21)$$

$$J \equiv \left| \frac{dX}{dx_0} \right| = (M_r^2 - M_+^2 - M_\times^2) / 4 = M^T \mathbf{B} M, \quad (3.22)$$

$$\mathbf{B} \equiv \text{diag}(0, 1/4, -1/4, -1/4), \quad (3.23)$$

$$\langle J^n \rangle = \text{Tr}(\mathbf{B} C_M) = 0, \quad (3.24)$$

The first line means that we detect a source at all stationary points of the function  $f(x_0) = M_f$ , the zeroth moment of the image as convolved with a filter defined by  $W(|k^2|)/\tilde{T}(k)$ . This filter will be broader than the PSF in any sensible application of

BFD. The second property yields  $\mathcal{L}(M^n, X^n) = \mathcal{L}(M^n)\mathcal{L}(X^n)$  for our multivariate Gaussian noise distribution. The third property shows that the Jacobian determinant  $J$  of the positional moments  $X$  is purely a function of  $M$ , and hence statistically independent of  $X$ .

The noiseless moments expected from galaxy  $G$  are now functions  $D^G(g, u = x_G - x_0)$  and  $X^G(g, u)$  since it is only the displacement  $u$  between the galaxy location and the Fourier phase center that matters. The detection condition is  $X = X^G + X^n = 0$  so the probability of this occurring in a small region  $\Delta^2 x$  about  $x_0$  is

$$P(M, d|G, g, x_G, x_0) = \mathcal{L}\left[M - M^G(g, x_G - x_0)\right] \mathcal{L}\left[-X^G(g, x_G - x_0)\right] \left|\frac{dX}{dx_0}\right| P(x_0) \Delta^2 x \quad (3.25)$$

$$= \mathcal{L}\left[M - M^G(g, x_G - x_0)\right] \mathcal{L}\left[X^G(g, x_G - x_0)\right] |J| \Delta^2 x. \quad (3.26)$$

In the last line, we take advantage of (3.22), assume a uniform prior  $P(x_0)$  on the position of the detection, and note that the zero-mean, multivariate Gaussian will have  $\mathcal{L}(-X^G) = \mathcal{L}(X^G)$ .

To eliminate noise detections, we will want to discard low-flux detections. We implement the selection criterion as membership in a subregion  $S$  of moment space:

$$S : f_{\min} < f < f_{\max} \quad (3.27)$$

$$\Rightarrow P(M, s|G, g, x_G, x_0) = \begin{cases} \mathcal{L}(M - M^G) \mathcal{L}(X^G) |J| \Delta^2 x & M \in S \\ 0 & M \notin S \end{cases} \quad (3.28)$$

$$\Rightarrow P(s|G, g, u = x_G - x_0) = \mathcal{L}(X^G) \Delta^2 x \int_{M \in S} dM \mathcal{L}(M - M^G) |J(M)|. \quad (3.29)$$

For brevity we suppress the dependence of the template galaxy's moments  $M^G, X^G$  on the applied lensing  $g$  and on the displacement  $x_G - x_0$  between the galaxy position and the detection location.

To render the integration in (3.29) tractable, we make the simplifying assumption that *the Jacobian determinant  $J$  of the first moments is positive at any location where there is non-negligible probability of selection*:

$$J = M^T \mathbf{B} M = J^G + 2 \left( M^G \right)^T \mathbf{B} M^n + J^n > 0. \quad (3.30)$$

Since  $J$  is the determinant of the 2nd derivative matrix of  $f$ , a restatement is that we are assuming the  $f(x_0)$  surface is (nearly) always convex if  $f_{\min} < f < f_{\max}$ . To maintain this approximation we will need to avoid noise detections by raising  $f_{\min} \gtrsim 5\sigma_f$ , where we define

$$\sigma_f^2 = (\mathbf{C}_M)_{ff}. \quad (3.31)$$

With this approximation, we can integrate a multivariate Gaussian  $\mathcal{L}$  in Equation (3.29) analytically, obtaining

$$P(s|G, g, u) = \mathcal{L}(X^G) \Delta^2 x \left[ J^G Y + 2 \left( \mathbf{C}_M \mathbf{B} M^G \right)_f \frac{\partial Y}{\partial f_G} + (\mathbf{C}_M \mathbf{B} \mathbf{C}_M)_{ff} \frac{\partial^2 Y}{\partial f_G^2} \right], \quad (3.32)$$

$$Y \equiv (2\pi)^{-1/2} \int_{(f_{\min} - f_G)/\sigma_f}^{(f_{\max} - f_G)/\sigma_f} dv e^{-v^2/2}. \quad (3.33)$$

Now consider the joint distribution of the detection/selection outcomes at a grid  $x_1, x_2, \dots, x_j \dots$  of all search positions with non-negligible selection probability  $P(s|G, x_G, x_0 = x_j)$ . We assume now that *galaxies are uncrowded, in that no other galaxies contribute significantly to  $M$  or  $X$  at any location  $x_j$  where galaxy  $G$  might be selected*. At each search position, we either have a selection and a resultant  $M$ , or we have a non-selection. If the search region is contiguous, there can be *at most one* of the  $x_j$  with successful selection. This follows from our assumption that  $J > 0$ , which implies that that map  $x_0 \rightarrow X$  is one-to-one over a contiguous region, so that  $X = 0$  can only occur at a single  $x_0$ .

With this single-selection rule, we have two possible outcomes:

1. A detection at a single location  $x_j$  yielding moments  $M$ , with probability  $P(M, s_j|G)$  from Equation (3.28), or
2. No detection at all, with probability  $1 - \sum_j P(s_j|G)$ , using the selection probability in Equation (3.32).

Integrating over all possible detection positions, we obtain a total probability of outcome

(1):

$$P(M, s|G, g, x_G) = J(M) \int d^2 u \mathcal{L} \left[ X^G(g, u) \right] \mathcal{L} \left[ M - M^G(g, u) \right]. \quad (3.34)$$

$$\approx J(M) \sum_u \Delta^2 u \mathcal{L} \left[ X^G(g, u) \right] \mathcal{L} \left[ M - M^G(g, u) \right]. \quad (3.35)$$

In the second line, we change the integration to a sum over a 2d grid of points  $u$  with cell area  $\Delta^2 u$ , since this is how we implement the integration over source position. We can truncate the grid where  $P(s_j|G)$  becomes negligible. As expected, the resulting probabilities are independent of both the true position  $x_G$  of the galaxy and the position  $x_i$  of the detection once the observed moments  $M$  are specified.

The total probability of detection is obtained by similarly integrating Equation (3.32) over all  $u$ :

$$P(s|G, g) = \sum_u \Delta^2 u \mathcal{L} \left( X^G \right) \left\{ J \left( M^G \right) Y + 2 \left( \mathbf{C}_M \mathbf{B} M^G \right)_f \frac{\partial Y}{\partial f_G} + (\mathbf{C}_M \mathbf{B} \mathbf{C}_M)_{ff} \frac{\partial^2 Y}{\partial f_G^2} \right\}, \quad (3.36)$$

remembering that  $M^G, X^G, f_G$ , and the arguments to  $Y$  depend upon  $g$  and  $u$ . For a galaxy with flux  $f_G$  that is many  $\sigma_f$  away from the selection boundaries, we have  $Y \rightarrow 1$ . In this case it is easy to see that  $P(s|G, g) \rightarrow 1$ , by recasting (3.36) as an integral over  $X^G$ —as long as  $J > 0$ . If the positive- $J$  assumption does not hold, Equation (3.36) is incorrect, and we can have a mean number of detections per source that is  $> 1$ . In Section 3.4.3 we discuss our approach to mitigating failure of the positive- $J$  assumption.

### 3.1.4 Galaxy populations: postage stamp case

Now we generalize from having a single galaxy type  $G$  to having  $G$  be an index into the entire catalog of possible galaxy images. We assume we know the prior probability  $p_G$  that a galaxy is of type  $G$ . If for example the galaxy library is approximated by the set of galaxies found in a high- $S/N$  imaging survey of the sky, each detected galaxy would be assigned equal  $p_G$ .

First consider the artificial case (commonly used in shear-testing programs) in which we know that exactly one galaxy has been placed in each of many disjoint “postage

stamps” of pixels  $D_i \in D$ . In each stamp, we either obtain a selection with measurement of moments  $M_i$  at some location in the stamp, or we obtain a non-selection. The probabilities of these two outcomes are

$$P(M_i, s|g) = J(M_i) \sum_{G,u} p_G \Delta^2 u \mathcal{L}(X^G) \mathcal{L}(M_i - M^G), \quad (3.37)$$

$$P(\sim s|g) = 1 - P(s|g) \quad (3.38)$$

$$P(s|g) = \sum_{G,u} p_G \Delta^2 u \mathcal{L}(X^G) \left[ J(M^G) Y + 2(\mathbf{C}_M \mathbf{B} M^G)_f \frac{\partial Y}{\partial f_G} + (\mathbf{C}_M \mathbf{B} \mathbf{C}_M)_{ff} \frac{\partial^2 Y}{\partial f_G^2} \right] \quad (3.39)$$

These are the key equations for the BFD calculation. We have made implicit the dependence of the noiseless template moments  $M^G$  and  $X^G$  on the source position  $u$  and the lensing  $g$ . We define as before the Taylor expansions

$$P(M_i, s|g) \approx P_i + Q_i \cdot g + \frac{1}{2} g \cdot \mathbf{R}_i \cdot g, \quad (3.40)$$

$$P(s|g) \approx P_s + Q_s \cdot g + \frac{1}{2} g \cdot \mathbf{R}_s \cdot g, \quad (3.41)$$

where  $Q_i = \nabla_g P(M_i, s)$ , etc., are derived by propagating derivatives through to template quantities  $M^G$  and  $X^G$ . The detection probability  $P(s)$  is integrated over all possible selected moments and all possible galaxies  $G$ , so it does not depend on the data in stamp  $i$ , only on the noise level and PSF of the observation as manifested in the covariance matrix  $\mathbf{C}_M$  in each stamp. For notational simplicity we will assume here that all stamps have the same noise level and PSF and hence the same  $\mathbf{C}_M$ , but the formalism and our implementation allow for variation between targets.

The combined probability of the output of the observation/detection/selection/compression process is

$$P(D|g) = P(\sim s|g)^{N_{ns}} \prod_{i \in \text{selections}} P(M_i, s|g) \quad (3.42)$$

where  $N_{ns}$  is the number of non-selected stamps. We can now calculate the probability of

the lensing variables, following Equation (3.14):

$$-\ln P(g|D) = (\text{const}) - \ln P(g) - g \cdot Q_{\text{tot}} + \frac{1}{2} g \cdot \mathbf{R}_{\text{tot}} \cdot g, \quad (3.43)$$

$$Q_{\text{tot}} \equiv \sum_i \frac{Q_i}{P_i} - N_{ns} \frac{Q_s}{1 - P_s} \quad (3.44)$$

$$\mathbf{R}_{\text{tot}} \equiv \sum_i \left( \frac{Q_i Q_i^T}{P_i^2} - \frac{\mathbf{R}_i}{P_i} \right) + N_{ns} \left( \frac{Q_s Q_s^T}{(1 - P_s)^2} + \frac{\mathbf{R}_s}{1 - P_s} \right) \quad (3.45)$$

We now have all the tools needed to make a lensing inference from a postage-stamp data set. We assume that we have available a *complete catalog of possible galaxies*  $G$  and that for each we have a *noiseless, unlensed image*. In practice of course our template set will be a finite sample from the (infinite) distribution of detectable galaxies. It is essential that the template set is a fair sample of all galaxy types that can meet the selection criteria with non-negligible probability. In other words we must know about galaxies that are outside the flux selection cuts by up to several  $\sigma_f$ .

The input data are: postage stamps of the “observed” galaxies, which we call the *targets*; low-noise postage stamp images of unlensed *template* galaxies to serve as our sample  $G$ ; the PSF for each stamp; and the noise power spectrum  $P_n$  for each stamp. Our testing assumes white noise,  $P_n = n$ .

The procedure is as follows:

1. Select a weight function  $W$  that will be applied to all targets and templates. The best choice will usually be a rotationally symmetric approximation to  $\tilde{T}(k)^2 \tilde{I}_g(k)$ , where  $\tilde{I}_g$  is the transform of the unlensed, pre-seeing image of a galaxy of typical size in the survey.
2. For each template galaxy  $G$ , measure the moments  $X^G$  and  $M^G$  under  $W$  for copies of the galaxy translated over a grid of  $x_G$  centered on the primary flux peak. We can purge from the template set any that have negligible  $P(s|G)$ . Further calculate the first and second derivatives of all moments with respect to  $g$ . (The formulae for these calculations can be found in Appendix C of Bernstein et al. [2016].)
3. For each target galaxy:

- (a) Find the point(s) near the object centroid where the detection criterion  $X = 0$  is met.
  - (b) Calculate the moments  $M_i$  about the detection point(s) and discard those failing the selection cut on the flux moment. After this step we require *no further access to the image data*.
  - (c) If no selection is made, increment the count  $N_{ns}$  of non-selections, and continue with the next stamp. If more than one selection is made, choose the brightest and note that we have violated one of our assumptions!
  - (d) Calculate  $\mathbf{C}_M$  for this stamp.
  - (e) For each target postage stamp  $i$ , calculate  $P_i = P(M_i, s|g = 0)$  from Equation (3.37), and also the derivatives under lensing  $Q_i$  and  $\mathbf{R}_i$ . Since this operation is executed for every target-template pair, it is the computational bottleneck of the procedure. The summand in (3.37) is simple, involving some 4-dimensional matrix algebra and one exponential, so is far faster than an iteration of a forward-modeling procedure. The  $\{P_i, Q_i, \mathbf{R}_i\}$  data fully encapsulate the lensing information from this galaxy and go into our catalog.
4. Calculate the selection probability  $P(s|g = 0)$  from Equation (3.39), and its derivatives  $Q_s, \mathbf{R}_s$  with respect to lensing. Note this needs to be done only once for each distinct  $\mathbf{C}_M$ .
5. Sum the contributions to the posterior –  $\ln P(g|D)$  from detections and non-detections as given in Equations (3.44) and (3.45).
6. Add the Taylor expansion of any prior  $P(g)$  to  $Q_{\text{tot}}$  and  $\mathbf{R}_{\text{tot}}$ .
7. We now have the posterior log probability for  $g$ . The shear estimate and its variance are in Equations (3.18) and (3.17).

### 3.1.5 Poisson-distributed galaxies

For real sky images, we replace the postage-stamp distribution of galaxies with a Poisson distribution. We assume a total unlensed density  $n$  of sources on the sky, with probabilities  $p_G$  of each galaxy being of type  $G$ . If our target survey spans solid angle  $\Omega$  of sky, consider dividing this area up into regions of area  $\Delta\Omega$  larger than the selection region of any single galaxy, but small enough that  $n\Delta\Omega \ll 1$  so that we only have 0 or 1 galaxy in the region after running the detection/selection/compression process across the survey. The probability of obtaining a detection with moments  $M_i$  within any small sky area  $\Delta\Omega$  is

$$P(M_i, s|g, \Delta\Omega) = \sum_G P(M_i, s|g, G)P(G|\Delta\Omega) \quad (3.46)$$

$$= n\Delta\Omega P(M_i, s|g), \quad (3.47)$$

where we take  $P(M_i, s|g)$  from Equation (3.37). Similarly, the probability of selecting a source in a single cell

$$P(s|g, \Delta\Omega) = n\Delta\Omega \sum_G p_G P(s|G, g), \quad (3.48)$$

$$= n\Delta\Omega P(s|g), \quad (3.49)$$

where we use  $P(s|g)$  from Equation (3.39). The quantity  $nP(s|g)$  is the expected sky density of selected galaxies. It depends on  $g$  through the moments of the template galaxies, as per usual.

Our total data  $D$  are reduced to a list  $\{M_i, x_i\}$  for  $1 \leq i \leq N_s$  of the locations and moments of the  $N_s$  selected sources; plus the information that there are no selections at any other locations. The total posterior for  $g$  is now

$$P(g|D) \propto P(g) \prod_{\text{non-detections}} [1 - P(s|g, \Delta\Omega)] \prod_{i=1}^{N_s} P(M_i, s|g, \Delta\Omega) \quad (3.50)$$

$$= P(g) e^{-n\Omega P(s|g)} (n\Delta\Omega)^{N_s} \prod_{i=1}^{N_s} P(M_i, s|g). \quad (3.51)$$

The  $(\Delta\Omega)^{N_s}$  term is independent of  $g$  and can be dropped. We retain dependence on  $n$  since we may wish to consider the source density as a free parameter along with  $g$  if we are simultaneously constraining source clustering and shear. This posterior differs from the postage-stamp case only in the non-selection term. We replace (3.44) and (3.45) with

$$-\ln P(g|D) = (\text{const}) - \ln P(g) - N_s \log n + n\Omega P_s - g \cdot Q_{\text{tot}} + \frac{1}{2} g \cdot \mathbf{R}_{\text{tot}} \cdot g, \quad (3.52)$$

$$Q_{\text{tot}} \equiv \sum_i \frac{Q_i}{P_i} - n\Omega Q_s, \quad (3.53)$$

$$\mathbf{R}_{\text{tot}} \equiv \sum_i \left( \frac{Q_i Q_i^T}{P_i^2} - \frac{\mathbf{R}_i}{P_i} \right) + n\Omega \mathbf{R}_s \quad (3.54)$$

The operative procedure for inferring shear from a sky image is hence identical to that given for the postage-stamp case, except that of course we search the entire image for detections, not just the centers of each stamp. We use the above formulae in step 5 instead of the postage-stamp formulae.

### 3.1.6 Sampling the template space

The BFD method depends upon approximating the full galaxy population with a finite sample of galaxies  $G$  from the sky. In essence we are approximating the continuous distribution of galaxies in the moment space with a set of  $N_G$   $\delta$  functions at a random sampling from the distribution. The measurement error distribution  $\mathcal{L}(M - M^G)$  acts as a smoothing kernel over the samples. While the sums over  $G$  for  $P_i$  (and  $Q_i, \mathbf{R}_i$ ) in Equation (3.37) are unbiased estimates of the complete integrals over moment space, there are two issues we must address.

First, in producing  $Q_{\text{tot}}$  and  $\mathbf{R}_{\text{tot}}$  we divide  $Q_i$  and  $\mathbf{R}_i$  by  $P_i$ . As noted in BA14, division by a noisy estimator for  $P_i$  produces a bias that scales inversely with the number of template galaxies contributing significantly to the  $P_i$  sums. The number of galaxies we can measure at sufficiently high  $S/N$  to use as templates will be limited by scarce observing time. Fortunately we can increase the density of templates in moment space by exploiting the rotation and parity symmetry of the unlensed sky: for each  $G$  that we observe, we can

assume that rotated and reflected copies of this galaxy are also equally likely to exist. In practice we partition  $p_G$  among such copies and add them to the template set. We will investigate in Section 3.4.7 the bias resulting from finite template sampling.

Second: because our  $M$  consists of un-normalized moments, the spacing between template galaxies in moment space will become large compared to the measurement error ellipsoid described by  $\mathbf{C}_M$  when we observe target galaxies at high  $S/N$ . Bright targets can easily end up with no templates for which  $\mathcal{L}(M - M^G)$  is non-negligible. Even worse, the  $P_i$  sum for a galaxy can be dominated by a single template that is many  $\sigma$  away from the target in moment space, and this produces large derivatives in  $\ln P(M_i, s)$  with respect to  $g$ , giving spuriously large influence in the final lensing estimator. It is further true that brighter galaxies are rarer on the sky, so our template survey will contain fewer sources with flux comparable to our brighter targets.

It is therefore advantageous to *add noise to the moments measured for bright galaxies*. One may question the sanity of adding noise to hard-won signal, but note that weak shear (magnification) measurements accrue uncertainty from the intrinsic variation of galaxy shapes (sizes) as well as from the measurement noise in these quantities. Typically, once  $S/N \gtrsim 20$ , the intrinsic variation of the population is the dominant form of noise. So a resolved galaxy with  $S/N \approx 75$  loses little lensing information if degraded to  $S/N \approx 25$ . However if we triple the noise, the likelihood function will “touch”  $3^4 \times$  more template galaxies in our 4-dimensional  $M$  space, so we can reduce template sample variance and bias by increasing noise.

We must be careful to implement this process such that  $P(M, s|G, g)$  remains calculable for both the bright galaxies and faint ones. Again this is best done by using the moments themselves to decide whether to add additional noise. The procedure that we use is as follows; the altered formulae for  $P(M, s|G, g)$  when noise is added can be found in Appendix A of Bernstein et al. [2016].

1. We establish bounds  $f_1$  and  $f_2$  on the galaxies to which we wish to add noise, based on comparing the density of templates with the covariance matrix  $\mathbf{C}_M$  of the

measured moments.

2. We detect, measure, and select target galaxies the same way as described in Section 3.1.4, in the flux range  $f_1 < f < f_2$ .
3. For each selected galaxy, we form a new moment vector  $\mathcal{M} = M + M_A$ , with  $M_A$  drawn from a multivariate Gaussian with zero mean and predetermined covariance matrix  $\mathbf{C}_A$ . We make no further use of the original moments  $M$ .
4. We proceed with the analysis as before, with the exception that  $P(\mathcal{M}, s|G, g)$  is used in place of our previous  $P(M, s|G, g)$ . Note the probability  $P(s|g)$  of galaxy selection in Equation (3.39) remains accurate, since selection is made before adding noise to the moments.

More generally we may define a series of  $b$  flux bins by bounds  $f_0, f_1, \dots, f_b$ , and choose for each bin a distinct covariance matrix  $\mathbf{C}_A$  for the added noise (presumably adding zero noise in the lowest-flux bin). For each target galaxy we calculate  $P(\mathcal{M}, s|G, g)$  using the value of  $\mathbf{C}_A$  we have applied. The non-selection term  $P(s|g)$  is calculated using  $f_{\min} = f_0$ ,  $f_{\max} = f_b$ . The only requirement on the added noise is that it obey the condition  $\text{Tr}(\mathbf{B}\mathbf{C}_A) = 0$  which holds for stationary noise.

## 3.2 Implementation

We have implemented the BFD shear inference in C++ code. The computational bottleneck of the BFD method is the evaluation of  $P(M, s|G, g)$ , which must be done for each target-template pair. A survey like *DES* might detect  $\sim 10^{8.5}$  galaxies, and use  $\sim 10^{4.5}$  templates, each replicated over  $\sim 10^4$  different translations and rotations, leading to  $\sim 10^{17}$  evaluations of  $P(M, s|G, g)$ .

Substantial speedup is attained if we can rapidly cull the templates to those which make significant contributions to the sums for  $P_i, Q_i$ , and  $\mathbf{R}_i$ , *i.e.* eliminate those highly suppressed by the Gaussian exponential in Equation (3.37). In this Section we describe

some shortcuts to reduce the scale of the problem, and an efficient algorithm for culling the target-template pairs, which leads to an implementation that is feasible to run on modest present-day hardware for even the largest foreseen surveys.

### 3.2.1 Computational shortcuts

The target galaxies all have  $X = 0$  by definition of the detection criterion, and so we may first eliminate any template with small  $\mathcal{L}(X^G)$ , a criterion we use to bound the displacements  $u$  at which we replicate the templates. Furthermore we have the freedom to rotate the coordinate axes for each target by the angle  $\beta$  which sets one of the ellipticity moments  $M_x = 0$ . We must rotate  $\mathbf{C}_M$  into this frame, and make sure to rotate all the  $Q_i$  and  $\mathbf{R}_i$  back to the original coordinate system after each is calculated. The unlensed population must be invariant under coordinate rotation, so we do *not* have to rotate the  $M^G$ . With this procedure, we can prune the templates to those that are within  $\sim 6\sigma$  of  $M_x = 0$ . The space  $M^G, X^G$  of template moments is now bounded to a small interval near the origin in 3 of its 6 dimensions.

### 3.2.2 $k$ -d tree algorithm

In building the prior we need to efficiently identify template galaxies with moments  $M^G$  that are close, in moment space, to a given target galaxy  $M$ . The relevant equation is

$$\chi^2 \equiv \left( M - M^G \right)^T \mathbf{C}_M^{-1} \left( M - M^G \right) \leq \sigma_{\max}^2. \quad (3.55)$$

We must be careful in choosing  $\sigma_{\max}$  so that truncation of the integral does not bias  $g$ ; but the number of sampled template galaxies, and the execution time of the measurement, will scale as  $\sigma_{\max}^6$ .

We choose to store the moments of the template galaxies in a  $k$ -d tree [Bentley, 1975], which partitions the templates into distinct  $k$ -dimensional rectangular nodes that allow for fast lookup of points satisfying (3.55). The  $k$ -d tree is built by assuming a nominal covariance matrix  $\mathbf{C}_N$  that is close enough to the  $\mathbf{C}_M$  of the targets that the set of templates

satisfying (3.55) with  $\mathbf{C}_N$  includes all those which do for  $\mathbf{C}_M$ , and not many more. To reduce the number of computations, we do a Cholesky decomposition  $\mathbf{C}_N^{-1} = \mathbf{A}^T \mathbf{A}$ , and rescale the template and target moments to  $N \equiv \mathbf{A}M, N^G \equiv \mathbf{A}N^G$ . This transformation yields  $\chi^2 = |N - N^G|^2$ , the Euclidean distance in  $N$ . The  $N$  are used only to isolate the relevant templates, not to calculate the probabilities.

We need to replicate each template at a grid in  $u$  and rotation angle. The step sizes in translation and rotation are chosen such that  $N^G$  shifts by  $\approx \sigma_{\text{step}} \lesssim 1$  between each grid point. Parity-reversed copies are also made. The probability  $p_G$  of each template is shared equally between its copies. We discard template copies that have no chance of satisfying Equation (3.55) for any selected target galaxy (remembering that all selected targets have  $X = 0$ ,  $M_x = 0$ , and  $f_{\min} < M_f < f_{\max}$ ).

The derivatives of  $M^G$  with respect to shear are calculated for all retained templates. If all the target galaxies have the same covariance matrix, a number of numerical factors can be precomputed so that they do not need to be recalculated for every template/target pair. Note that a new template set needs to be constructed, and the  $k$ -d tree partition repeated, if the target  $\mathbf{C}_M$  changes by more than  $\approx 10\%$ . The construction of the template tree scales as  $N_G \log N_G$ , where  $G$  is the number of templates, which is subdominant to the time  $N_t N_G$  for integrating the  $N_t$  targets over the template set.

After the tree has been constructed, we find for each target galaxy all the nodes that contain template galaxies with  $\chi^2 < \sigma_{\max}^2$  using the nominal  $\mathbf{C}_N$ . If the number of templates in the retained nodes exceeds  $3N_{\text{sample}}$ , we randomly subsample a fixed number  $N_{\text{sample}}$  of them according to their probabilities  $p_G$ . This keeps us from wasting time calculating huge numbers of template/target pairs for targets with large uncertainties, while making full use of the templates that resemble the rarer targets. With this list of template/target pairs, we can calculate the  $P, Q$ , and  $\mathbf{R}$  values needed. The speed of the integration step now scales as  $N_t N_{\text{sample}}$  if the number of templates becomes large.

Our implementation executes the integration over templates for  $\approx 10$  galaxies per second per core on a general-purpose cluster, for the GALSIM simulations below in which

each target is compared to  $\approx 40,000$  templates. At this speed, a 1000-core cluster could measure  $10^9$  target galaxies (*e.g.* the LSST survey) in just 1 day, probably much faster than the subsequent cosmological inferences will require.

While the BFD method has no parameters to tune to reduce bias, the sampling/integration algorithm has three free parameters— $\sigma_{\text{max}}$ ,  $\sigma_{\text{step}}$ , and  $N_{\text{sample}}$ —which trade computational speed and memory requirements against the bias induced by finite sampling. The number  $N_G$  of templates sampled from the sky also will be important in controlling finite-sample biases.

### 3.2.3 Weights and PSFs

The weight function  $W(|k^2|)$  used in calculating the moments of Equation (3.7) must satisfy two requirements: first, it must vanish at any  $k$  where  $\tilde{T}(k) = 0$ , in order to keep measurement errors finite; and it must have two continuous derivatives in order for the shear derivatives of the template moments to be calculable (see Appendix C of Bernstein et al. [2016]). With these conditions satisfied, BFD is well-defined and unbiased, but further refinement of  $W$  can optimize the noise on the inferred  $g$  and the required size of “postage stamp” of pixels for the DFT around each galaxy. In our validation tests we use this “ $k\sigma$ ” weight function:

$$W(|k^2|) \equiv \begin{cases} \left(1 - \frac{k^2 \sigma^2}{2N}\right)^N & k < \frac{\sqrt{2N}}{\sigma} \\ 0 & k \geq \frac{\sqrt{2N}}{\sigma} \end{cases} \quad (3.56)$$

with  $N = 4$ . This closely approximates a Gaussian with width (in  $k$  space) of  $1/\sigma$ , but goes smoothly to zero at finite  $k$ .

In our validation tests we assume we have a noiseless, Nyquist-sampled postage stamp of the PSF from which we can measure  $\tilde{T}(k)$  on a discrete grid of  $k$ . If we require  $\tilde{T}$  at other values of  $k$ , we interpolate the prescription for zero-padding in real space and quintic polynomial interpolation in  $k$ -space given by Bernstein and Gruen [2014]. This need arises if there is distortion across the image such that either targets or templates are sampled at slightly different pitch than the PSF.

### 3.3 Validation Tests

To verify that our implementation of BFD can infer shear with an accuracy of  $|m| \lesssim 10^{-3}$ , we use two types of simulated data. The “Gauss tests” use Gaussian galaxies, a  $\delta$ -function PSF, and a Gaussian  $W(|k^2|)$ , in which case we can calculate all moments and their shear derivatives analytically—no rendering of images is done, so this is fast and bypasses any issues related to image discreteness. The second validation test, the "GALSIM test," uses simulated galaxy images produced with the Python/C++ software GALSIM [Rowe et al., 2015].<sup>4</sup>

Table 3.1 gives the parameters of the two validation simulations. While they use different methods to generate “observed” moments for the target and template galaxies, they use the same integration code. Both simulations proceed as follows:

1. A common galaxy generator is used to generate target and template samples, with shear and noise being applied only to the targets. The galaxies are sampled from a uniform distribution in  $S/N$  (Gauss test) or flux (GALSIM test) between specified limits. The galaxy half-light radius  $r_{50}$  is also drawn uniformly between two bounds. The (unlensed) ellipticity  $e = (a^2 - b^2)/(a^2 + b^2)$  of the source is drawn from the distribution

$$P(e) \propto e(1 - e^2)^2 \exp(-e^2/2\sigma_e^2) \quad (3.57)$$

and the galaxy position angle is distributed uniformly. Galaxy origins are randomized with respect to the pixel boundaries (if any).

2. A “batch” of measurements is made by generating  $N_{\text{batch}}$  target galaxies with a constant shear  $g$ , adding noise, and measuring moments about the origin which yields  $X = 0$ . Those passing any selection cuts are integrated against  $N_{\text{template}}$  template galaxies drawn from the same generator, each of which is translated, rotated, and reflected as described above. The  $P_{\text{tot}}$ ,  $Q_{\text{tot}}$ , and  $\mathbf{R}_{\text{tot}}$  for the batch are saved.

---

<sup>4</sup><https://github.com/GalSim-developers/GalSim>

3. Batches are processed until we have generated the desired number  $N_t$  of target galaxies. Note that each batch draws an independent set of templates. The final shear estimate and its uncertainty are derived from the summed  $P, Q, \mathbf{R}$  using Equations (3.18) and (3.17).

### 3.3.1 Gauss tests

We use the analytic moments of the Gauss tests to check the BFD formulae and their implementation, and explore the sampling parameters of the integration algorithm. Table 3.1 describes the baseline simulation; in Section 3.4 we investigate dependence of shear bias on these parameters using the Gauss tests. Although the moment calculations are analytic, we use the full  $k$ -d tree implementation described in Section 3.2.2 to evaluate the integrals. We can quickly run a sufficient number of statistics to reach the accuracy of  $m \sim 10^{-3}$  using these analytic simulations.

Galaxy moments  $M^G$  (and their shear derivatives) are calculated analytically, and the moment noise  $M^n$  is generated from the multivariate Gaussian distribution with the known  $\mathbf{C}_M$ . A complication is that the moment noise is held fixed as we shift the target coordinate origin to null the  $X$  moments. This is contrary to the behavior of normal images, and results in some changes to the formulae for  $P(D|g)$  which are described in Appendix B of Bernstein et al. [2016]. The baseline Gauss test with  $10^9$  targets yields  $m = (+0.1 \pm 0.4) \times 10^{-3}$ .

### 3.3.2 GALSIM Tests

The GALSIM tests validate several aspects of the code that are not exercised in the Gaussian tests, primarily the measurement of moments and PSFs from pixelized images. The GALSIM code is used to produce FITS images, each consisting of  $100 \times 100$  postage stamps that are  $48 \times 48$  pixels in size. Every stamp contains one galaxy, the sum of an exponential disk and a deVaucouleurs bulge, located near its center. Both components are

Table 3.1. Parameters and results of the baseline validation tests

Characteristic	Gauss test	GALSIM test
Galaxy profile	Gaussian	Decentered disk+bulge
PSF profile	$\delta$ -function	Moffat, $\beta = 3.5$
PSF size (pixels)	...	$r_{50} = 1.5$
PSF ellipticity	...	(0.00, 0.05)
Weight function	Gaussian	$k\sigma$ , eqn. (3.56)
Weight size	$\sigma = 1$	$\sigma = 3.5$ pix
Galaxy radius <sup>1</sup>	0.5–1.5	1.0–2.0
Galaxy $S/N$	5–25	5–25
$\sigma_e$ , galaxy shape noise	0.2	0.2
Selection cuts	none	$8 < S/N < 20$
$N_{\text{batch}} / N_{\text{template}}$ , target/templates per batch	$10^6 / 3 \times 10^4$	$5 \times 10^5 / 2.5 \times 10^4$
$\sigma_{\text{max}} / \sigma_{\text{step}}$ , template truncation/replication	5.5 / 1.0	6.0 / 1.1
$N_{\text{sample}}$ , templates subsampled	$7 \times 10^4$	$5 \times 10^4$
$N_t$ , total targets	$10^9$	$10^9$
Selection fraction	1.0	0.69
$g_{\text{true}}$ , input shear	(0.01, 0.00)	(0.02, 0.00)
$(g_{\text{meas}} - g_{\text{true}}) \times 10^5$	$(+0.1, +0.0) \pm (0.4, 0.4)$	$(+4.3, -1.3) \pm (0.9, 0.9)$
Non-linearity $\alpha$	2	0.5

<sup>1</sup>Galaxy half-light radius is given relative to the weight scale for Gauss tests, or relative to the PSF half-light radius for GALSIM tests.

given the same ellipticity and half-light radius. The fraction of flux in the bulge component is uniformly distributed between 0 and 1. The center of the bulge is randomly shifted with respect to the center of the disk by a distance up to the half-light radius. For our simulated target galaxies, we apply a lensing shear  $\vec{g}$ . We convolve the final galaxy with an elliptical Moffat PSF. Gaussian noise is applied to the final stamp images for targets, but not to the simulated templates. A selection of targets and templates used in this test is shown in Figure 3.1.

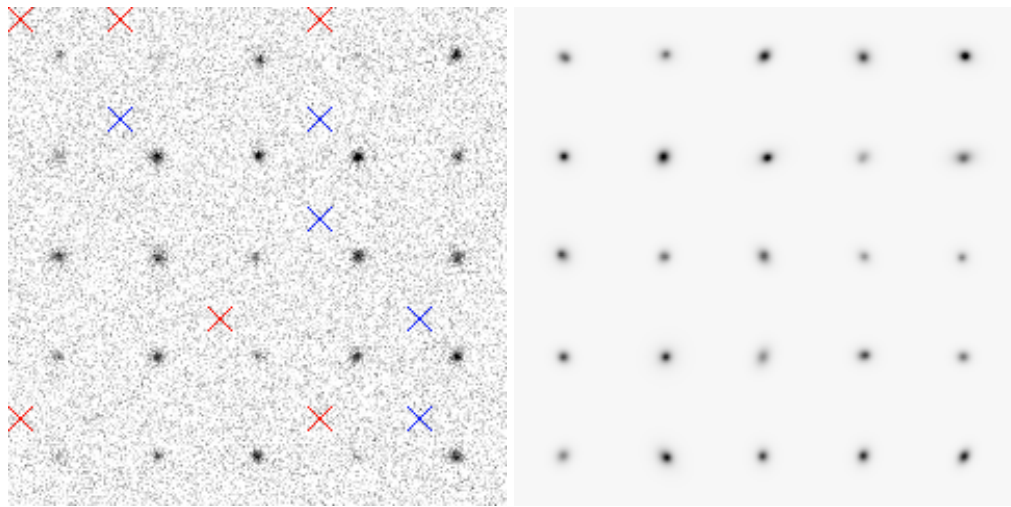


Figure 3.1: A sample of the target (left) and template (right) simulated galaxies used in the validation test. Targets are marked here with an X in the upper left of their stamp if they were cut for low (red) or high (blue)  $S/N$ .

The range of flux assigned to galaxies is set such that it yields  $5 < S/N < 25$  for a circular galaxy of typical size under matched-aperture detection. In measuring shear, we set selection bounds  $f_{\min} = 8\sigma_f$ ,  $f_{\max} = 20\sigma_f$ . Note that the selection uses a different definition of  $S/N$  than the generation. At fixed flux, the selection favors more compact and more circular galaxies.

The properties for these simulated galaxies were chosen to capture the non-idealities of real data which might affect the BFD implementation:

- We give the PSF an ellipticity  $e_2 = 0.05$ , which will test our ability to reject PSF

asymmetries.

- The Moffat PSF is not strictly band-limited so the data are slightly aliased. The PSF half-light radius of 1.5 pixels yields a sampling equivalent to *DES* imaging in seeing with FWHM of 0.8”, which would be in the worst-sampled quartile of the data.
- The decentering of the disk and bulge components breaks the perfect elliptical symmetry of the galaxies, which might otherwise be canceling some systematic error in the method.
- Elliptical Gaussians are a six-parameter family, and hence a given point in the 4d  $(\vec{M}^G, \vec{X}^G)$  space has only a single possible value for the shear derivatives. The varying bulge fraction and bulge/disk misregistration in the **GALSIM** simulations admit a range of shear derivatives at each point in moment space.
- These tests include a non-trivial selection function and hence test the validity of the BFD terms for non-selection.

We produce a total of  $N_t = 8.6 \times 10^8$  targets, of which a fraction 0.69105 pass the flux selection test. The calculated  $P(s)$  predicts this extremely well:  $0.69111 \pm 0.00006$ . The uncertainty on  $P(s)$  arises from sampling noise in the template set.

Most importantly, the inferred values for  $g_1$  and  $g_2$  imply

$$m = (+2.1 \pm 0.4) \times 10^{-3}, \quad (3.58)$$

$$c = (-1.3 \pm 0.9) \times 10^{-5}. \quad (3.59)$$

We detect a deviation from  $m = 0$  at  $5\sigma$  significance: well below that demonstrated by any previous practical method. The  $c$  value is within  $1.5\sigma$  of zero, and suppresses the input PSF ellipticity by a factor of  $> 3000$ .

If we omit the selection terms in Equations (3.44) and (3.45), we obtain  $m = -0.0122 \pm 0.0004$ . The selection term is clearly necessary for part-per-thousand shear inference, and the BFD formalism appears to calculate the correction to 20% accuracy or better.

Lastly we can assess the accuracy of the code’s internal estimates of the uncertainty on the shear estimator. The standard deviation of the  $g$  components derived from each batch of targets is  $(3.56 \pm 0.04) \times 10^{-4}$ , consistent with the internal error estimate from (3.17) of  $3.58 \times 10^{-4}$ .

## 3.4 Testing approximations

We collect here all the assumptions and approximations that have been made in deriving the lensing inference formulae:

1. We have implicitly assumed that we know  $\tilde{I}(k)$  at all values of  $k$  non-vanishing  $\tilde{T}(k)$ , in other words that we have a Nyquist-sampled real-space image.
2. The pixel noise  $D^n$  is stationary and independent of the underlying galaxy  $G$ , and the moment noise likelihood is a multivariate Gaussian.
3. The Jacobian determinant  $J = |dX/dx_0|$  is positive at any location where there is non-negligible probability of selection
4. Galaxies are uncrowded, in that no other galaxies contribute significantly to  $M$  or  $X$  at any location  $x$  where galaxy  $G$  might be selected.
5. The lensing is weak, so that a second-order Taylor expansion about  $g = 0$  captures all information about  $P(M|g)$ .
6. Our template set  $G$  is a complete sample of source galaxies.
7. We have a noiseless, unlensed image of each template.

In this Section we will describe our progress to date in verifying that failures of these assumptions or approximations will not stand in the way of achieving part-per-thousand inference of  $g$ . Also: our `GALSIM` simulation results, while very good, are still imperfect, with  $m$  measured  $5\sigma$  deviant from zero. So we are interested in whether any of these approximations could be responsible for this deviation.

### 3.4.1 Nyquist sampling

We have implicitly assumed Nyquist sampling of the data by defining our moments as integrals over the regions of  $k$  space with non-vanishing  $W(|k^2|)$ . We will not in this chapter examine the consequences of aliasing in the data due to finite sampling. We do note, however, that the method does not require that the data be available at all  $k$  or even that it be free of aliasing. We can *define* our  $M$  elements to be sums over a finite sampling of  $k$  space, and the formalism remains valid as long as we know what the template galaxies'  $M^G$  would be under the same sampling, and also know the first two derivatives of  $M^G$  with respect to lensing distortion  $g$ . This is true even in the case of aliasing, as long as the templates are aliased in the same way as the targets. This, however, is hard to arrange in practice, and it is better to construct un-aliased data from dithered images if necessary, as described in a simple case by Lauer [1999] and in a more general case by Rowe et al. [2011].

Note also that the Moffat PSF used in the validation tests of Section 3.3 is not strictly band-limited, so these tests incurred a level of aliasing that would be typical for a well-designed ground-based survey. In future tests we will evaluate whether this aliasing, or some other approximation in the GALSIM rendering, is causing the non-zero  $m$  value in the GALSIM tests.

### 3.4.2 Stationary noise

The assumption of stationary, source-independent noise is valid for background-limited (or read-noise-limited) imaging, which will generally be the case for the galaxies dominating the lensing information in ground-based weak-lensing surveys. We leave for future work the investigation of the impact of shot noise from source photons, which may be relevant for low-background space-based surveys. Our current simulations do not include source shot noise.

### 3.4.3 Convex galaxies

The assumption of positive Jacobian determinant  $J$  for all selectable regions was necessary to render as feasible the analytic integration of selection probability, and also to avoid calculating the joint probability of multiple detections of the same source. We consider two potential modes of failure of this approximation.

First, if the galaxy is sufficiently faint,  $J^G$  is small enough even near its peak that the noise in  $M$  can flip the sign and create a fold in the  $x \rightarrow X$  mapping. Clearly the defense against this is to have the selection threshold  $f_{\min}$  be large enough ( $\gtrsim 5\sigma_f$ ) that  $J^G$  is also large enough to dominate the noise fluctuations. Further work is needed to determine if there is a level of  $f_{\min}$  which satisfactorily suppresses noise detections without discarding sources that carry a significant fraction of the lensing information.

Second, there will be galaxies which have high flux but have complex structure such that  $J^G$  crosses or approaches zero because of multiple maxima or plateaus. We should note that we only care about the structure in the galaxy *after* it has been smoothed by the detection filter, which in real space is the Fourier transform of  $W(|k^2|)/\tilde{T}(k)$ . We will usually aim to have  $W \approx \tilde{T}^2 \tilde{I}^g$ , where  $\tilde{I}^g(k)$  is the transform of the average observed galaxy. Thus in practice, the observed image, already convolved by the PSF, is convolved again with the PSF and the typical galaxy profile before running the detection scheme. This means that any maxima or plateaus on scales of the PSF or smaller are going to be erased.

We have not yet validated BFD on sources with well-resolved structure that might lead to multiple selections, but our implementation includes some ameliorative measures in anticipation of the issue. First, in our postage-stamp tests, we can discard all but the highest-flux detection in each stamp. Our calculation of  $P(M, s|G, g)$  should then incorporate the probability of a higher-flux selection existing. Our crude version of this is to include in our sum over  $u$  only those values of  $u$  that have  $J^G \geq 0$  and are contiguous with global maximum for  $f$ . In other words we assume that the brightest detection will arise from the convex region of the (filtered) galaxy that surrounds the global maximum.

We have not yet quantified the efficacy of this approach on realistic galaxies.

### 3.4.4 Uncrowded galaxies

Overlapping galaxies pose a considerable challenge for BFD (and indeed for nearly all lensing-measurement methods). We have strived for a formalism that makes minimal assumptions about the morphology of the galaxies. But galaxy image deblending depends fundamentally on having some prior expectations for galaxy morphology in order to partition the flux in a single pixel among two (or more) sources. We suspect that for mild cases of blending, one could precede the BFD analysis with joint model-fitting to multiple overlapping sources; and then, subtract each source model in turn when measuring the Fourier moments of the other. This would likely be successful as long as the subtracted flux has moments that are small compared to the remainder, as our dependence on the correctness of the model will remain weak. At present, we will simply ignore galaxies which overlap to an extent that they grossly perturb each other's moments. Crowding remains as a critical issue for deep ground-based surveys, where the product of typical observed galaxy size and desired target number density is  $\gtrsim 0.1$  [Chang et al., 2013].

### 3.4.5 Weak lensing limit

Any shear estimator that is analytic in the input shear and introduces no preferred direction on the sky should have

$$\langle g_{\text{meas}} - g_{\text{true}} \rangle = [m + \alpha g^2 + O(g^4)] g_{\text{true}}. \quad (3.60)$$

The coefficient  $\alpha$  is expected to be of order unity unless  $d \log P/dg$  becomes large for some targets. This will occur only for galaxies whose moments are many  $\sigma$  different from any of the templates, a situation we avoid by adding noise to high- $S/N$  targets. If  $\alpha \sim 1$ , then the desired accuracy of  $< 10^{-3}$  of the shear will be lost in the second order Taylor expansion about  $g = 0$  for  $g \gtrsim 0.03$ . Expanding around  $g \neq 0$  greatly complicates the calculation of the moments and their derivatives, making it impractical. BA14 derive

third-order expressions, but these are not included in our present implementation and would also slow the method substantially.

Figure 3.2 shows the recovered multiplicative bias as a function of input shear in tests for non-linear behavior of both the Gauss and GALSIM tests. The bias is consistent with the expected quadratic growth with  $g$ , with  $\alpha \approx 2$  and  $\approx 0.5$  in the two cases. A similar result is obtained for a model-fitting implementation of the BA14 method by Sheldon [2014]. The value of  $\alpha$  clearly can vary based on the nature of the galaxies and the noise levels. The  $\alpha = 0.5$  nonlinearity contributes an apparent multiplicative error of  $\alpha g^2 = 0.2 \times 10^{-3}$  to our principal GALSIM test results, smaller than the measurement error even with  $10^9$  target galaxies. But if real cosmic-shear measurements have a value closer to the  $\alpha = 2$  seen in the Gauss tests, the nonlinearity cannot be ignored: The cosmic-shear test is, at its most basic, a measure of the RMS dispersion  $\sigma_g$  of the point distribution function (PDF) of shear to  $z \sim 1$  sources. Propagating (3.60) through a nearly-Gaussian PDF suggests that we would mis-estimate  $\sigma_g$  by a factor  $1 + 3\alpha\sigma_g^2$ , which for  $\sigma_g \approx 0.02$  and  $\alpha = 2$  would be a fractional error of 0.0024 on  $\sigma_g$ , larger than the expected statistical error for future surveys, and in need of a correction. Fortunately the value of  $\alpha$  is straightforwardly assessed to the  $\sim 20\%$  accuracy that would be needed to render nonlinearity errors negligible.

The nonlinearity poses a potentially larger problem for regions of high shear such as galaxy clusters. This problem can be overcome with an iterative procedure if we are fitting a model to the shear. We first fit the model, ignoring nonlinear shear response. In regions of not-so-weak shear, *e.g.* where the shear is  $\approx 0.1$ , we can unshear the source galaxy by the predicted 0.1 shear before measuring its moments and calculating  $P_i, Q_i$ , and  $\mathbf{R}_i$  with the nominal second order procedure. This will yield a Taylor expansion of  $P(D_i|g)$  of deviations from the model, which can then be used to refine the model. We speculate that this procedure would recover full unbiased accuracy around well-measured individual clusters.

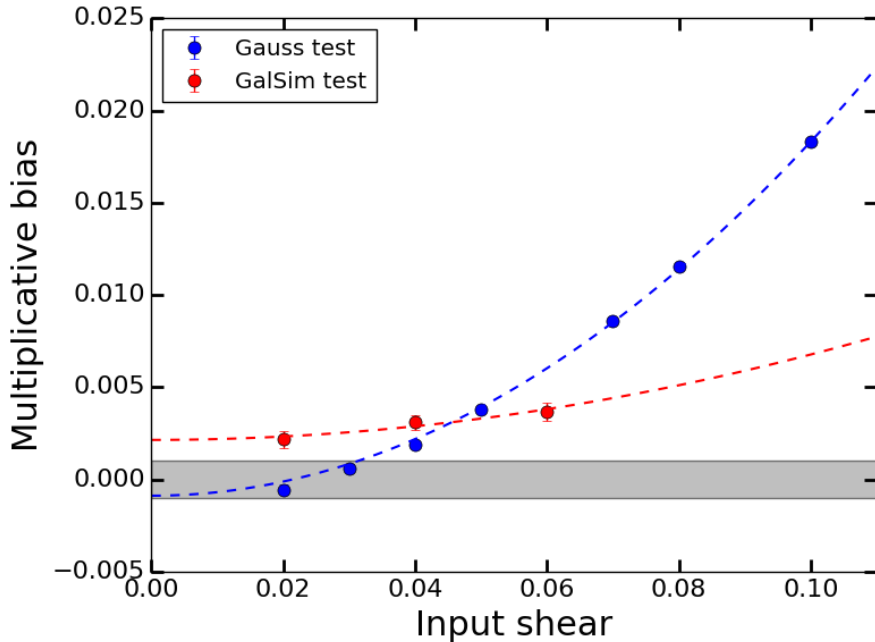


Figure 3.2: The recovered multiplicative bias using the second-order BFD formalism, as a function of input shear. The grey band shows the desired accuracy of  $m < 10^{-3}$ . The dashed line is a fit of the data to the expected quadratic dependence on  $g$ , with coefficient  $\alpha \approx 2$  for the Gauss tests and  $\alpha \approx 0.5$  for the GALSIM tests.

### 3.4.6 Noiseless, unlensed templates

We have assumed that the galaxies used in constructing the prior are noiseless and unlensed, whereas in real data they will be both noisy and lensed by large scale structure. We run a series of Gaussian simulations to evaluate the impact of each of these on shear measurement. In the first test, we add noise to the moments and derivatives of the template galaxies. Figure 3.3 shows the bias in recovered shear as a function of the ratio of template noise variance to target noise variance. When this ratio is  $\sim 10\%$ , the multiplicative bias remains  $< 10^{-3}$ . Therefore, observations with  $> 10\times$  the integration time of target galaxies are sufficiently high- $S/N$  to use as “noiseless” template galaxies. Most current and future lensing surveys already include such deep observations to maximize their scientific value.

In the second test, we assess the impact of using template galaxies that have already been sheared. Recall that we use rotated copies of all observed templates, which means that the *mean* shear on our templates is always zero, but we must ask whether non-vanishing *variance* of the shear on the templates produces biased shear inferences. We applied shear to the templates in two different ways: a constant shear amplitude for every template; and a shear randomly drawn from a zero mean Gaussian with dispersion  $\sigma_g$ . Fig 3.3 shows the bias as a function of the applied template shear. The multiplicative bias satisfies  $|m| < 10^{-3}$  in both cases if the RMS template shear is  $< 0.04$ . The typical shear imparted by large scale structure is only half as large, thus it appears feasible to use deep integrations of the real sky to produce the template set.

### 3.4.7 Complete template set

We approximate the integral over all possible template galaxy types and locations with a finite number  $N_{\text{template}}$  of high- $S/N$  galaxies, and by using a finite number of copies of each at intervals of  $\sigma_{\text{step}}$  in translation and rotation. Further we subsample a number  $N_{\text{sample}}$  of the resultant copies that lie within  $\sigma_{\text{max}}$ , of each target. Ideally, the variance due to these approximations will be far below the expected noise of the targets. BA14 suggest that BFD estimates will have a bias that scales inversely with the number of templates. We again use the Gauss tests to see how sensitive the recovered shear is to  $N_{\text{template}}$  and  $N_{\text{sample}}$ . Figure 3.4 shows that, for the Gauss tests, the bias is within  $|m| < 10^{-3}$  when we have at least 30,000 template galaxies and  $N_{\text{sample}} \gtrsim 70,000$ . The necessary values will in practice depend on how the galaxies are distributed in moment space, how noisy they are, and how we implement the added-noise strategy of Section 3.1.6. These tests suggest, though, that a sample of  $10^4$ – $10^5$  deep sky templates will suffice. This is readily attainable in all planned surveys.

The GALSIM tests reported in Section 3.3 used a value of  $N_{\text{template}} = 2.5 \times 10^4$ . Tests with a  $2.5\times$  smaller value show no significant change in  $m$ , arguing against the hypothesis that our non-zero  $m$  value is attributable to insufficient template sampling. Figure 3.5

shows that for the GALSIM tests, we integrate over a similar number of templates ( $\approx 40,000$ ) for each target. Note that in this case  $N_{\text{samp}}$  was 50,000, so we never invoked the subsampling of accessible templates. An unrealistic aspect of this test is that galaxies are uniformly distributed in flux, leading to uniformity in the number of templates. The real sky has fewer bright galaxies and we would expect the template count to increase for fainter sources.

## 3.5 Future developments

The BFD formalism can be straightforwardly extended beyond the basic single-image, single-plane shear-estimation implementation that we test in this chapter. In this section we sketch some of these possibilities.

### 3.5.1 Interferometric data

Interferometric data is collected in Fourier domain; data for a galaxy will consist of estimates of  $\tilde{I}(k)$  (the visibilities) at a finite sampling of  $k$  values determined by the interferometer baselines. As noted in Section 3.4.1, it is not required that we measure galaxies at all  $k$ : we can replace the integrals over  $d^2k$  in Equation (3.7) with weighted sums over the visibilities. The sole requirement is that we be able to calculate the same sums for the template galaxies, as well as derivatives under lensing distortion.

### 3.5.2 Multi-image analysis and multi-band data

Equation (3.7) defines our compressed measurement vector  $M$  as derived from a single image  $I(x)$  observed with a single PSF  $T(x)$ . In most surveys, observations of a given target will be spread over multiple exposures  $i \in \{1, 2, \dots, N\}$ . As long as each individual exposure is unaliased, we can define the moments of the target as a weighted sum over

the moments  $M_i$  measured on each exposure:

$$M = \sum_i w_i M_i. \quad (3.61)$$

(and likewise for the detection moments  $X$ ). It is important that the  $w_i$  be determined independent of the observed properties of the galaxy, so that the probability  $P(M|G)$  remains calculable. This linear combination of the  $M_i$  yields a zero-mean normal distribution for the moment noise, with covariance matrix  $\mathbf{C}_M$  that is the sum of those for the individual exposures weighted by  $w_i^2$ . Our implementation of this extension selects the weights to minimize the variance of the ellipticity moment  $M_+$ , a process which depends only on the noise level and PSF of each exposure.

Formally, we can choose a different weighting function  $W(|k^2|)$  for each exposure, as long as we can calculate the  $M^G$  that would result for each template (and its lensing derivatives). It is, however, convenient to use the same  $W$  for all exposures, simplifying construction of the template set. If the seeing conditions of the exposures vary widely, then a single  $W$  may be far from optimum for some exposures; but since poor-seeing exposures carry less lensing information to begin with, we lose little by selecting  $W$  to optimize the use of exposures at median or better seeing.

Because we make use of un-normalized moments, it is important that all exposures (including templates) be placed on a common photometric scale.

### 3.5.2.1 Multiple observing bands

There is also no requirement that all exposures be taken through the same filter. Equation (3.61) can refer to exposures in multiple filters. We must once again select weights in advance—iterative procedures such as weighting each galaxy according to its observed colors result in  $P(M|G)$  functions that are analytically intractable. Choosing fixed weights to apply to each filter is akin to measuring moments in a bandpass that is the weighted sum of all the filters' bandpasses.

Another alternative would be to define the moment vector  $M$  to be the concatenation of moment vectors from each filter. This retains more information, though at the

cost of higher memory and computation demands due to the higher-dimensional moment space. We advocate a hybrid procedure, in which we retain distinct flux moments  $M_{f,i}$  for each filter  $i$ , but retain only a single weighted combination of the other moments  $M_r, M_+, M_\times, X$ . This is because shape information is generally highly degenerate between bands [Jarvis and Jain, 2008], but colors carry a lot of information. For example, red galaxies have a more compact shape distribution than blue at low redshift [Bernstein and Jarvis, 2002], so retaining color information when we compress the pixel data allows the BFD formalism to exploit this distinction for more precise shear inference.

Again the key requirement is that a low-noise measure of the template moments  $M^G$  be available, as is the case if the templates are observed in all of the same bands as the targets. One can select distinct  $W$  functions for each band, as long as the targets and templates are treated consistently. An advantage of a fixed  $W$  across bands is that the resultant flux moments then have the same pre-seeing window function on the galaxy in all bands. This property, also attainable with PSF-matching codes, or the GAAP algorithm of Kuijken [2008], is desirable for use with photometric redshifts, since it insures that the measured colors correspond to a fixed weighting of the stellar populations in the galaxy, *i.e.* we are not mixing aperture effects with stellar evolution.

### 3.5.3 Star-galaxy discrimination

Stars are Dirac  $\delta$  functions in real space, so their moments  $M^G$  are known functions of flux and position  $x_G$ . Furthermore they are unaffected by cosmological-scale lensing so we set the lensing derivatives of  $M^G$  to zero. If we add stellar sources to our template set, assigning them  $p_G$  values according to a prior expected sky density vs flux, then we automatically correct the shear estimate for dilution by stellar sources. We obtain as a by-product an excellent posterior estimate of the probability that each source is stellar, and we can sum these to obtain a posterior stellar density estimate which may help to refine the stellar model that led to the prior.

It should also be noted that faint galaxy targets which might be confused with stars

are by definition weakly resolved, and contribute very little to  $Q_{\text{tot}}$  and  $\mathbf{R}_{\text{tot}}$  for shear estimation. Hence the shear estimation will have low sensitivity to mis-estimation of the stellar density in the prior.

If we have observed in multiple filters and retained flux moments  $M_{f,i}$  in each band as described in Section 3.5.2.1, we can (and must) produce stellar templates across the color-magnitude diagram, with  $p_G$  values expressing the expected density vs color and magnitude.

### 3.5.4 Magnification

The BFD formalism makes no assumptions about the nature of the lensing distortion vector  $g$ , except that we can simulate its action on each template, and that  $P(D|g)$  is well approximated by a quadratic Taylor expansion. This means that we can include magnification  $\mu$  along with the shear components  $g_1$  and  $g_2$  with essentially no change except to increment the dimension of the  $Q$  and  $\mathbf{R}$  derivatives.

Huff and Graves [2014] note that early-type galaxies define a narrow plane in the space of flux, size, and concentration, which then enables much-enhanced determination of magnification. Our current BFD implementation would not exploit this gain since our compressed data vector lacks information on concentration. This could be remedied by adding a  $|k^4|$  moment to  $M$ . Furthermore we would need color information, *i.e.* the series of flux moments proposed in Section 3.5.2.1, to distinguish red galaxies in a desired redshift range. There is no need to “teach” BFD about the existence of the Huff-Graves relation. Any such relation that exists will be automatically exploited in the lensing constraints, as long as the action of lensing produces a shift in the way the galaxies populate the moment space.

Two minor technical points about the estimation of magnification: first, Equation (3.52) has assumed that galaxies are placed by a Poisson process. Clustering of sources will mean that the resultant posterior is invalid, underestimating the uncertainty on  $\mu$ . We can, if desired, treat the unlensed density  $n$  as a spatial variable when inferring magnification

statistics, to distinguish clustering from magnification. Second, recall that magnification will dilute the source population on the sky, changing the apparent  $n$ . This effect is already included in our implementation because we calculate the derivative  $\partial M^G / \partial \mu$  by magnifying about the coordinate origin, not the center of the galaxy. This means that our grid  $u$  of template copies is diluted by magnification, but we do not alter  $\Delta^2 u$  in Equation (3.37) or Equation (3.39). Thus source dilation is included in the  $P$  terms, and the  $n$  term should retain the unlensed density.

Higher-order lensing distortions, *i.e.* flexions, can similarly be constrained by the BFD method, again as long as we augment the compressed data vector to include quantities that are altered at first order by the distortion. Since flexion is not an affine transformation, its action on the Fourier domain  $\tilde{I}(k)$  is less easily expressed than shear and magnification. Nonetheless, it is possible to derive flexion derivatives of template moments for simultaneous constraint of all these lensing distortions using BFD.

### 3.5.5 Lensing tomography and photometric redshifts

One important caveat to BFD is that one cannot select subsets of the targets and then combine their  $P_i, Q_i, \mathbf{R}_i$  values to estimate the shear on this subset. This would invalidate the  $P(D|g)$  formulae we have derived, unless one can guarantee that the *post hoc* selection criteria do not at all alter the distribution of underlying moments  $M^G$  of the selected galaxies.

Many useful scientific inferences and diagnostic tests for weak lensing measurements rely upon comparing  $g$  on subpopulations of the sources. Most critically, the bulk of the lensing information, plus constraints on contamination by intrinsic galaxy alignments, require splitting the source population into redshift bins, a.k.a. lensing tomography.

If precise redshift estimates are available for all targets and templates, then the application of BFD is straightforward, as we compare each target only to templates that reside in the same redshift bin. More commonly we have *probabilistic* redshift estimates for targets derived from photometric redshift (photo- $z$ ) estimation. Partitioning target or

template galaxies by their maximum-likelihood redshifts will not, in general, yield valid BFD inferences on the shear in each redshift bin.<sup>5</sup>

This apparent stumbling block turns out to be an opportunity: the BFD formalism contains within it an ideal Bayesian photo- $z$  estimation mechanism, particularly for the sources with modest  $S/N \lesssim 30$  photometry that dominate the weak lensing information in most surveys. Benítez [2000] presents the formalism for Bayesian inference of redshift from broad-band fluxes; like BFD, it relies upon having noiseless data vectors for a sample of “truth” objects of known prevalence on the night sky.

We generalize the BFD method as follows: the lensing vector is extended to the tomographic information  $t = \{g_1, \dots, g_Z\}$ , where  $g_v$  is the lensing distortion applied to sources in redshift bin  $v$  out of  $Z$  total bins. We want the posterior  $P(t|D)$ , and as before we compress the image data  $D$  into the moments  $M_i$  of objects detected and selected at positions  $x_i$ . The posterior on  $t$  is calculable once we have expressions for  $P(M_i, s|t)$  and the total selection probability  $P(s|t)$ . If we know the probability  $p_{Gv}$  that template galaxy  $G$  is in redshift bin  $v$ , then we have the clear generalization of Equation (3.37) to the tomographic case:

$$P(M, s|t) = \sum_{G, x_G} p_G \Delta^2 u \sum_v p_{Gv} P(M, s|G, u, g_v) \quad (3.62)$$

$$P(M, s|G, u, g_v) = |J(M)| \mathcal{L} \left[ X^G(u, g_v) \right] \mathcal{L} \left[ M - M^G(u, g_v) \right] \quad (3.63)$$

In the second line we make explicit the dependence of the template moments on its true position  $u$  relative to the detection location and upon the shear  $g_v$  to the source. The total probability of detection vs  $t$  is similarly obtained by introducing  $p_{Gv}$  into Equation (3.39).

We can also easily calculate the posterior redshift distribution  $P(v|M_i)$  for each source, which would be found equivalent to the treatment of Benítez [2000]. Of course our redshift discrimination will be weak unless we have measured flux moments  $M_{f,j}$  in multiple

---

<sup>5</sup>The same is true for most other lensing-inference methods: the responsivities or empirical calibrations they employ will depend upon the galaxy selection in subtle ways that may thwart part-per-thousand calibration.

bands  $j$  as described in Section 3.5.2.1, where we noted that our pre-seeing aperture-matched fluxes are ideal for photo- $z$  purposes. We also note that we are working with fluxes, not colors, and therefore we automatically include the “luminosity prior” that is often added by hand into photo- $z$  estimators. Indeed our inclusion of  $M_r, M_+,$  and  $M_\times$  means that we automatically exploit any size, surface brightness, or ellipticity information that helps with redshift discrimination.

Extending BFD to return the full tomographic lensing likelihood  $P(t|D)$  would have many advantages for precision lensing cosmology. It would allow us to extract all the available lensing information from galaxies with low-resolution photo- $z$  information due either to color ambiguities or low  $S/N$ . It eliminates the need for *post hoc* estimation of selection biases induced on the lensing estimators by photo- $z$  cuts. An important issue will be whether it is feasible to use sufficiently many, narrow bins that we do not need to worry about the variation of lensing signal across the redshift range of a bin.

The implementation of BFD tomography requires that we have a template galaxy set with known redshift probabilities assigned to each. Clearly one issue is how to obtain this information—especially since the number of templates required to sample the moment space with desired density will increase substantially with additional flux dimensions in  $M$ . It is likely infeasible to obtain spectroscopic redshifts for a sufficiently large and complete set of templates. A survey such as *DES* which observes galaxies in the *grizY* bands requires higher- $S/N$  observations in these bands to create the template moments set; these observations in the survey bands could be supplemented with deep data in other bands and with other instruments to tighten the  $p_{Gv}$  estimates for the template set—for example, the COSMOS field has data in many bands across the EM spectrum, producing much higher-reliability photo- $z$ ’s beyond the spectroscopic limit [Ilbert et al., 2009]. It will likely be necessary to use spectral-synthesis methods to create artificially redshifted copies of the observed template galaxies, just as we synthesize  $M^G$  for rotated copies, in order to more densely sample the template space and damp the line-of-sight structures (sample variance) present in the template fields. We envision BFD primarily as a means

to rigorously bootstrap the photo- $z$  calibration from a well-observed subset of galaxies to the full survey population.

Incompleteness in the spectroscopic surveys defining the redshift priors is a difficult problem [see *e.g.* Bernstein and Huterer, 2010]. The BFD tomography formalism allows us to propagate the uncertainties due to missed redshifts into the final cosmological results: we can reassign the probabilities  $p_{GV}$  using different assumptions about the missing redshifts, and propagate these cases through  $P(t, D)$  into cosmological inferences to determine their impact. One could also add a “mystery bin” to  $t$  to which we assign all template galaxies with poorly known redshift. The tomographic BFD formalism will calculate the likelihood that any given target has unknown  $z$ , and cosmological inferences could marginalize over the redshift distribution of the mystery bin.

Joint BFD tomography and photo- $z$  is clearly an intriguing and critical extension of the method, with quite a few details to work out. We will examine these in future publications.

## 3.6 Conclusion

The BFD method is now a practical, validated means to estimate WL shear at parts-per-thousand accuracy. In our initial large-scale tests, deviations from perfection were measurable only with trials of nearly  $10^9$  simulated galaxies. Work remains to determine if and why BFD has inaccuracies at the level of  $m = 0.002$ . Future work will investigate the possible impact of aliasing, and approximations in the rendering of images onto finite postage stamps, since we find  $m$  consistent with zero for our Gauss tests that do no rendering. PSF asymmetries are perfectly removed from the shear estimator, to present accuracy. We have implemented a flux selection in such a way that we can correct the  $> 1\%$  selection bias induced on the shear. The BFD formalism needs no parameter tuning or calibration to eliminate biases—there is just a free weighting function one chooses to minimize noise. A real implementation does have some parameters for sampling the infinite distribution of galaxies on the sky, which imply a tradeoff of bias vs observational

and computational resources. We have used simulations to validate the performance of the method and demonstrate that the desired accuracy is attainable with readily available resources to sample the underlying galaxy population.

While BFD assumes that noiseless images of unlensed galaxy populations are available, our tests indicate that it retains desired accuracy when the templates are taken from images with the same instrument, but  $\approx 10 \times$  longer exposure time than the target survey. This is eminently practical, and indeed most planned surveys already have such “deep fields” for other reasons.

The BFD method also predicts the uncertainty on the shear estimate, and the detection efficiency, correctly to within the shot noise of our tests. The algorithms should scale to the needs of even the largest proposed surveys, and the computational steps are simple, highly parallel and amenable to execution on GPU’s if greater speed is needed.

Sheldon [2014] reports  $|m| < 2 \times 10^{-3}$  when applying the BA14 formalism to likelihoods derived from MCMC model-fitting to galaxy images with  $S/N$  as low as 10. The galaxy images were both drawn and fitted with simple Sérsic models, so this work notes that the method may be susceptible to “model bias” in more realistic cases. Sheldon [2014] also does not yet include a prescription for galaxy selection and resultant biases.

The only other demonstration of part-per-thousand WL inference at  $S/N \lesssim 10$  from a realistic algorithm of which we are aware is Zhang et al. [2015], also implemented as the FOURIERQUAD method in the GREAT3 challenge [Mandelbaum et al., 2015]. This method shares several characteristics with BFD: galaxies are reduced to weighted moments in Fourier space, where PSF correction is straightforward. Neither method assigns shapes to individual galaxies; FOURIERQUAD works by stacking un-normalized moments of the power spectrum; the shear estimator is a quotient of stacks. Using the power spectrum has the advantage of making the estimator insensitive to choice of galaxy origin, but amplifies measurement noise by  $\sqrt{2}$  relative to our phase-sensitive moments. More problematic is that a stacking method weights galaxies by flux, which is far from optimal. FOURIERQUAD does not yet have an approach to selection and weighting of sources

without biasing shear inferences. BFD is at this time closer to applicability on real data.

Schneider et al. [2015] propose an ambitious effort to simultaneously model the shear field, the pixel-level appearance of galaxies within it, and the underlying distribution of the source galaxies. This approach shares some formalism with BFD, but does ultimately rely on parametric models for the galaxies. Our “model,” which is that galaxies’ true moments are equal to those of galaxies found in a deep sub-survey, should be less subject to model bias than the Schneider et al. [2015] approach while greatly reducing the computational complexity.

There are issues to address before BFD can be applied to real survey data. Working in Fourier space means we cannot easily exclude pixel data contaminated by cosmic rays or defects, and hence we need some method for infill of pixels or rejection of exposures. Overlapping or multi-peaked galaxy images are not handled by BFD, so we will need some combination of model-based deblending with rejection of hopeless overlaps that does not significantly bias WL inferences. This will be easier in low-density surveys such as *DES* and *KiDS* than deep ground-based surveys such as *LSST* and *HSC*. For space-based surveys, we need to investigate the behavior of BFD in the presence of source shot noise that violates our background-limited (stationary) noise assumption. We also may need to develop a nonlinearity correction for some applications.

Our validation tests assume constant shear across all galaxies, but as BA14 point out, it is straightforward to calculate a posterior likelihood on the parameters of any model of shear vs position, for example for tangential shear vs radius around a selected lens population. Cosmological models, however, predict a power spectrum or other statistical property of the WL field rather than predicting the shear pattern itself. Current 2-point (and 3-point) estimators for shear assume that each source galaxy provides a point estimate of the shear, but BFD returns a different kind of information, namely some weak probability distribution for shear along each line of sight in the form of  $\{P_i, Q_i, \mathbf{R}_i\}$ . Exploitation of the BFD outputs for lensing statistics will require development of new estimation frameworks. Madhavacheril et al. [2015] discuss means to treat such outputs

as point estimators, and quadratic estimators for 2-point functions that use BFD-style information.

We have also treated the lensing distortion as a single screen, whereas the sources are distributed in  $z$  and hence we measure a weighted mean of shear on the line of sight. A real experiment will need to estimate the  $z$  distribution of sources—or more precisely, the distribution of contribution to the BFD shear estimate. Better yet, we have outlined an extension of BFD to joint Bayesian redshift and shear estimation, which directly generates a tomographic lensing likelihood  $P(D_i|t)$  for each source where  $t$  contains the shear (and potentially magnification and source density) at a series of  $z$  bins. This could open the door to full exploitation of the low-to-modest  $S/N$  regime—where both photo- $z$  and WL estimators have proven difficult to produce without bias—that potentially carries more information than high- $S/N$  galaxies with well-constrained photo- $z$ 's. Work is needed to develop statistics to constrain cosmological models with this  $P(D_i|t)$  information, as opposed to the binned point estimates used now. It is likely that there are extensions of the Madhavacheril et al. [2015] techniques to this tomographic case.

A critical question will be how many template galaxies must be observed, particularly in the tomographic case where we will need to increase the dimensionality of the moment space that the templates sample. This is related to the question of how large and complete a spectroscopic sample is needed to calibrate photo- $z$ 's to the accuracy needed for WL cosmology.

The BFD method also naturally extends to multi-filter or interferometric observations, and deals gracefully with the blurring of the stellar and galactic loci in faint surveys. Compared to currently dominant model-fitting methods for WL inference, BFD has some disadvantages, such as not-quite-optimal use of the pixel information, annoyances with defective pixels, and a less-clear route to using crowded sources. BFD's advantages are, however, substantial, primarily in the superior accuracy that comes from having a first-principles treatment of noise and selection, and no need to assume a functional form for the sources.

### 3.7 BFD on DES

Since the publication of the above work, some progress has been made towards applying BFD to real DES data, which currently consists of three years of observations. Several improvements and updates to the BFD code have been completed. In new simulations, we use increased postage stamp sizes, resulting in a measured bias that is consistent with zero. The cause of this change is still being investigated. BFD can now also combine results from multiple epochs of observations as well as those from different filters.

Unlike the postage stamp simulations we use to test BFD, real data is littered with blended objects. It is necessary to model these objects and subtract the light from their neighbors in order to measure accurate and unbiased shapes and fluxes. The deblending effort in DES has succeeded in providing the ability to produce stamps of neighbor-subtracted galaxy images to use as inputs to BFD.

The templates required for BFD will in practice be deep images of the same types of galaxies found in the DES wide field. In DES, there are several fields with special observations resulting in significantly deeper images than the wide survey. These fields have increased exposure time and cadence to facilitate the search for transients, mainly supernovae. This collection of deep field objects will provide a set of templates with sufficient variety to describe the wide field population of objects.

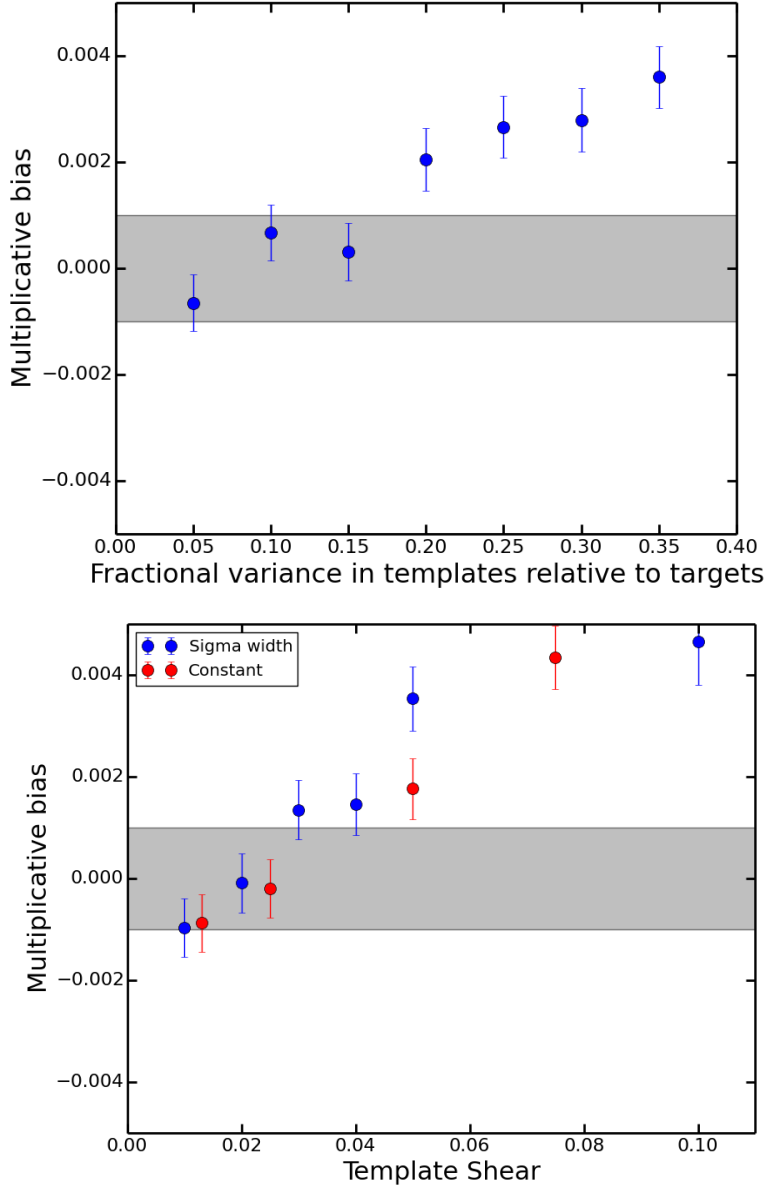


Figure 3.3: Top: the multiplicative bias in shear inferred from simulations where we add noise to the template galaxies. The  $x$  axis gives the noise variance on the templates relative to the noise variance on the target observations. Bottom: the multiplicative bias recovered when template galaxies have an applied shear that is either constant or drawn from a Gaussian of given RMS value. The grey band shows the desired accuracy of  $m < 10^{-3}$ , which we see is retained when the templates have  $\lesssim 10\%$  of the noise power of the targets, and the RMS shear on templates is  $\lesssim 0.04$ .

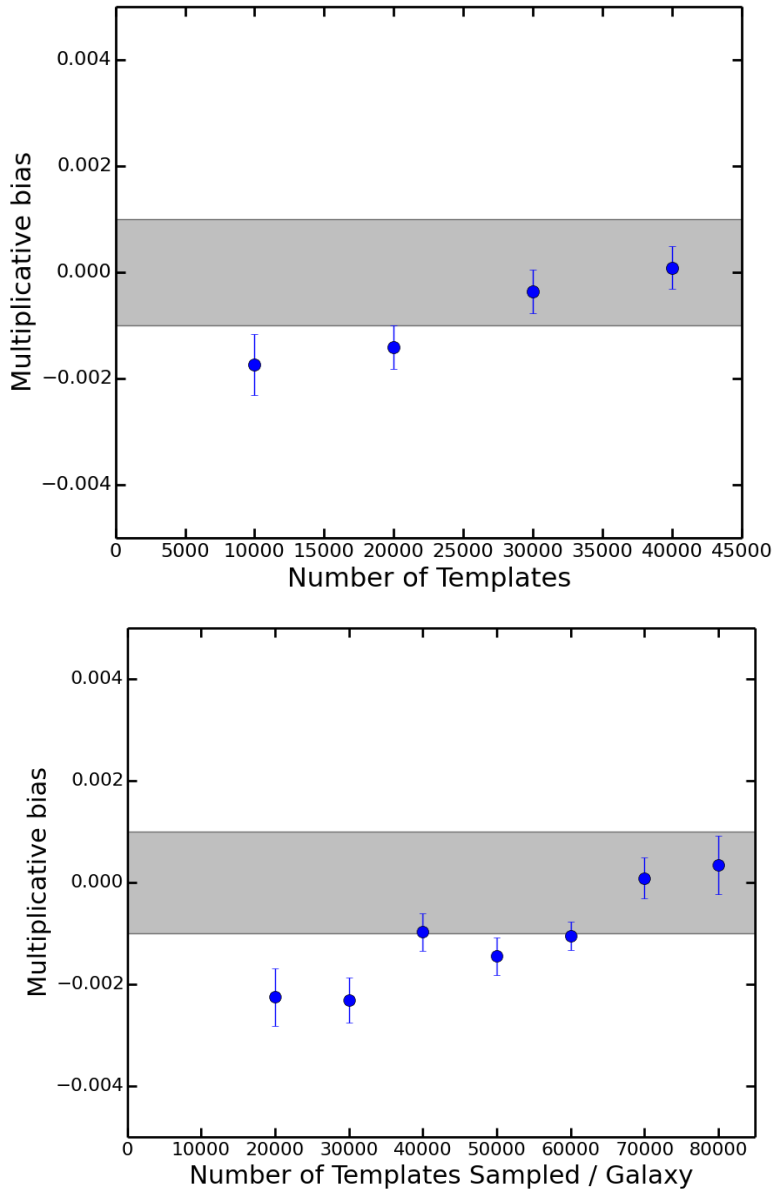


Figure 3.4: The multiplicative bias recovered as a function of the number of initial template galaxies before adding rotated/translated copies (top) and as a function of  $N_{\text{sample}}$  (bottom), the number of subsampled templates used to evaluate the integrals for each target galaxy. The grey band shows the desired accuracy of  $|m| < 10^{-3}$ .

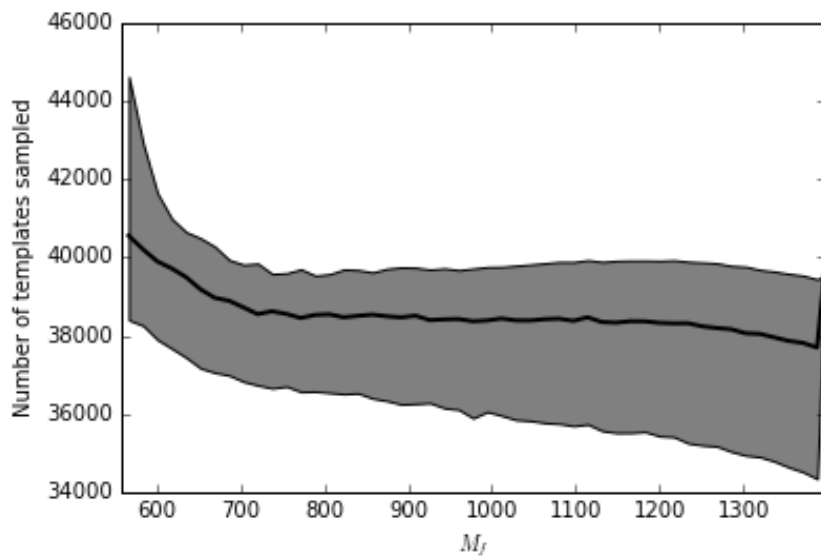


Figure 3.5: The number of templates used in the integration of  $P(D_i|g)$  for each galaxy as a function of its flux moment  $M_f$  in the GALSIM tests. The central line is the median, the shaded region bounds the 10–90 percentile range.

# **Chapter 4**

## **A New Method for Measuring the Cosmic Magnification of High Redshift Galaxies**

As described in Section 1.2.2, magnification bias caused by gravitational lensing alters the observed number density of sources on the sky, and this change is related to the slope of the source luminosity function. It is clear that previous measurements of cosmic magnification using distant sources (Section 1.2.3) have used a somewhat standard procedure that can be summarized as such: create a catalog of potential sources using color selection; remove suspicious objects using some combination of survey flags, visual inspection, and photometric redshifts; calculate remaining low-redshift contamination of the source catalog using simulations or other ad-hoc estimation; count sources around low-redshift lenses; and finally, calculate the correlation function  $w(\theta)$  (proportional to  $\mu(\theta)$ ) and correct for the estimated contamination if necessary. In this chapter, we propose a new and different approach to estimate the magnification  $\mu(\theta)$  of high redshift galaxies in a ground-based photometric survey like the Dark Energy Survey (DES).

## 4.1 Magnification in the Dark Energy Survey

The standard selection method for high redshift sources like Lyman-break galaxies (LBGs, see Section 1.2.3.1) would be especially inefficient in DES for two reasons: the bluest DE-Cam filter used in the wide survey ( $g$ ) is centered around 450nm and is therefore sensitive only to dropouts at redshift  $z \approx 3.5$  and above, as shown in Figure 4.1; and the depth of the survey (expected  $10\sigma i_{mag}=23.5$ ; Dark Energy Survey Collaboration et al. [2016]) is several magnitudes below that of the studies mentioned in Section 1.2.3.

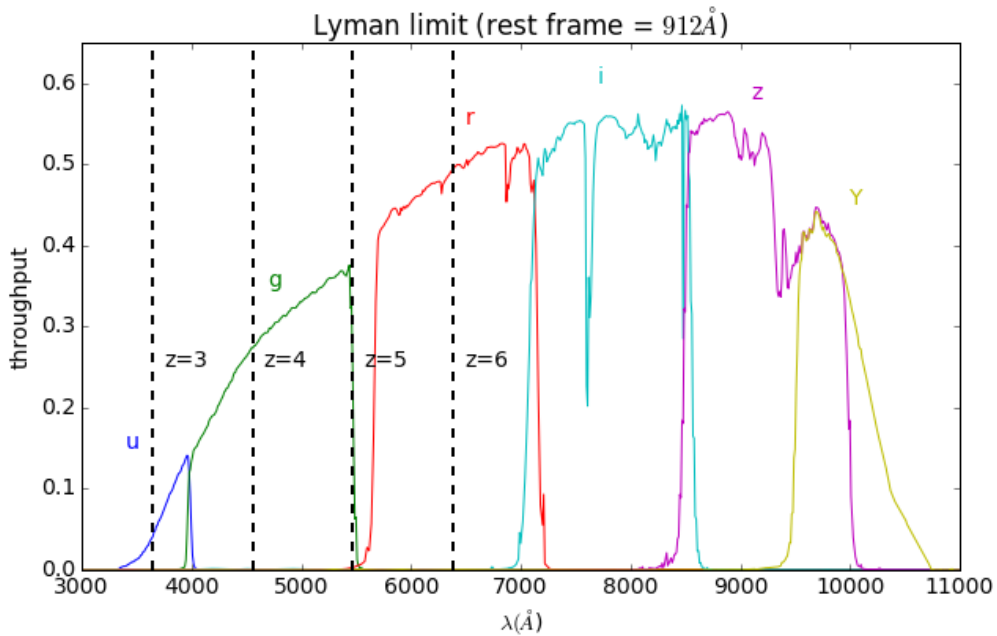


Figure 4.1: DES throughput overlaid with the Lyman break at various redshifts.

Davies et al. [2013] ran simulations similar to those created in Hildebrandt et al. [2009a] using stellar population synthesis models to find the redshift evolution of DES colors for LBGs and possible low-redshift interlopers. They found that the standard color-color cut method could be used to separate objects in DES at redshifts most effectively at  $z \approx 4$  or higher. These results are shown in Figure 4.2. Due to the expected survey depth quoted above, one will find a more significant overlap of LBGs and low-redshift objects

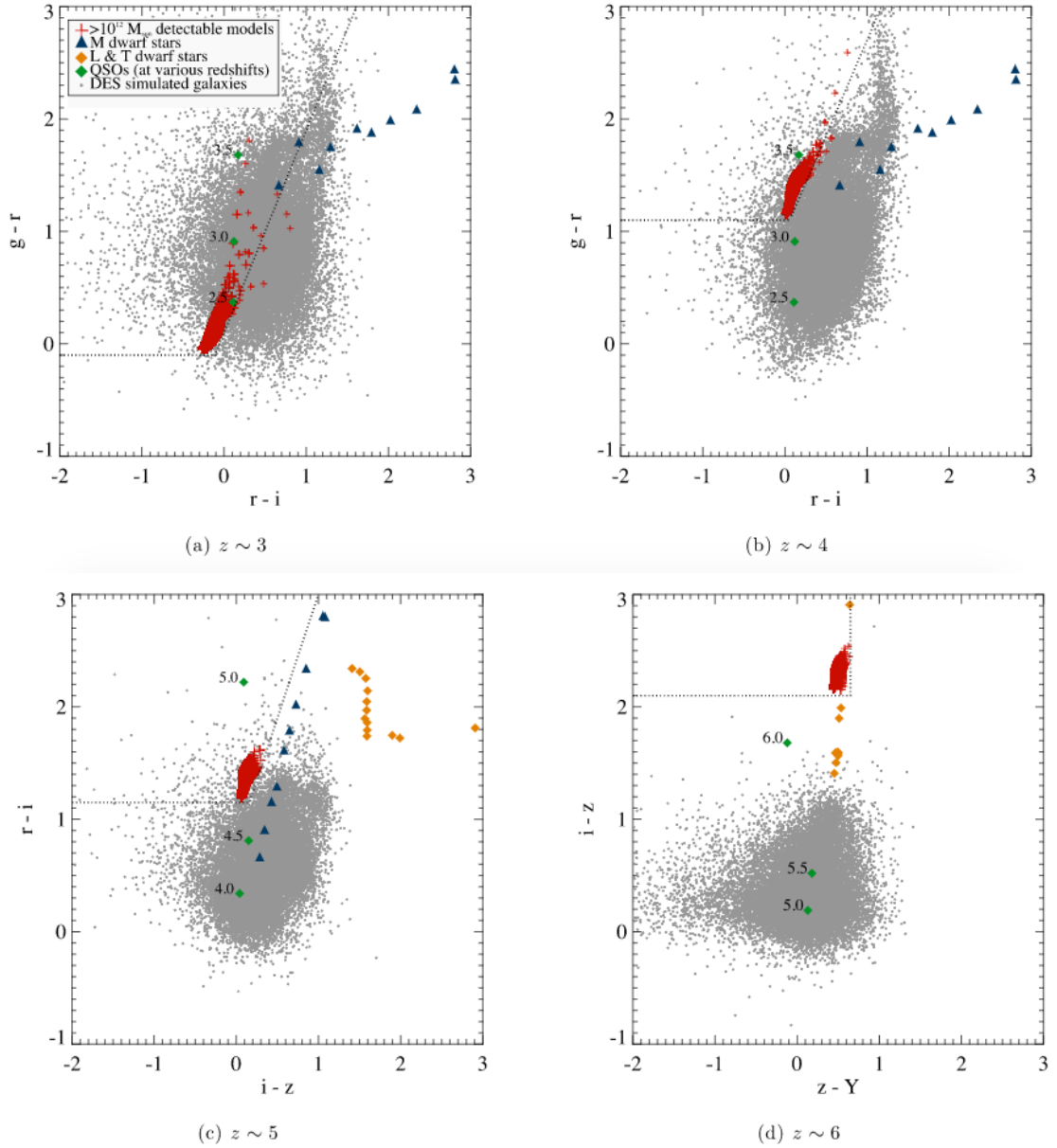


Figure 4.2: Figures from Davies et al. [2013] showing the simulated color tracks for massive galaxies at high redshifts compared to those of various nearby galaxies and stars in DES.

near the color-color cutoff edges due to larger errors in flux estimation of the faint, unresolved objects we are searching for. Hence the cuts suggested by Davies et al. [2013], which are chosen to give an adequately complete sample of LBGs, would require the esti-

mation and strict correction for this contamination as done previously while still missing LBGs beyond the cut and would leave us with too small a sample to make any statistically significant magnification measurements. In addition to these motivating factors for a new method to use with DES, the fiducial LBG selection method has inherent imperfections in its catch-all style, and the *a posteriori* correction for this leaves poorly defined uncertainties in the ultimate measured correlations that have been deemed acceptable thus far in the literature. We seek to combat these issues by improving the accuracy of source selection on an object-by-object basis and account for the uncertainty in this source assignment in the magnification measurement itself.

In the following sections of this chapter, we present an improved Bayesian method for selecting high redshift sources for use in measuring their cosmic magnification (Section 4.2); test this method (Section 4.3); propose the use of simulations to predict the expected magnification of these objects at varying redshift (Section 4.5); and suggest how to accurately estimate the magnification around foreground galaxies by taking the above selection and simulations into account (Section 4.6).

## 4.2 Source Selection

In a photometric survey with multiple filters such as DES, we can calculate the colors of observed objects using any combination of two flux measurements. Since high-redshift galaxies have very distinct colors, analyzing the fluxes of objects in a given catalog should tell us which objects could potentially be classified as such.<sup>1</sup> In fact, we can use existing information about high-redshift galaxies to give us a very well-informed probability that an object is or is not at high redshift. Bayes' Theorem allows us to use this prior information to calculate the probability that a target object with observed flux  $\vec{f}_{obs}$  exists at a redshift  $z$  in the range  $z_{group}$  (where  $z_{group}$  describes a redshift range  $[z_{min}, z_{max}]$ ) of a

---

<sup>1</sup>We will use fluxes instead of magnitudes because the galaxies we seek are faint enough to cause problems with magnitude and error estimation as the error distribution on  $\log(\text{flux})$  is very non-Gaussian.

specific type of galaxy). This probability is calculated as such:

$$P(z \in z_{group} | \vec{f}_{obs}) = \frac{P(\vec{f}_{obs} | z \in z_{group}) P(z \in z_{group})}{P(\vec{f}_{obs})} \quad (4.1)$$

As noted, we require prior knowledge of how flux relates to redshift in the real distribution of objects in the universe. Similar to the scheme described in Chapter 3, this prior can be in the form of an object catalog with well-known redshifts and fluxes. We call these objects “templates.” The template flux measurements should also be significantly more precise than those of our target objects, such that their flux-redshift relationship can be treated as “truth.” We can also start with the assumption that the observed (noisy) measurements of a target’s flux fall in a Gaussian distribution centered on its true underlying value, with the width of this Gaussian defined by the reported flux errors of the target survey. With this assumption, we can calculate the probability in Equation 4.1 as the sum of Gaussian probabilities that the target object is a noisy measurement of each galaxy in our template set; and we can do this calculation for various redshift ranges with templates known to be in the range defined by  $z_{group}$ :

$$P(z \in z_{group} | \vec{f}_{obs}) \propto \sum_{t \in templates_{group}} |2\pi\mathbf{C}_f|^{-1/2} \exp\left(-\frac{1}{2} |\vec{f}_t - \vec{f}_{obs}| \mathbf{C}_f^{-2} |\vec{f}_t - \vec{f}_{obs}| \right) \quad (4.2)$$

Here,  $\mathbf{C}_f$  is the covariance matrix of the observed fluxes, which we will assume to be diagonal with  $\mathbf{C}_{f,ii} = \sigma_i$ . Since we are using these groups to separate lens and source populations in our weak lensing analysis, the choice of redshift ranges should be informed by the redshifts covered by the chosen lens population, as well as binned fine enough to account for the change in the convergence  $\kappa(\theta)$  acting on sources at different distances from the lens.

### 4.3 Testing the Bayesian Source Selection

Before moving on to the estimation of magnification  $\mu(\theta)$ , we will discuss several tests conducted to confirm that the above Bayesian redshift grouping performs as intended,

since this will motivate how we treat possible contamination later. Since we will be using the method on real data, we want to test the assumptions we have made and confirm that they can be applied to actual observations. The first assumption is that the fluxes and errors reported by SExtractor<sup>2</sup> are true representations of the object's properties.

### 4.3.1 Flux Errors

Equation 4.2 relies on the assumption that for a given target object, the probability of measuring  $\vec{f}_{obs}$  follows a Gaussian distribution centered around the true, unknown flux of the target with a  $1\sigma$  width matching the reported flux errors. In a survey like DES, we seek to know if the actual error distributions follow this idealized probability, and how badly our posteriors are affected if we assume the wrong error function.

To explore this question, we need two sets of data for the same list of targets: a set of "true" fluxes and a set of fluxes that have been observed with some uncertainty. For this, we use DES catalogs derived from different stacks of observations of the same field, yielding catalogs with varying noise levels for identical sources. These DES catalogs are called D04, D10, and DFULL (hereafter D\*), depending on the number of exposures (4, 10, and all available) used. The intent behind their creation is to mimic the Year 1 (Y1) and Science Verification (SV) survey depths (D04 and D10 respectively) as well as provide a catalog of the deepest observations available (DFULL). The DFULL fluxes therefore represent the most reliable flux measurements we have, and will be our "truth" set.

We plot in Figure 4.3 the distribution of reported errors (FLUXERR\_AUTO/DETMODEL from SExtractor) for the D04 and D10 catalogs (our "observation" sets) compared to the actual difference between the D04/10 and DFULL fluxes for the same objects in a small region in DES that overlaps the 2 deg<sup>2</sup> COSMOS<sup>3</sup> footprint. From this we can conclude

---

<sup>2</sup>[www.astromatic.net/software/sextorator](http://www.astromatic.net/software/sextorator); software used to measure the observed properties of every DES object.

<sup>3</sup>[cosmos.astro.caltech.edu](http://cosmos.astro.caltech.edu)

that the fluxes and errors reported for objects in the DES wide survey differ slightly from the assumed and expected Gaussian distribution.<sup>4</sup> But we should only concern ourselves with this deviation if it significantly impacts our final goal - calculating accurate Bayesian posterior probabilities of redshift group membership.

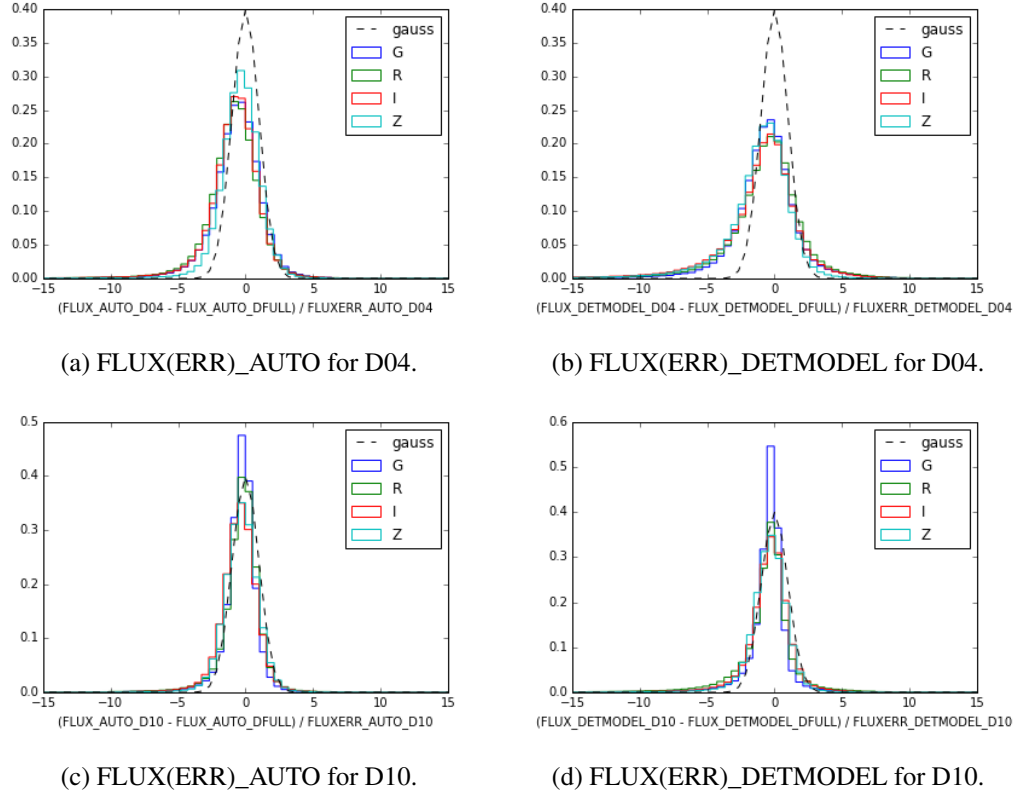


Figure 4.3: Histograms of D04/D10 flux deviation from DFULL in units of reported flux error. The dotted line is a  $1\sigma$  Gaussian distribution, i.e. what we expect if DFULL is the true flux, and the errors are reported exactly correctly.

We perform an experiment to this end using custom mock errors that do not obey the expected Gaussian noise distribution. By analyzing them assuming Gaussian errors, we can study the impact of non-Gaussianity on our posteriors.

---

<sup>4</sup>This difference is noticeably worse for DETMODEL fluxes, which is why we will use AUTO fluxes in the following analyses.

We start with an existing simulated catalog<sup>5</sup> that has redshift and FLUX\_NOISELESS values for each object. We separate this catalog into three redshift ranges:  $z = 0.001 - 1.0$ ,  $z = 1.0 - 3.0$ , and  $z = 3.0 - 9.9$ , and use them as our templates. The targets for this test are the same objects as the templates, but with noise added to their fluxes following our mock error function (new fluxes are labelled FLUX\_NOISELESS+NOISE). The error distribution for this mock catalog is shown in Figure 4.4. We choose an exaggerated form for this function inspired by the deviation in shape seen in Figure 4.3 for the DES D\* catalogs. We run two tests with this target/template set:

1. Calculate the posteriors assuming the traditional Gaussian form for  $P(\vec{f}_{obs}|\vec{f}_{template})$  (Equation 4.2).
2. Repeat the calculation using the exact error function applied in the mock catalog creation.

The results of these tests are shown in Figure 4.5. For a given slice in posterior probability, we expect the calculated  $P(z_{group})$  to equal the fraction of objects in the slice that have true redshifts in  $z_{group}$ . It is clear from Figure 4.5 that the choice of observed flux probability distribution has an effect on the shape and accuracy of the posteriors for every redshift range probed. We can use this test to check whether the actual DES deviation from normal seen in the D\* catalogs is large enough to affect the results we achieve in a similar, and statistically significant, way.

### 4.3.2 Probability Accuracy

Now we test the performance of the posteriors using the D10/DFULL catalogs instead of the mocks, i.e. whether the error distribution in Figure 4.3(c) is acceptably Gaussian. We match the objects in the DFULL catalog by position (within 1 arcsec) to objects from the COSMOS2015 catalog (Laigle et al. [2016]), which has 30-band photometric redshifts

---

<sup>5</sup>Created with BALROG for DES; more information on this catalog and its uses is in Section 5.5.

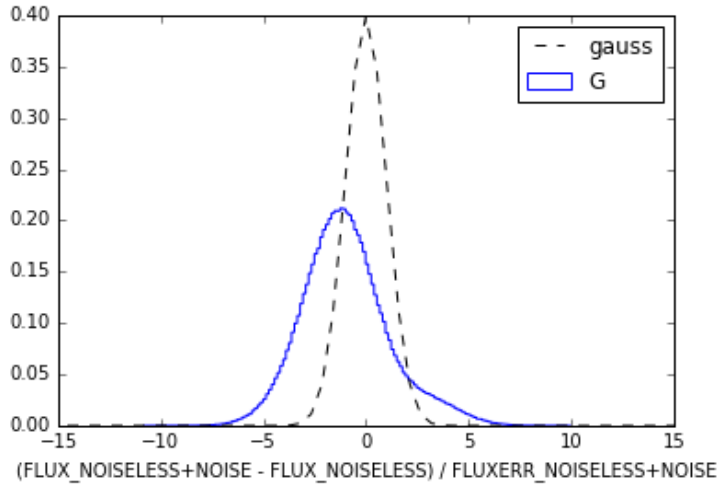


Figure 4.4: Custom error distribution (shown in blue) of the mock catalog used to test the assumptions made in the posterior probability calculation. It differs in shape from a  $1\sigma$  Gaussian distribution (shown in black) in a manner exaggerated from that found in the real data.

assigned to objects in the 2-deg<sup>2</sup> COSMOS field [Ilbert et al., 2009]. We tag these objects using the redshift column ZMINCHI2 (the redshift which minimizes the  $\chi^2$  of the LEPHARE (Arnouts et al. [2002]; Ilbert et al. [2006]) redshift probability distribution calculated for each object). We then match this template catalog with the D10 catalog (again within 1 arcsec), to create a matched target/template set as we did previously with the mock catalog. We calculate the posterior probabilities that the targets belong to a set of six redshift ranges. These results are shown in Figure 4.6. We expect an almost perfect reproduction of the true fraction of objects in each redshift range because the targets and templates are the same objects, observed with and without DES SV levels of noise. We find the method does this for most of the redshift and probability ranges, within uncertainties, and that it is unsurprisingly worse for high redshift ranges where the number of templates is lowest. We notice no significant deviation (from the 1-to-1 relation we expect) similar to that found with the test in Section 4.3.1 and conclude that the FLUX\_AUTO errors are acceptably Gaussian.

Another sanity check we can perform is to look at the colors of objects with high probability of belonging to a given redshift range. The colors of objects in the DFULL/COSMOS matched catalog are shown in Figure 4.7 and can be seen to follow the suggested evolution shown in part by the simulations in Figure 4.2. We compare the results of our method by plotting the same DES colors in Figures 4.8 and 4.9, but color the objects by their posterior probability of being in each of the six redshift ranges chosen. We can see that, overall, the evolution of probability with targeted redshift range follows the expectations from Figures 4.2 and 4.7.

## 4.4 Object Classification

In reality, the targets we seek to classify as high, low, or intermediate redshift types (for use as sources or lenses) will not be exact matches to the prior as in the previous sections' tests. We thus admit possible inaccuracy in the method due to an insufficient number of templates in some parts of the multi-dimensional flux space. This may lead to spuriously high likelihoods where a target's flux happens to be close to a lonely template in this space. We are dealing with sample sizes much smaller than those we would with shear (i.e. in the BFD method) since we are probing significantly higher redshifts where galaxies are rarer. We thus propose something novel: estimate the probability that we have wrongly classified each target. For example, if the target we have chosen as a  $z > 4$  LBG based on a high  $P(z > 4)$  is in fact a red galaxy at the lens redshift, the signal we measure will be boosted not by lensing but by the physical relationship between galaxies at the same redshift.

What we are doing is putting our targets into *classes*, which we will index by  $H$ , where the intention is that targets in this class predominantly exist in one of the redshift ranges we chose earlier. See Figure 4.10 for a demonstration of this task. In reality, each target *does* have a true redshift that is unknown to us that may or may not be in the range we classified it as being in. The unknown type of each galaxy will be indexed by  $G$ . For

a given patch of sky,  $i$ , the number of true type  $G$  galaxies we observe will depend on the average number density in the absence of lensing,  $n_{G,0,i}$ , the over- or under-density of  $G$  galaxies in that patch,  $\delta_{G,i}$ , and any magnification due to lensing,  $\mu_{G,i}$ , at the redshift where type  $G$  galaxies are found. We can thus write the number density of galaxies of a given true type  $G$  in this patch as follows:

$$n_{G,i} = n_{G,0,i}(1 + \delta_{G,i})[1 + k_{G,i}\Delta\mu_{G,i}] \quad (4.3)$$

where  $\Delta\mu_{G,i} = \mu_{G,i} - 1$  and

$$k_{G,i} = \frac{\partial \log n_{G,i}}{\partial \mu_{G,i}} \quad (4.4)$$

and describes how the observed number density of type  $G$  galaxies changes when lensed and depends in part on the luminosity function of type  $G$  galaxies as explained in Section 1.2.3.

Since we have classified the objects - giving them a new index,  $H$  - using the posterior probabilities we calculated using Equation 4.2, the observed number density of each class is directly related to the number density of the underlying truth types of targets in the class through the following equation:

$$n_H = \sum_G P(H|G)|_{\mu=1} n_G \quad (4.5)$$

where  $P(H|G)$  is the Bayesian posterior probability of having classified an object as  $H$  given that it is truly a type  $G$  galaxy.

This leads us to the final expression of measured number densities in patch  $i$  for a given class  $H$ ,

$$n_{H,i} = \sum_G n_{0,G,i}(1 + \delta_{G,i})[P(H|G)|_{\mu=1} + k_{HG,i}\Delta\mu_{G,i}] \quad (4.6)$$

where

$$k_{HG,i} = \frac{\partial \log n_{H,i}}{\partial \mu_{G,i}}. \quad (4.7)$$

## 4.5 Obtaining $P(H|G)$ and $k$

The probabilities  $P(H|G)$  are fairly straightforward to obtain if we have a matched truth/observation set as we used to test the method in Section 4.3.2. We can set  $P(H|G)$  to the fraction of objects with truth redshift in  $z_G$  that have observations classified as  $H$ .

But the derivatives with respect to lensing  $k_{HG}$ , a key piece of the above formulation, are not as easily calculated. We need to determine how each class density changes under magnification of the underlying types, which exist at different redshifts and thus incur varying magnitudes of the lensing convergence  $\kappa$ . We propose that these derivatives can be estimated using simulations. If one has a simulated catalog of objects with known redshifts, that are then observed through the same pipeline as that of the target survey, i.e. "observed" fluxes measured in the same system with the same noise as the targets, then one may follow this procedure:

For each type ( $G$ ):

1. Generate observations for the original set of input truth objects.
2. Count the number of objects in the observed set that belong to each class  $H$ .
3. Select objects in the truth set with redshifts matching type  $G$  galaxies.
4. Magnify these objects ( $\vec{f}_\mu = \mu \vec{f}$  and/or  $r_\mu = \mu^{1/2} r$ , where  $r$  is an estimate of size such as the half-light radius).
5. Generate observations for the new, magnified set of input truth objects.
6. Repeat 2. for the new set of observations and compare.

Unfortunately, while DES does have simulated catalogs that satisfy steps 1.-3., the magnified version requires a workaround that we describe in the next chapter.

## 4.6 Estimating Magnification $\mu(\theta)$

From Equation 4.6, we can extract the desired magnification  $\mu_{G,i}$ , for any galaxy type  $G$  (i.e.  $z > 4$  LBGs), if the probabilities  $P(H|G)$ , clustering  $\delta_{G,i}$ , and differentials  $k_{HG,i}$  are known for all class/type ( $H/G$ ) combinations. In practice,  $\delta_{G,i}$  will be unknown to us, so in order to properly constrain the problem we must assume something about the magnification and clustering of our galaxy types. Here we will assume that we have one galaxy type  $G_l$  that exists at the foreground lens redshift range ( $z_l \in z_{lens}$ ) that is not affected by magnification ( $\mu_l = 1$ ) but experiences an intrinsic clustering ( $\delta_l \neq 0$ ). We will assume the opposite for all other types  $G_s$  ( $s \in [s1..sN_s]$ ) where  $z_s > z_l$ , and  $N_s$  is however many "source" groups we choose to use. We can now estimate the clustering of type  $G_l$  galaxies and the magnification of type  $G_s$  galaxies ( $\delta_s = 0$ ) by solving the following set of equations:

$$\begin{pmatrix} n_{H_1} \\ n_{H_2} \\ \vdots \\ n_{H_N} \end{pmatrix} = \mathbf{P} \times \begin{pmatrix} n_{0,G_l} \\ n_{0,G_{s1}} \\ \vdots \\ n_{0,G_{sN_s}} \end{pmatrix} \quad (4.8)$$

where

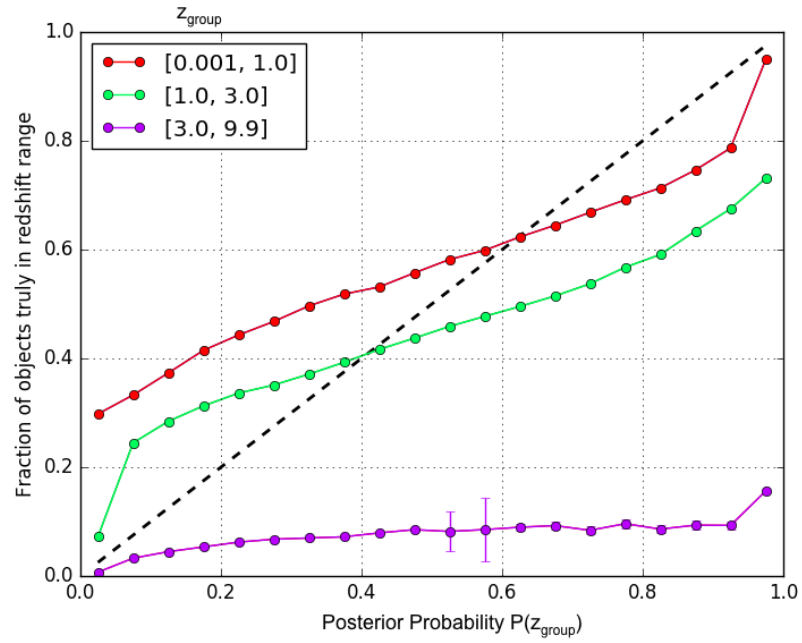
$$\mathbf{P} = \begin{pmatrix} P(H_1|G_l)(1 + \delta_{G_l}) & P(H_1|G_{s1}) + k_{H_1 G_{s1}} \Delta \mu_{G_{s1}} & \cdots & P(H_1|G_{sN_s}) + k_{H_1 G_{sN_s}} \Delta \mu_{G_{sN_s}} \\ P(H_2|G_l)(1 + \delta_{G_l}) & P(H_2|G_{s1}) + k_{H_2 G_{s1}} \Delta \mu_{G_{s1}} & \cdots & P(H_2|G_{sN_s}) + k_{H_2 G_{sN_s}} \Delta \mu_{G_{sN_s}} \\ \vdots & \vdots & \ddots & \vdots \\ P(H_N|G_l)(1 + \delta_{G_l}) & P(H_N|G_{s1}) + k_{H_N G_{s1}} \Delta \mu_{G_{s1}} & \cdots & P(H_N|G_{sN_s}) + k_{H_N G_{sN_s}} \Delta \mu_{G_{sN_s}} \end{pmatrix} \quad (4.9)$$

The final estimator for the observed magnification of a set of source type galaxies,  $\hat{\mu}_{G_s}$ , is the average of the  $\mu_{G_s}$  elements found from Equation 4.8 over all observed patches of sky. For a catalog of lenses, we can measure  $\mu_{G_s}$  in circular annuli at radius  $\vec{\theta}_i$  from each lens. This magnification will be related to the measured angular two-point correlation function between the lenses and each class (similarly to the approximation in Equation 1.22) by

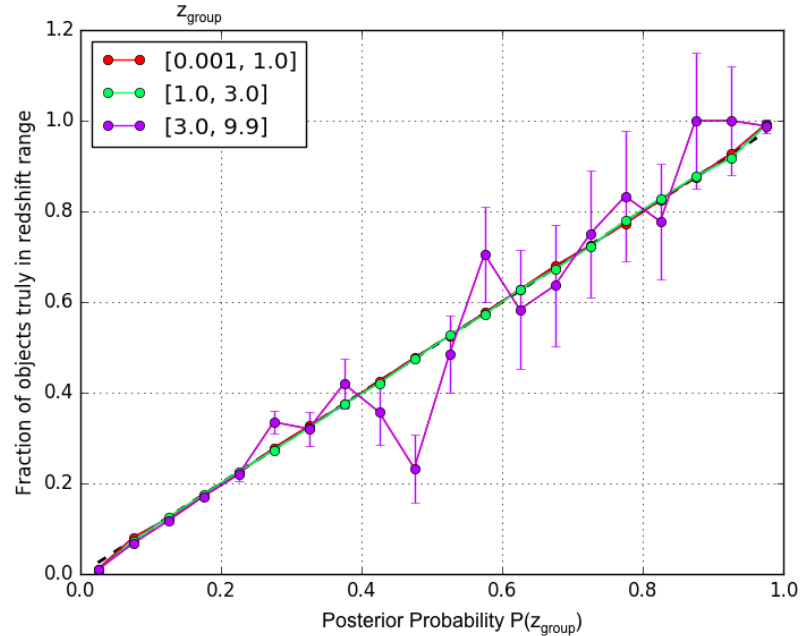
$$w_{IH}(\theta) = \frac{P(H|G_l)}{P(H_1|G_l)} \frac{n_{H_1}}{n_H} (1 + \delta_{G_l}) + \sum_{s=1}^{N_s} k_{HG_s} \Delta \mu_{G_s}(\theta). \quad (4.10)$$

## 4.7 Conclusion

The Bayesian source selection method described in this chapter has been shown to perform adequately using templates with DES fluxes and reliable photometric redshifts. The use of survey simulations and deep fields is a new approach to accounting for contamination by mis-classified objects and predicting the realistic effects on source number density due to magnification of galaxies at significantly different redshift ranges. This method should be applicable to any survey with such data products available. We present the application of this method on DES Science Verification data in the following chapter.



(a) Posterior probability accuracy when assuming Gaussian errors.



(b) Posterior probability accuracy when using the correct (input) error function from Figure 4.4.

Figure 4.5

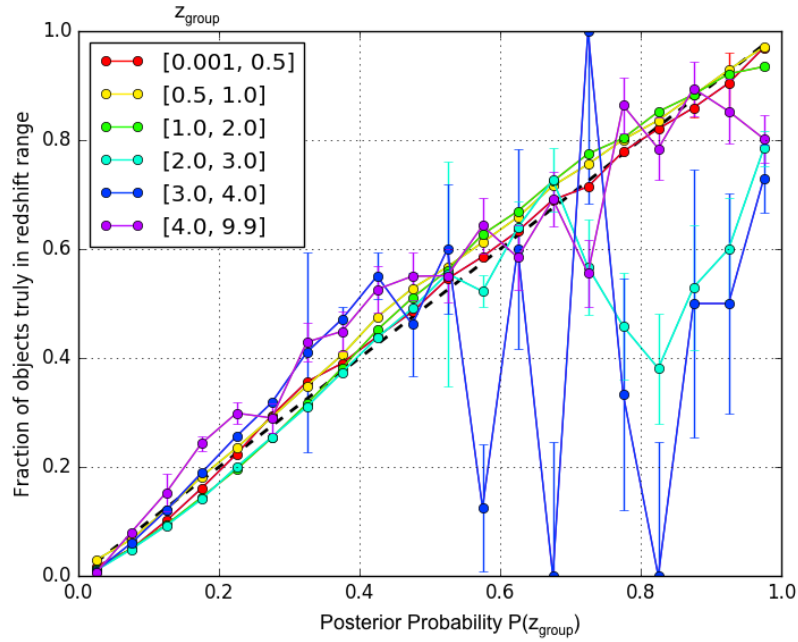


Figure 4.6: Posterior probability accuracy for objects in the DES D10 catalog when the prior consists of their counterparts in the matched DFULL/COSMOS catalog.

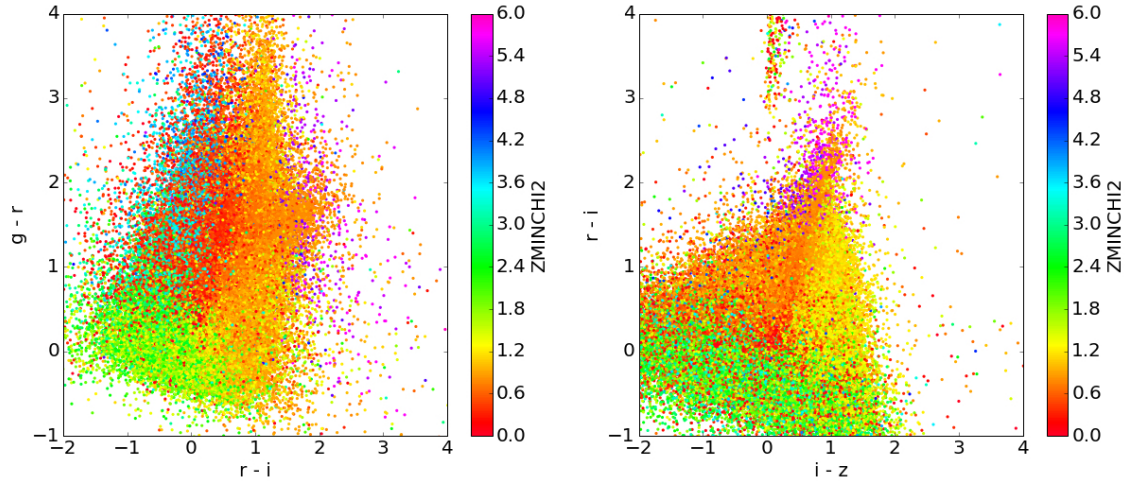


Figure 4.7: DES  $g - r$  vs.  $r - i$  (a) and  $r - i$  vs.  $i - z$  (b) for objects in our DFULL/COSMOS matched catalog, colored by their  $ZMINCHI2$  value.

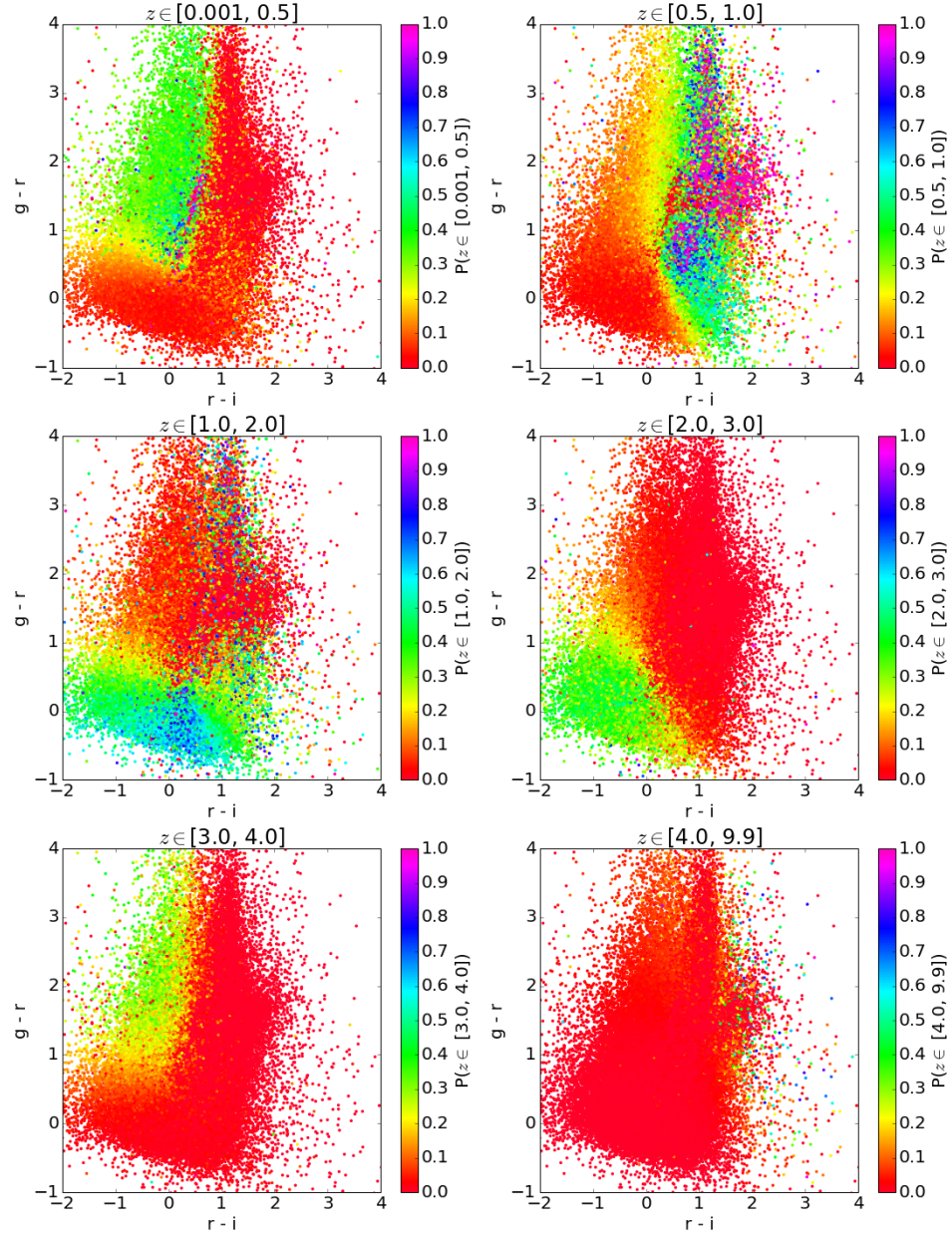


Figure 4.8: DES  $g - r$  vs.  $r - i$  for objects in the D10 catalog. Each panel's points are colored according to their posterior probability of membership in different redshift bins ( $P[z_{min}, z_{max}]$ ).

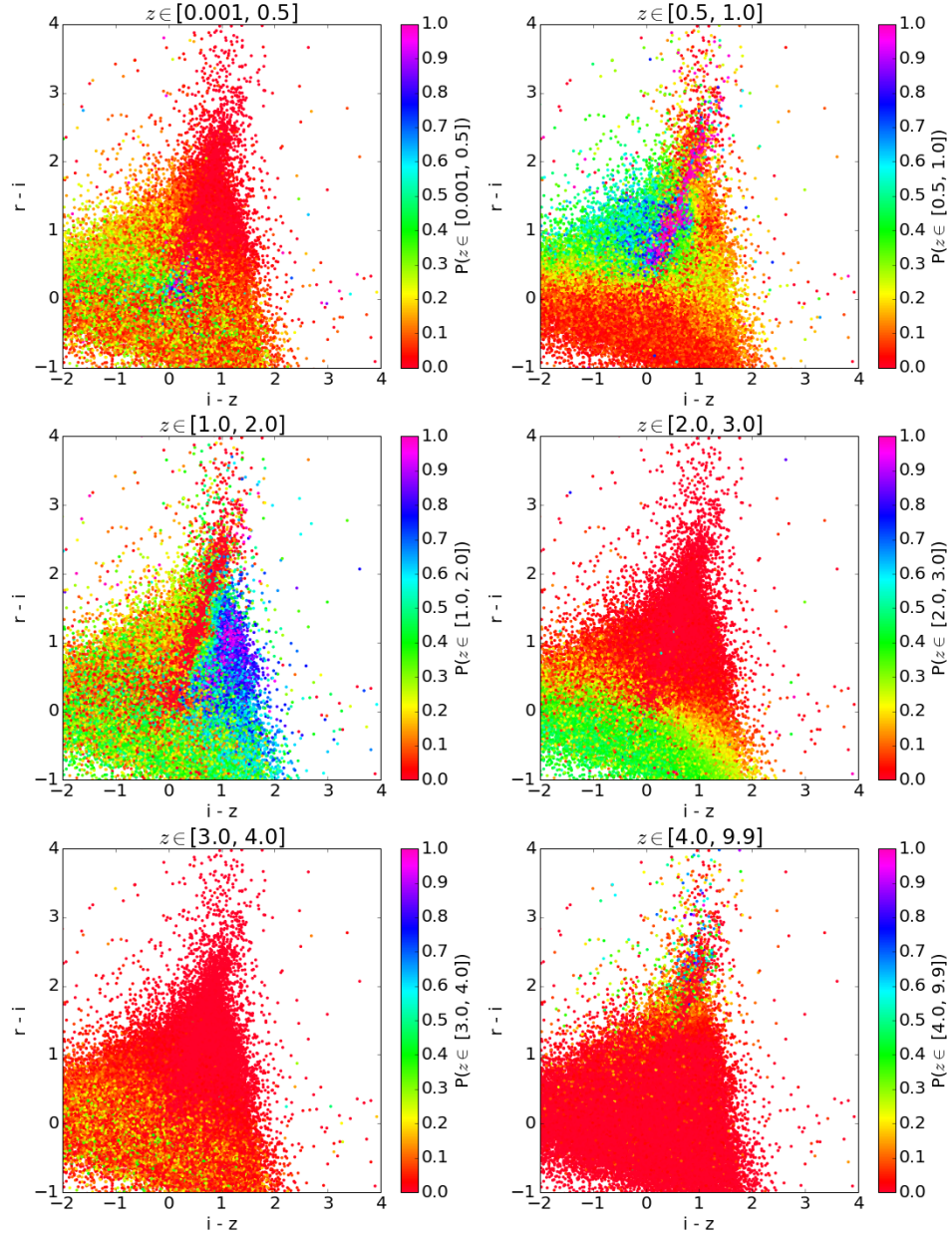


Figure 4.9: DES  $r - i$  vs.  $i - z$  for objects in the D10 catalog. Each panel's points are colored according to their posterior probability of membership in different redshift bins ( $P[z_{min}, z_{max}]$ ).

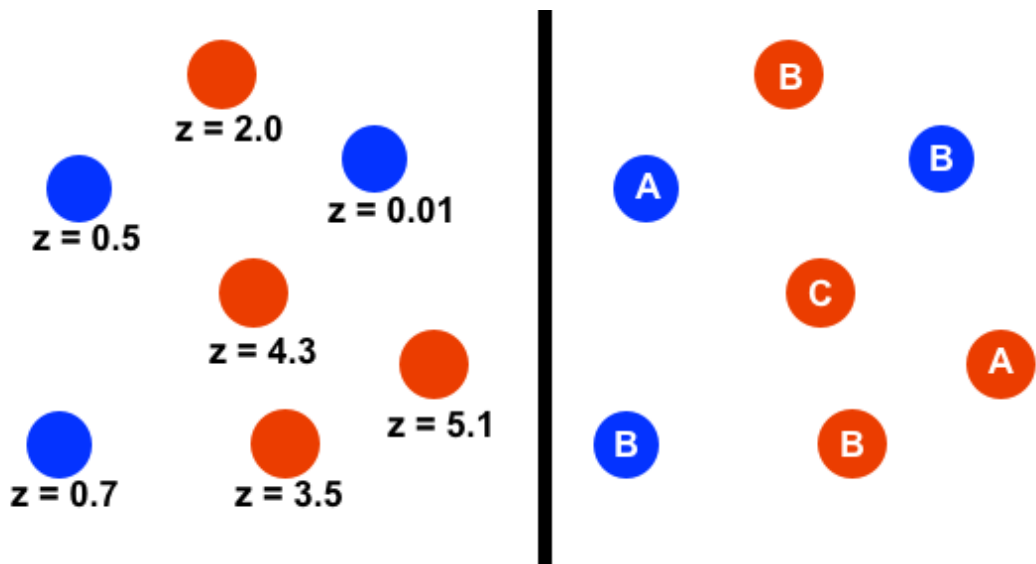


Figure 4.10: Left: Objects labeled by their true redshift (these are unknown to us). Right: The same objects classified into groups A, B, and C (low, medium, and high redshift classes) by some combination of their posterior probabilities. Not all objects will be classified into the correct group, i.e. a red object may be classified as group A despite being at very high  $z=5.1$ .

# Chapter 5

## Magnification of High Redshift Galaxies in the Dark Energy Survey

We will apply the method from Chapter 4 to the Dark Energy Survey’s (DES) Science Verification (SV) run. We choose this dataset over the subsequent Year 1 (Y1) and Year 3 (Y3) datasets because the SV data are deeper, and the necessary BALROG artificial-object tests are as yet only available for SV. This also gives us the benefit of using previous weak lensing (WL) analyses on this data to inform or verify our results.

### 5.1 Previous DES WL Results

Several papers have been published on weak lensing using SV galaxies. Clampitt et al. [2017] calculated the tangential shear around galaxies in the redshift range  $0.2 < z < 0.8$  from  $139 \text{ deg}^2$  of the SV region. The lenses come from the redMaGiC catalog, a sample of galaxies with low photometric redshift errors and few outliers [Rozo et al., 2016]. They are selected using a red-sequence-finding algorithm, resulting in  $z_{spec} - z_{photo} = 0.005$ , and  $\sigma_z/(1+z) = 0.017$ . This tight relation is shown in Figure 5.1. The tangential shear measurements from Clampitt et al. [2017] using three different redMaGiC lens bins is shown in Figure 5.2.

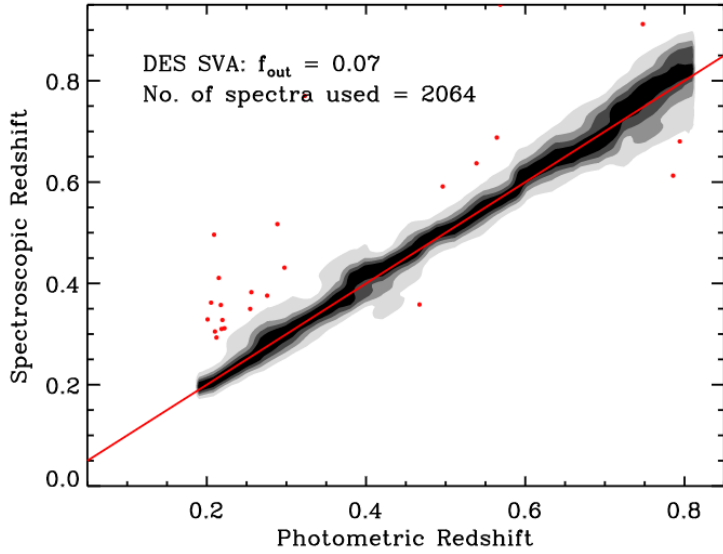


Figure 5.1: Spectroscopic vs. photometric redshifts for a subset of the redMaGiC catalog.  
Figure from Rozo et al. [2016].

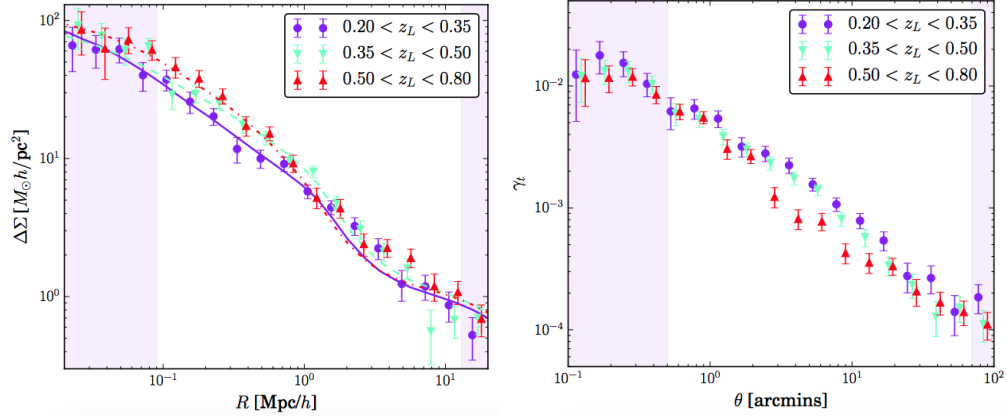


Figure 5.2: Figure from Clampitt et al. [2017]. Left: Differential surface mass density  $\Delta\Sigma$  measured from WL shear around redMaGiC lenses in three redshift bins (as labeled). Best-fit model curves are also shown for each sample. Right: The same, but showing the tangential shear  $\gamma_t$ .

A magnification analysis has also been published for DES SV by Garcia-Fernandez et al. [2018]. Instead of using the whole redMaGiC sample as their lens set, they select

redMaGiC galaxies with photometric redshifts  $0.2 < z < 0.4$  as lenses and those with  $0.7 < z < 1.0$  as sources. These results are shown in Figure 5.3. We will use the same

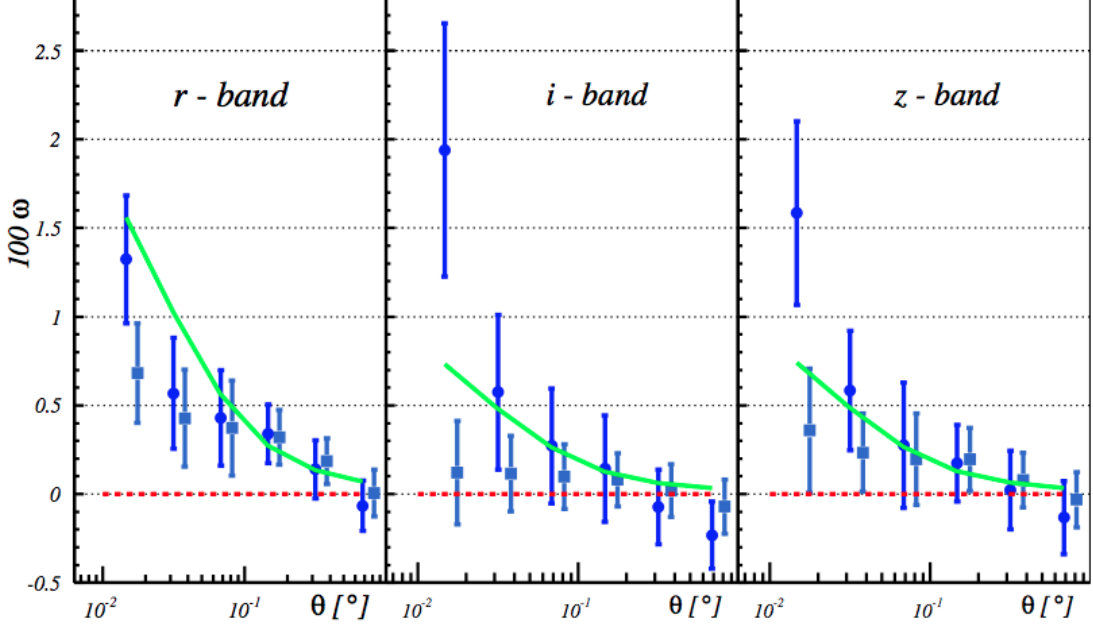


Figure 5.3: Figure from Garcia-Fernandez et al. [2018]. Measured two-point angular cross-correlation functions for the samples  $r < 23.0$ ,  $i < 22.5$  and  $z < 22.0$ , left to right respectively. Dots use the optimal weighting [Scranton et al., 2005], where each galaxy is weighted by its corresponding  $\alpha(m) - 1$  value, whereas squares are equally weighted. The green line is their theoretical prediction. The red dashed line is zero.

redMaGiC lenses from the above measurements in our analysis.

## 5.2 Targets: SVA1 Gold

DES has thus-far completed five years of observations and released datasets up to and including Year 3. In order to estimate magnification in the manner laid out in Chapter 4, however, several ancillary catalogs are required.

We use the matched D10/DFULL/COSMOS catalog to calculate the probabilities  $P(H|G)$  as described in Section 4.5. To calculate the differentials  $k_{HG}$  we need a cata-

log of truth objects and a catalog of the same objects after being observed through the DES pipeline. Thankfully we have such a set of catalogs produced by the software BALROG, which we will discuss in Section 5.5. Since the BALROG catalogs only exist for the Science Verification (SV) run of DES, we will use this dataset for our magnification analysis.

The SV run was completed in 2012, and its observations are presented in the SVA1 Gold Catalog.<sup>1</sup> This catalog is a set of objects from SV that have been calibrated and flagged for data quality. The catalog spans  $\sim 250$  deg<sup>2</sup> of sky, but our analysis will focus on the contiguous region known as SPT-E for its overlap with the South Pole Telescope (SPT)<sup>2</sup> coverage. A map of the  $\sim 15,000,000$  objects in this region is shown in Figure 5.4. The catalog has a non-uniform depth as it is a compilation of all available good exposures, and it also varies in data quality. The median  $10\sigma$  limiting magnitudes of galaxies for each band are  $g = 24.0$ ,  $r = 23.8$ ,  $i = 23.0$ , and  $z = 22.3$ . Additionally, the objects may be separated into stars and galaxies using a MODEST\_CLASS flag.

### 5.3 Templates

For our galaxy templates, we create a catalog by matching the DES DFULL catalog (see Section 4.3.1 for a more detailed description) to the COSMOS2015 30-band photo-z catalog (covering 2 deg<sup>2</sup>; Laigle et al. [2016]; Ilbert et al. [2009]) by position within 1 arcsec. For each target we compute the probabilities that it belongs to a set of redshift ranges using Equation 4.2, where the templates are sorted into redshift groups by their COSMOS2015 photo-z's. The number of templates in each redshift range is detailed in Table 5.1. A minimum photo-z of 0.001 is chosen to reject stars in the template set that have ZMINCHI2 set to zero, and a maximum value of 9.9 is allowed to reject other objects (i.e. X-ray sources and AGN) that are valued at 9.99.

---

<sup>1</sup><https://des.ncsa.illinois.edu/releases/sva1>

<sup>2</sup><https://pole.uchicago.edu>

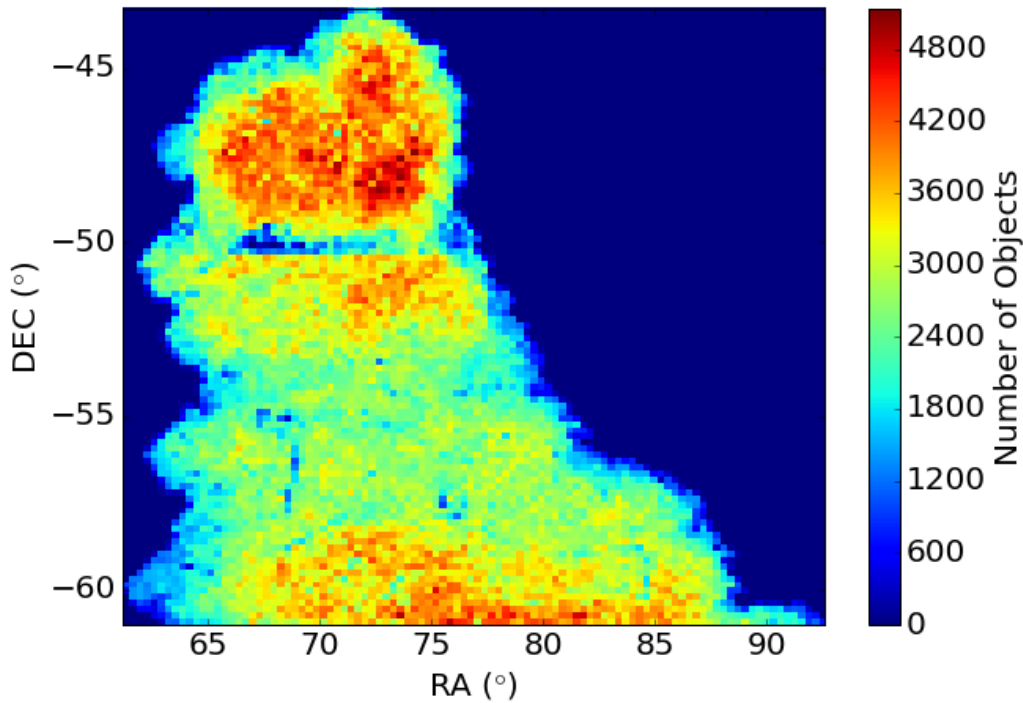


Figure 5.4: Density of objects in the SVA1 Gold Catalog.

$z_{group}$	$N_{templates}$
0.001-0.5	83,787
0.5-1.0	112,333
1.0-2.0	111,867
2.0-3.0	42,251
3.0-4.0	16,447
4.0-9.9	5,581

Table 5.1: The six groups of redshift ranges and number of templates for each group.

### 5.3.1 Stars

In addition to identifying redshift ranges of target galaxies, it is important to weed out stars from the target set. Instead of simply using the MODEST\_CLASS flag as described above, we can use additional templates with typical star fluxes to produce a posterior

probability that a target is actually a star. Templates should have low noise, so using stars already identified in DES is not ideal. Instead, we use GALAXIA [Sharma et al., 2011], a program that simulates Milky Way stars for a desired patch of sky. The output fluxes/magnitudes from GALAXIA are in the filter system of the Sloan Digital Sky Survey (SDSS)<sup>3</sup>. We transform these into DES *griz* system using transformations calculated for internal DES calibrations<sup>4</sup>. The final simulated star template catalog covers an area of 390 deg<sup>2</sup> centered on the SV footprint. Using these templates, we are able to calculate a  $P(STAR)$  in addition to the redshift range probabilities.

## 5.4 Target Classification

We assign SVA1 Gold targets to five redshift classes using cuts on the posterior probabilities calculated using Equation 4.2. These cuts and the total number of objects in each class are listed in Table 5.2. The DES colors for each class are shown in Figure 5.6. We note that the objects in this figure are only targets that meet one (or more) of the classification criteria.

Class	$z_{class}$	Probability Cut	$N_{class}$
A	0.001-1.0	$P(z_{class}) > 0.9$	3,478,140
B	1.0-2.0	$P(z_{class}) > 0.8$	238,569
C	2.0-3.0	$P(z_{class}) > 0.45$	89,817
D	3.0-4.0	$P(z_{class}) > 0.4$	10,657
E	4.0-9.9	$P(z_{class}) > 0.5$	36,176

Table 5.2

---

<sup>3</sup><https://www.sdss.org>

<sup>4</sup>D. Tucker, private communication

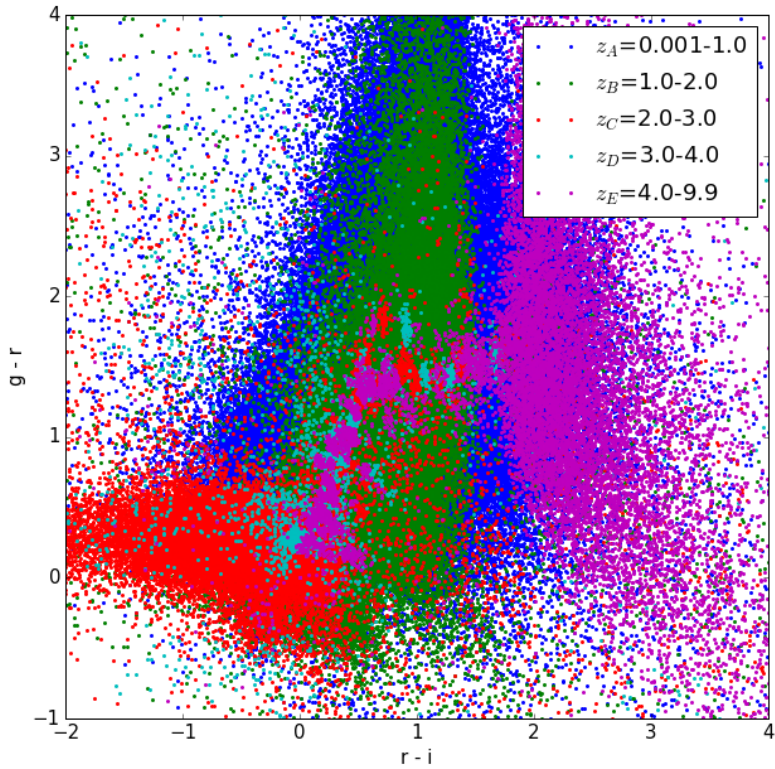


Figure 5.5: DES  $g - r$  vs.  $r - i$  for the SVA1 Gold targets that pass the probability cuts for each class as described in Table 5.2.

## 5.5 BALROG

In order to estimate the magnification of objects in each redshift range using our classified targets, we need to calculate  $k_{HG}$  - i.e. how our classifications are affected by magnification. For this, we use BALROG. BALROG [Suchyta et al., 2016] is a software suite that embeds fake objects in real survey images in order to characterize any measurement biases of the survey. By using BALROG with DES, we can thus naturally account for systematics from photometric pipeline, detector effects, seeing, etc. that are normally difficult to quantify. BALROG begins with simulated objects that are superpositions of arbitrarily many elliptical Sérsic profiles and adds Poisson noise to their flux. The simulated

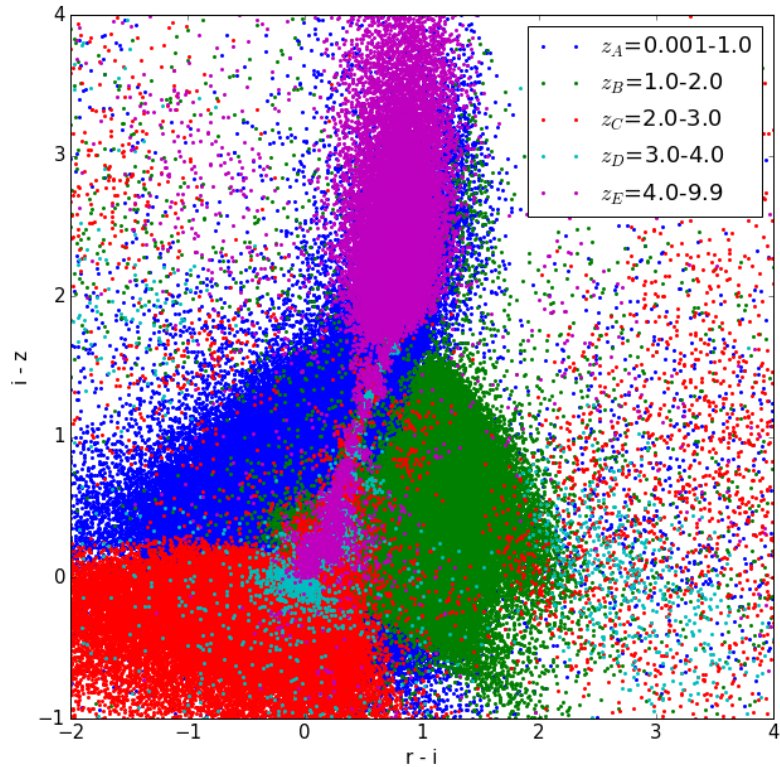


Figure 5.6: DES  $r - i$  vs.  $i - z$  for the SVA1 Gold targets labeled by their classifications as described in Table 5.2.

object magnitudes and sizes are drawn from the COSMOS Mock Catalog (CMC, Jouvel et al. [2009]), so there is some bias due to COSMOS being small field with limited statistics and cosmic variance. Morphologies are drawn from the Mandelbaum et al. [2006] catalog. For every coadded image in the survey, a subset of these profiles are convolved with the coadd point spread function and drawn onto the image.

The BALROG catalog is therefore an ideal set of random objects because the input positions have no intrinsic clustering. For the SV run of DES, BALROG was used to inject 40 million simulated objects into  $178 \text{ deg}^2$  of SV coadds. The catalog of input model fluxes and positions is called the "TRUTH" catalog. These inputs are meant to mimic the

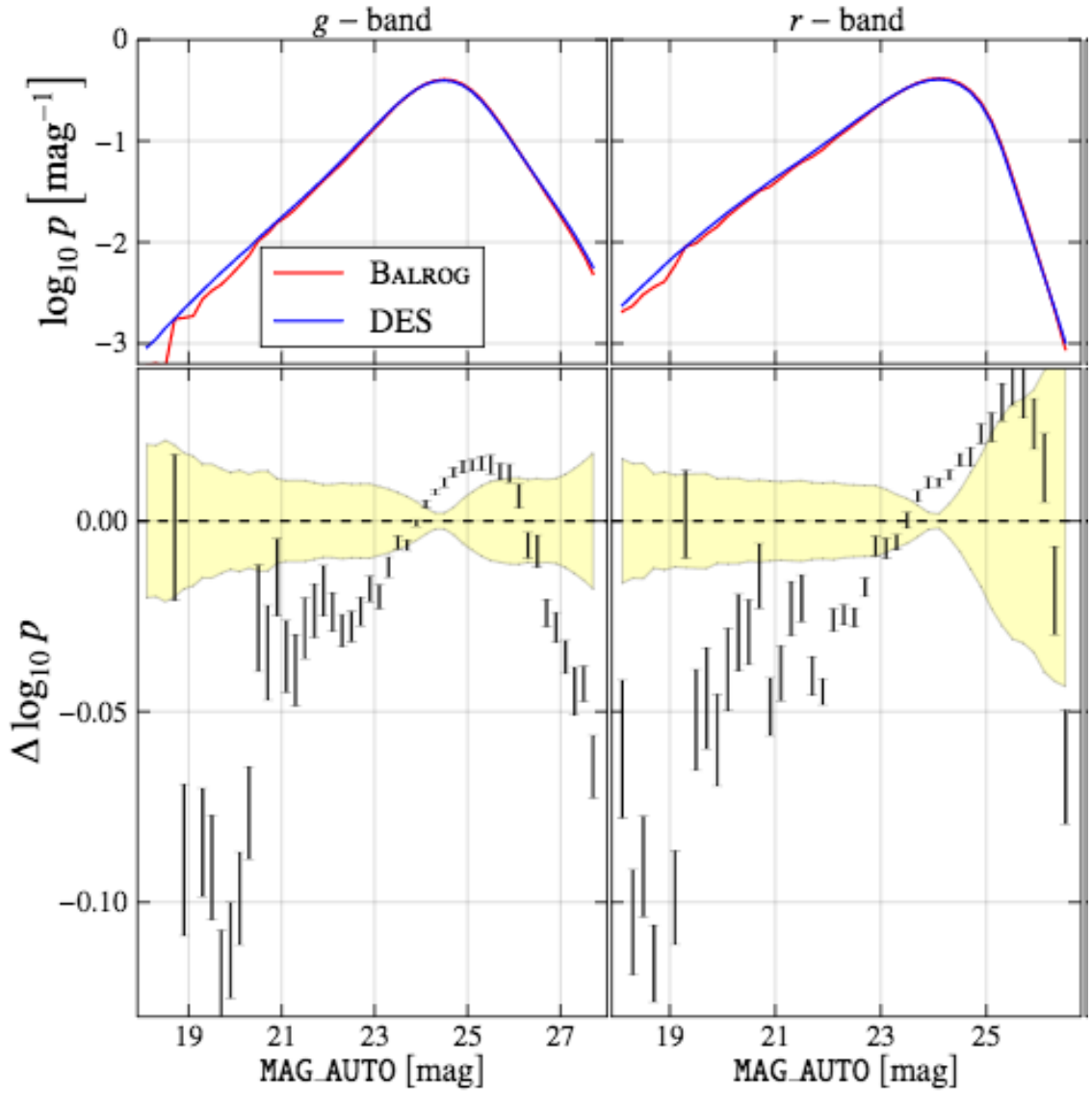


Figure 5.7: Figure from Suchyta et al. [2016]. The observed distributions of MAG\_AUTO *gr* magnitudes in the BALROG SIM catalog compared with those in DES SV.

real distribution of objects in DES; see Figure 5.7. They use the same source detection software, SExtractor, with the same settings used by DES, to then detect (or not) and measure the input objects on the whole image. The observed catalog thus inherits the inhomogeneities of the real data. This new catalog of SExtractor properties is called the

"SIM" catalog, and does not necessarily have a 1-to-1 correspondence with the TRUTH catalog because input objects may or may not have been detected by SExtractor. Objects in both catalogs can be matched by their BALROG ID. We can therefore use the TRUTH and SIM catalogs to calculate the  $k$ 's following a modified version of the procedure laid out in Section 4.5.

A modification is necessary because there are no magnified versions of the BALROG catalogs, and running BALROG is non-trivial, so we must make due with the one set of TRUTH and SIM catalogs we have. To calculate the  $k$ 's, we want to artificially magnify our TRUTH catalog by multiplying the fluxes and sizes by the proper factors, and see how many objects show up in the SIM catalog before and after this process. But we desire to only magnify the objects in a given redshift group, because we want  $k_{HG}$  for every  $H/G$  pair. Because BALROG was not meant to perfectly mimic the fluxes and colors of rare *high-redshift* objects, we choose which objects to magnify by matching the BALROG TRUTH catalog to the DFULL/COSMOS catalog (by closest flux and size) and select the TRUTH matches with COSMOS photo-z in the desired redshift range. Then, we count the matching SIM objects that are detected in each class  $H$ <sup>5</sup> before and after the magnification process for each type  $G$  in the TRUTH catalog.

## 5.6 Results

Using the above procedure we obtain the  $k$  values listed in Table 5.3. We also list the  $P(H|G)$  values from the D10/DFULL/COSMOS region in Table 5.4. Using Equation 4.8, we calculate the magnification  $\mu_G$  for six logarithmic angular bins around the  $\sim 95,000$  redMaGiC galaxies in the SPT-E region for each source galaxy type. These results are shown in Figure 5.9. We also calculate the correlation between lenses and sources from each of the five target classes for the same six angular bins, shown in Figure 5.8, using

---

<sup>5</sup>The BALROG SIM catalog is classified using the same templates and procedure as the SVA1 Gold targets.

	$k_{HG}$				
	$z_G = 0.001\text{-}1.0$	$z_G = 1.0\text{-}2.0$	$z_G = 2.0\text{-}3.0$	$z_G = 3.0\text{-}4.0$	$z_G = 4.0\text{-}9.9$
Class A	0.0352	0.0115	0.0154	0.00702	-0.00203
Class B	0.0484	0.00732	0.00244	0.00244	0.00244
Class C	0.0202	-0.147	-0.0204	0.00	-0.0102
Class D	0.161	-0.363	0.00	0.00	0.161
Class E	-1.01	-0.128	0.0612	0.00	0.00

Table 5.3:  $k_{HG} = \frac{d \log n_H}{d \mu_G}$  calculated by counting the change in the number of SIM objects in each class  $H$  when input BALROG objects with matched COSMOS photo-z in  $z_G$  are artificially magnified.

	$P(H G)$				
	$z_G = 0.001\text{-}1.0$	$z_G = 1.0\text{-}2.0$	$z_G = 2.0\text{-}3.0$	$z_G = 3.0\text{-}4.0$	$z_G = 4.0\text{-}9.9$
Class A	31.8%	0.854%	0.870%	1.81%	7.19%
Class B	0.551%	10.8%	0.666%	0.177%	0.879%
Class C	0.430%	2.27%	9.82%	1.76%	0.440%
Class D	0.0418%	0.0120%	0.0152%	1.01%	0.440%
Class E	0.0768%	0.0272%	0.00913%	0.00%	9.98%

Table 5.4:  $P(H|G)$  measured from the D10/DFULL/COSMOS matched field for each  $H/G$  pair.

the following estimation:

$$w_{IH}(\theta) = \frac{DD_H(\theta)}{DR_H(\theta)} \frac{N_{R,H}}{N_{D,H}} - 1, \quad (5.1)$$

where  $DD_H$  is the number of lens-target pairs for Class H and  $DR_H$  is the number of lens-BALROG pairs for the same Class. We note that both measurements are fairly noisy, and the errors on  $\mu_G$  are correlated between the  $G$  types.

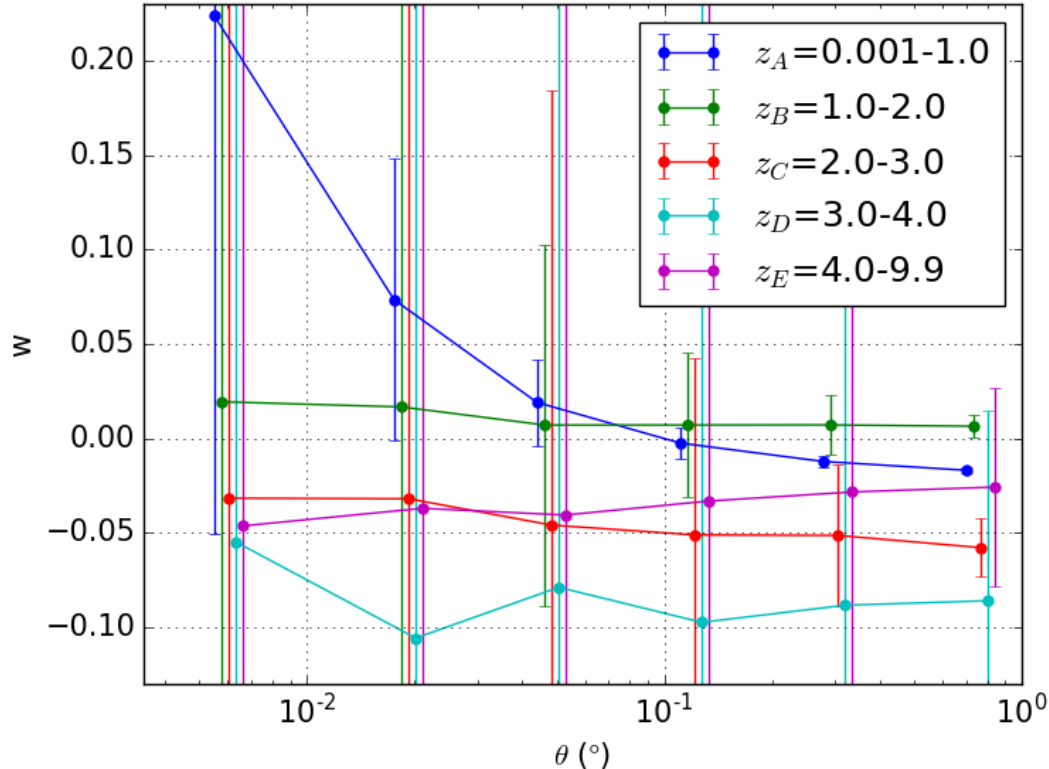


Figure 5.8: Angular two-point correlation functions for the five target classes and red-MaGiC lenses.

## 5.7 Discussion

For Classes B, C, D, and E, the flat nature of the measured correlations in Figure 5.8 and their position below zero is concerning and suggests a possible normalization error

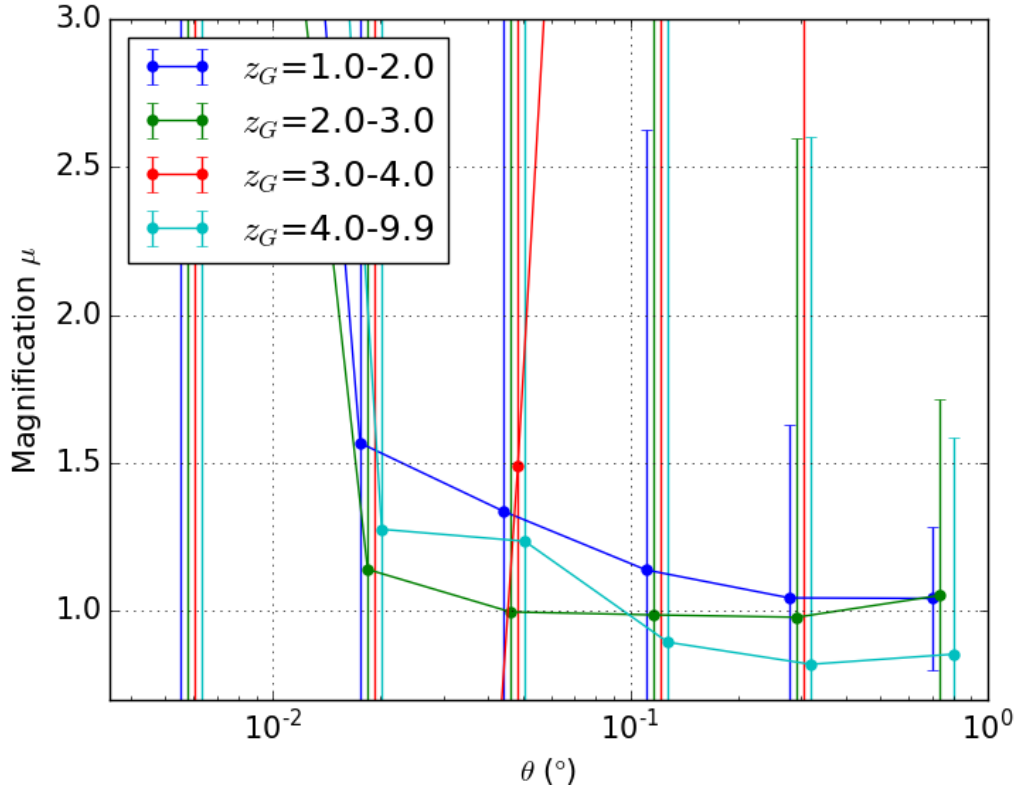


Figure 5.9: Estimated magnification for each of the source galaxy types.

between the targets and BALROG randoms that is not immediately obvious in our calculation. Class A ( $z_{class} = 0.001\text{-}1.0$ ), however, shows a large correlation at small  $\theta$ , which is expected since they have been chosen to be in the same redshift range as the lenses. The magnification in Figure 5.9 also shows unusual deviations from  $\mu_G = 1$  for the high redshift types. The source of these offsets is not known at this time. Considering some of the values of  $k_{HG}$  (Table 5.3) are identically zero, we have some concern about the process by which we obtain them. The procedure we use to select which matches in the BALROG TRUTH catalog to magnify does not seem to select enough objects for the higher redshift bins to generate changes in  $\log n_H$ . The application of this method on current and future DES datasets with larger sample sizes and improved BALROG software would be beneficial to understanding our result.

In addition to the magnification analysis we have presented, we also have a catalog of objects with Bayesian posteriors of redshift range membership. This catalog of probabilities and our classifications of SVA1 Gold objects may be useful for other astrophysical or cosmological analyses, since high redshift objects are particularly difficult to select and confirm.

# **Chapter 6**

## **Astronomers' and Physicists' Attitudes Towards Education & Public Outreach: A Case Study with The Dark Energy Survey**

The text and figures in this chapter are quoted from the article of the same name by A. Farahi, R. R. Gupta, C. Krawiec, A. A. Plazas, and R. C. Wolf. It is currently available in pre-print form on the arXiv [Farahi et al., 2018] and is in the review process for a science communication journal.

### **6.1 Introduction**

Over the past twenty years, the need for improved communication between scientists and the general public has been recognized worldwide [Kenney et al., 2016, Burns et al., 2003, National Research Council, 2010]. Advances in science and technology have transformed life in the 21st century, and institutions ranging from government agencies to business conglomerates are calling for change in the perception and understanding of sci-

ence. Such a paradigm shift has been discussed in the context of the science, technology, engineering, and mathematics (STEM) disciplines, eliciting reform in education materials spanning from the classroom to informal education spaces. This demand for STEM professionals to participate in education and public outreach (EPO)<sup>1</sup> has made evident, however, that the public does not know much about the scientific process or academic culture, nor do the scientists know much about the public interest [Miller, 1998, Lévy-Leblond, 1992]. Therefore, scientific societies such the American Association for the Advancement of Science are advocating a new model in which scientists engage with the public in meaningful dialogue that positively impacts the attitudes and behaviors of not only the general public, but of the scientists themselves.<sup>2</sup>

Of the many STEM topics available to captivate an audience, astronomy is one of the most popularly used to spur public interest [Heck and Madsen, 2013]. The night sky is accessible across the globe and provides a spark for curiosity. Astronomical images can be both scientifically discussed and aesthetically admired. Questions surrounding the origin and fate of the Universe inspire scientific, moral, and philosophical debate. Given the natural curiosity inspired by the subject, it is no surprise that there is overwhelming evidence that the public is interested in astronomy programming. Each year nearly 28 million people visit planetaria [National Research Council, 2001], and hundreds of thousands make their way to astronomical observatories. On social media, the NASA Twitter account<sup>3</sup> has nearly 30 million followers to date.

It would seem that such a public demand for astronomy material would encourage the larger community of astronomy professionals (including self-identified physicists, astrophysicists, astronomers, telescope engineers, and technical support staff) to engage in

---

<sup>1</sup>We define EPO in this context as any type of engagement between a STEM professional and a member of the public, including, but certainly not limited to: K-12 curriculum development and classroom visits, science festivals, written communication, social media, public lectures, radio and TV appearances, and museum programming. See Figure 6.2 for a list of EPO activities used in the survey instrument.

<sup>2</sup>[https://mcmprodaaas.s3.amazonaws.com/s3fs-public/content\\_files/2016-09-15\\_AAAS-Logic-Model-for-Public-Engagement\\_Final.pdf](https://mcmprodaaas.s3.amazonaws.com/s3fs-public/content_files/2016-09-15_AAAS-Logic-Model-for-Public-Engagement_Final.pdf)

<sup>3</sup><https://twitter.com/NASA>

EPO. However, as in many other STEM disciplines, there remains a disconnect between the duties of the professional and engagement in EPO. This is particularly evident in the perceived “Sagan Effect,” a stigma imposed by colleagues in academia on those research professionals who are actively involved in EPO [Shermer, 2002]. In a survey of 59 physicists, Johnson et al. [2014] observe that EPO is considered to be outside the realm of professional tasks and that those who participate in EPO activities are “perceived as occupying a marginal status.”

How and why professional physicists and astronomers engage in EPO has recently become a topic of research. In one of the first systematic surveys of a large international group of astronomers,<sup>4</sup> Dang and Russo [2015] observed that 79% of respondents ( $n = 155$ ; where here and hereafter  $n$  denotes the total number of responses) expressed belief that EPO initiatives are essential. In addition, only 43% of a subsample of respondents<sup>5</sup> ( $n = 116$ ) were explicitly funded to engage in EPO programming. Dang and Russo [2015] also asked about barriers to EPO engagement, finding that lack of time and grant funding were significant deterrents. Such barriers were confirmed by survey responses and interviews by Johnson et al. [2014] and Thorley [2016]. However, as Johnson et al. [2014] assert, better “understanding how scientists *interpret* outreach” is crucial for both research and policy. Furthermore, understanding these scientists’ perspectives of EPO will be essential for professionals developing future astronomy-related EPO programs.

In this article we present an analysis of scientists’ EPO experience as compiled from 131 survey responses from physicists, astronomers, and astrophysicists who are part of the Dark Energy Survey [DES, Dark Energy Survey Collaboration et al., 2016].<sup>6</sup> DES is an international collaboration of hundreds of scientists primarily working together to study the effects of dark energy. The project, which was conceptualized in 2004 and officially began taking data in 2012, is composed mainly of faculty, staff scientists, postdoctoral researchers (post-docs), and graduate students. The collaboration is structured into several

---

<sup>4</sup>This survey was conducted at the 2012 International Astronomical Union General Assembly.

<sup>5</sup>Several respondents elected not to answer survey items concerning funding.

<sup>6</sup><https://www.darkenergysurvey.org/>

working groups, each with a particular scientific focus. Since its inception in 2014, the Education and Public Outreach Committee has acted as a working group, developing and cultivating a diverse repertoire of online and in-person EPO initiatives. For more on DES science, infrastructure, and the EPO program, see Wolf et al. [2018].

We present an analysis of DES members’ attitudes towards, motivations for, and deterrents from STEM EPO programming. We consider both general EPO engagement and involvement specific to the DES EPO program. Throughout this article, we refer to the collective group of DES members as “scientists,” and emphasize that the attitudes expressed do not reflect the opinions of all people who self identify as professional scientists and/or researchers.

## 6.2 Methods

### 6.2.1 Survey Structure

Although DES scientists are experts in physics and astronomy, we aimed to investigate their opinions not only about EPO related to these particular disciplines, but about STEM education and outreach in general.

As such, we designed an anonymous online survey using the Google Forms<sup>7</sup> platform which could be electronically disseminated to collaboration members. The survey was composed of three sections: 1) an introduction, 2) questions about general STEM EPO engagement, and 3) questions about EPO attitudes specific to the structure of and resources available to DES and other large science collaborations. A final section collecting demographic information (i.e., gender, ethnicity, age, and position) concluded the survey. While all questions in the demographic section of the survey were mandatory, each question provided respondents with the option to decline a response. The survey was open to participants for two weeks; reminder emails were sent with one week, three days, and one day remaining in the open survey period.

---

<sup>7</sup><https://www.google.com/forms/about/>

We investigated scientists' dispositions from multiple perspectives by including survey items related to diverse components of the EPO experience. Respondents were asked about the types of activities in which they have engaged and how frequently that engagement takes place. We inquired about personal and professional motives for engagement, as well as any barriers. Furthermore, we asked scientists to describe how their peers view EPO and to provide their feedback on more centralized EPO organizational efforts. The complete survey and data are provided on the DES EPO research website.<sup>8</sup>

In the survey introduction, we defined STEM EPO under the umbrella of the Burns et al. [2003] "vowel analogy" of science communication: "the use of appropriate skills, media, activities, and dialogue" to produce "awareness, enjoyment, interest, opinions, and understanding" of science. The survey consisted of mixed question types including Likert<sup>9</sup> measures, multiple choice and checkbox questions, and free response. We note that due to nuances with the survey platform, in some cases respondents could not change an incorrectly submitted response.

### 6.2.2 Respondents

All DES members are encouraged to subscribe to a DES-wide LISTSERV (electronic mailing list), which is frequently used for collaboration-wide announcements and updates. The survey described in Section 6.2.1 was emailed to the DES LISTSERV, which at the time of this study, included 606 subscribers. Subscribers include current active DES members, as well those who are either inactive or have since left the field.

In total, 131 current and former DES members (22% of the LISTSERV membership) participated in the online survey, of which 115 self-identified as "Active Members." Figure 6.1 displays distributions of respondent gender, age, ethnicity, and position (e.g., fac-

---

<sup>8</sup><https://www.darkenergysurvey.org/education/des-education-outreach-science-communication-research/>

<sup>9</sup>Scaling method used to gauge response to a statement, i.e., the extent to which a respondent agrees or disagrees.

ulty or graduate student). Respondents were predominantly male and white. Most were relatively early career scientists: 65% reported they were under the age of 40 and 37% were younger than 30. Respondents were more evenly distributed with respect to current position. Post-docs, graduate students, and faculty each composed roughly a quarter of those surveyed. The remaining quarter consisted of staff scientists and people with other occupations (such as science educator, scientist emeritus, and software developer).

The DES membership database records are not current or detailed enough to allow us to make demographic comparisons of the respondents to the full DES collaboration. It is, however, possible to compare to recent data drawn from the larger astronomy community, such as the American Astronomical Society (AAS) Workforce Survey of 2016 US Members.<sup>10</sup> The AAS survey results consist of responses from 1795 AAS members living in the United States. Of the AAS respondents, 73% identified as male compared to 72% in our survey. One percent of AAS respondents and 3% of DES respondents preferred not to indicate their gender. The distribution of ethnicities for AAS respondents was 84% white, 9% Asian, 3.5% Hispanic or Latino, and 1% black or African American. The corresponding fractions for our DES respondents were 72%, 10%, 5% and 1.5%. Four percent of AAS respondents and 11% of DES respondents preferred not to indicate their ethnicity. Given this comparison, we conclude that our survey sample is fairly representative of the astronomy community in the United States, at least in terms of gender and ethnicity.

For cases in which we had both hypotheses about response differences between demographic groups and sufficient sample size, we performed chi-squared tests of independence to quantify any significant effects. Respondents were grouped as follows: gender [male, female], ethnicity [white, non-white], age [18-30, 31-40, 41+], and academic position [tenured (i.e., Staff Scientist, Faculty/Professor, or Scientist Emeritus), non-tenured (i.e., Undergraduate Student, Graduate Student, or Post-Doc)]. The results of these tests are presented in Sections 6.3.1 and 6.3.2.

Since participation in the survey was entirely voluntary, we could not ensure that all

---

<sup>10</sup>[https://aas.org/files/aas\\\_members\\\_workforce\\\_survey\\\_2017.pdf](https://aas.org/files/aas\_members\_workforce\_survey\_2017.pdf)



Figure 6.1: Demographic information for study respondents. Here we display breakdowns by (a) gender, (b) age, (c) ethnicity, and (d) current position as self-reported in the survey.

DES members responded or that those who did were a representative sample of the full DES collaboration. Therefore, selection bias is a factor that impacts the results presented here. It is likely that many of the study respondents were members who already had some interest in EPO. Roughly 79% of respondents stated that they were (or have been) involved in some type of EPO project local to their institution or community, and 66% responded that they had participated in a DES-specific EPO initiative.

## 6.3 Results

### 6.3.1 Types of Engagement and Time Commitment to EPO

In the first main section of the survey, we provided a list of nineteen EPO activities (see Figure 6.2), spanning a range of engagement audiences, environments, and media, and asked scientists to indicate how frequently (if at all) they had engaged in each. The five most popular responses<sup>11</sup> were: PUBLIC PRESENTATIONS/LECTURES (82%), UNDERGRADUATE TEACHING (79%), SCIENCE FAIRS/FESTIVALS (67%), MENTORING (64%), and SOCIAL MEDIA (PERSONAL, I.E., FROM A PERSONAL TWITTER ACCOUNT) (54%). We find these most common answers unsurprising, as participation in these activities is accessible to, and commonly asked of, scientists at many academic institutions.

However, participation in specific EPO activities may not be indicative of the importance scientists place upon them. One could posit that pragmatic and logistical factors such as ease, cost, and required time likely influence how scientists elect to engage in EPO. Furthermore, it is possible that these factors are more influential than the perceived value of the activities themselves. To explore this hypothesis, we asked survey respondents to rank the nineteen EPO activities on a 5-point Likert scale: 1 = LEAST IMPACTFUL/VALUABLE TO THE AUDIENCE to 5 = MOST IMPACTFUL/VALUABLE TO THE AUDIENCE. They were also given the option to choose NOT IMPACTFUL/SHOULD NOT COUNT AS EPO or I DON'T KNOW. To determine which activities respondents deemed the most impactful (highest value), responses were scored using the following metric for each activity:

$$Value = \frac{R}{5n}, \text{ where } R = \sum_{i=1}^n R_i \text{ and } n = n_{\text{resp}} - n_{\text{IDK}}. \quad (6.1)$$

Here  $R_i$  is the rank from 0-5 (NOT IMPACTFUL responses were counted as 0),  $n_{\text{resp}}$  is the total number of responses, and  $n_{\text{IDK}}$  is the number of "I Don't Know" responses (which are excluded from the sum). Using Eq. 6.1, we find the top five activities with

---

<sup>11</sup>Choosing a response indicates that the respondent had participated in this activity at least once.

the highest value are: ON-AIR MEDIA (E.G., TV, RADIO), *Value* = 0.86, *n* = 125; ELEMENTARY/HIGH SCHOOL TEACHER DEVELOPMENT, *Value* = 0.85, *n* = 128; MENTORING, *Value* = 0.81, *n* = 124; SCIENCE JOURNALISM/SCIENCE WRITING/SCIENCE BLOGGING, *Value* = 0.80, *n* = 127; PUBLIC PRESENTATIONS/LECTURES, *Value* = 0.80, *n* = 128. Figure 6.2 directly compares reported participation and perceived value for all 19 activities. Among the largest disparities found in this comparison include ELEMENTARY/HIGH SCHOOL TEACHER DEVELOPMENT, SCIENCE JOURNALISM/SCIENCE WRITING/SCIENCE BLOGGING, and ON-AIR MEDIA (E.G., TV, RADIO), which are ranked high in value, but are not as commonly engaged in as the other highly-valued activities. Among the activities with the least participation are AUDIO MEDIA (E.G. MUSIC, PODCASTS) and COMEDY/PLAYS/OPEN MIC NIGHTS which are also among the lowest-valued.

We also included several questions designed to learn how much time DES scientists commit to EPO. We asked survey respondents to indicate their average weekly time commitment to preparing and engaging in EPO activities by checking corresponding boxes. In addition, we asked how much time they *would like to* spend on such tasks. A summary of these responses is shown in Table 6.1. It is clear that, on the whole, respondents would like to spend more time on both preparing and engaging in EPO than they currently are. Thirty-five percent of respondents would like more time to prepare for EPO activities, while 62% are satisfied with their current preparation time. Similarly, 45% of respondents would like to spend more time actually engaging in EPO, while 54% are content with current engagement. Furthermore, while nearly 10% of respondents do not engage in EPO, only 3% lack the interest.

We also asked respondents to choose answers corresponding to *when* they primarily engage in EPO. The majority chose the response I ENGAGE IN EPO DURING WORK HOURS AND DURING MY FREE TIME (63%). The remaining responses were as follows: I ONLY ENGAGE IN EPO DURING MY FREE TIME (I.E., DURING EVENINGS AND ON WEEKENDS (21%), I DO NOT ENGAGE IN EPO (8%), and I ONLY ENGAGE IN EPO

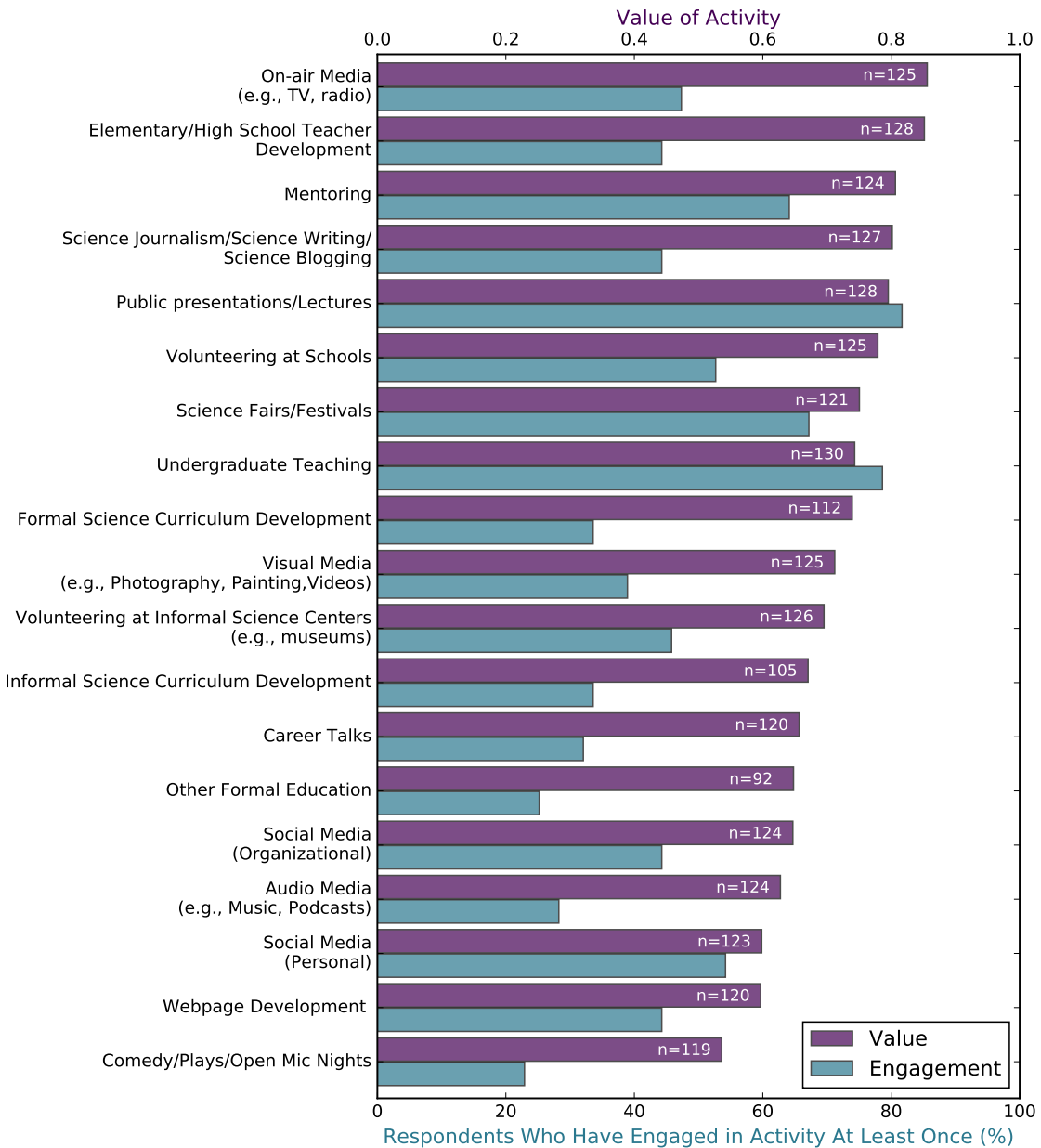


Figure 6.2: Respondents were presented with 19 activities and asked 1) if they have ever engaged in the activity and 2) to rank its value (level of impact). “Value of Activity” is calculated from Eq. 6.1. The number of counted responses,  $n$ , is noted in white (out of a total 131 respondents).

**(a) How long do you spend (on average) per week on EPO?**

Time Spent	On Preparation	On Engagement
I don't participate in EPO	13 (10%)	13 (10%)
0-1 Hrs	77 (59%)	69 (53%)
1-3 Hrs	30 (23%)	33 (25%)
3-5 Hrs	7 (5%)	9 (7%)
5-10 Hrs	3 (2%)	5 (4%)
>10 Hrs	1 (1%)	2 (2%)

**(b) How long would you like to spend (on average) per week on EPO?**

Time to Spend	On Preparation	On Engagement
I don't want to participate in EPO	4 (3%)	4 (3%)
0-1 Hrs	60 (46%)	41 (31%)
1-3 Hrs	45 (34%)	55 (42%)
3-5 Hrs	13 (10%)	15 (12%)
5-10 Hrs	5 (3%)	10 (8%)
>10 Hrs	4 (3%)	6 (5%)

Table 6.1: Current (a) and desired (b) time commitment to EPO.

DURING WORK HOURS (7%). Two percent of respondents chose I DON'T KNOW. We analyzed this question by the demographic groups outlined in Section 6.2.2 and divided respondents into two categories: those who engage in EPO only in their free time, and those who engage in EPO at work.<sup>12</sup> Chi-squared tests show that differences between most demographic groups are not significant. However, we do find some evidence that

<sup>12</sup>This grouping was chosen such that we would have sufficient statistics for a chi-squared test. The group of respondents who engage in EPO during work hours and during free time was collapsed with the group who engage in EPO during work hours only.

a larger fraction of non-tenured (26%) versus tenured (6%) respondents engage in EPO only during their free time ( $\chi^2 = 9.02, p = 0.0027$ ).

### 6.3.2 Motives and Deterrents

Several survey items were intended to probe why respondents may or not engage in EPO activities. Through these items we also sought to understand if respondents feel that engaging in EPO is part of their duty as a member of the larger scientific community.

When asked whether they think engaging in EPO is part of their professional responsibility as a scientist, 69% of respondents answered with an unequivocal YES. When asked if it *should* be part of their professional responsibility, this fraction rose to 76%. When asked instead whether they believed it should be a *personal* responsibility of a scientist, 80% responded YES unequivocally. Some respondents instead answered these questions with a conditional. In each case, less than 12% responded YES, BUT ONLY EDUCATION (I.E., UNDERGRADUATE TEACHING OR MENTORSHIP) and less than 4% responded YES, BUT ONLY PUBLIC OUTREACH (I.E., PUBLIC LECTURES OR VOLUNTEERING AT SCIENCE FESTIVALS). We further examined these results by comparing the responses regarding perceived responsibility across the different demographic groups outlined in Section 6.2.2. After performing chi-squared tests of independence we find that the differences between the fraction who selected YES among these groups are not statistically significant ( $p > 0.05$  for all comparisons).

Furthermore, we asked respondents about their general motivations for engaging in EPO and any factors which deter their engagement. Parts of these questions explicitly addressed how funding (or lack thereof) affects these motives and/or deterrents. Figure 6.3 presents the distribution of responses for motivating factors. The most popular motivating factor for participating in EPO is the desire to educate the general public (80%); this is closely followed by respondents engaging in EPO because they find it personally enjoyable (73%). When asked how funding impacts EPO engagement, 17% of respondents indicated they are currently funded specifically to participate in EPO, and 21% indicated

they hope engaging in EPO will help them secure future funding.

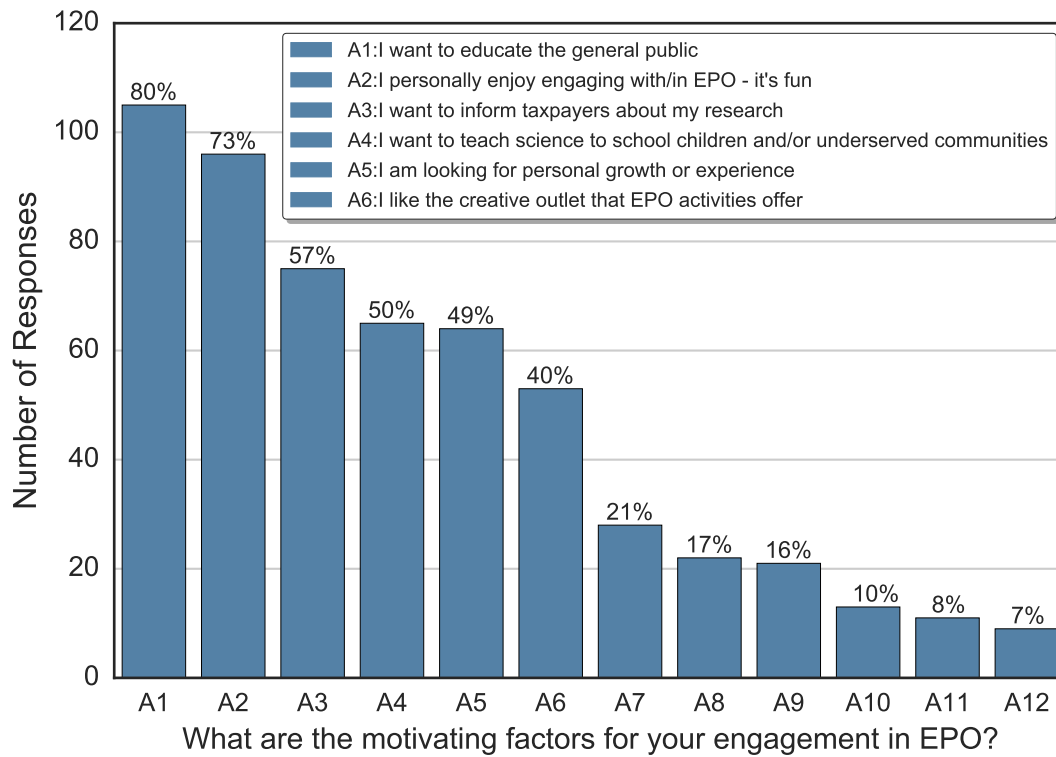


Figure 6.3: Distribution of checked motivating factors towards EPO engagement. Respondents were provided a list of possible motivating factors for EPO engagement and asked to check all that apply. Complete descriptions for provided list of factors, some of which are present in the legend, are given in Table A.1.

When asked about barriers to engagement, lack of time was overwhelmingly the most popular response (52%). We note that in this survey item, there was no distinction made between time spent at work or personal time, or any conflict between spending time on EPO and research. Funding was also indicated to be an issue, as 19% of respondents indicated they “are not funded to do EPO.” Additionally, respondents indicated that they felt they lacked the skills and/or training to engage in EPO activities (16%). A subset of respondents noted that cultural (3%) and language (6%) barriers prohibited their involvement in EPO activities.

Issues with program logistics were another barrier to engagement. In a free-response option, several respondents reported that they did not want to participate in the organization or administration of activities and/or that they were not aware of current opportunities for engagement. The desire for an “EPO specialist” to facilitate scientists’ EPO engagement was prominent amongst those who reported barriers.

We concluded this portion of the survey by asking scientists about factors which might encourage increased participation in EPO activities. Results are displayed in Figure 6.4. Three important themes emerged from the responses. The first is a response to the previously discussed barrier of lack of time. Many respondents indicated they would be more inclined to participate in EPO if they felt they could allocate more time during the work week (53%) and if EPO were listed as an explicit component of their job descriptions (46%). In addition, the desire for changes in the cultural value of EPO within the astronomy community was evident. Respondents indicated that they would feel more inclined to participate in EPO if doing so would help with career development (26%), if doing so were encouraged by supervisors/managers (34%), and if doing so were more highly regarded among peers (39%). These responses suggest that amongst  $\gtrsim 30\%$  of respondents there exists a perception that 1) EPO does not positively contribute towards successful careers in academia, and 2) there is a perceived stigma surrounding participation in EPO in academic culture, at least in the context of physics and astronomy.

### 6.3.3 Centralization

As a primarily grass-roots effort, analysis of the development and implementation of the DES EPO program offers important insight for future large collaborations [Wolf et al., 2018]. The final section of our survey focused on EPO in large collaborations, both for the purpose of self-reflection for the DES EPO organizational team, and to offer suggestions for future EPO programs.

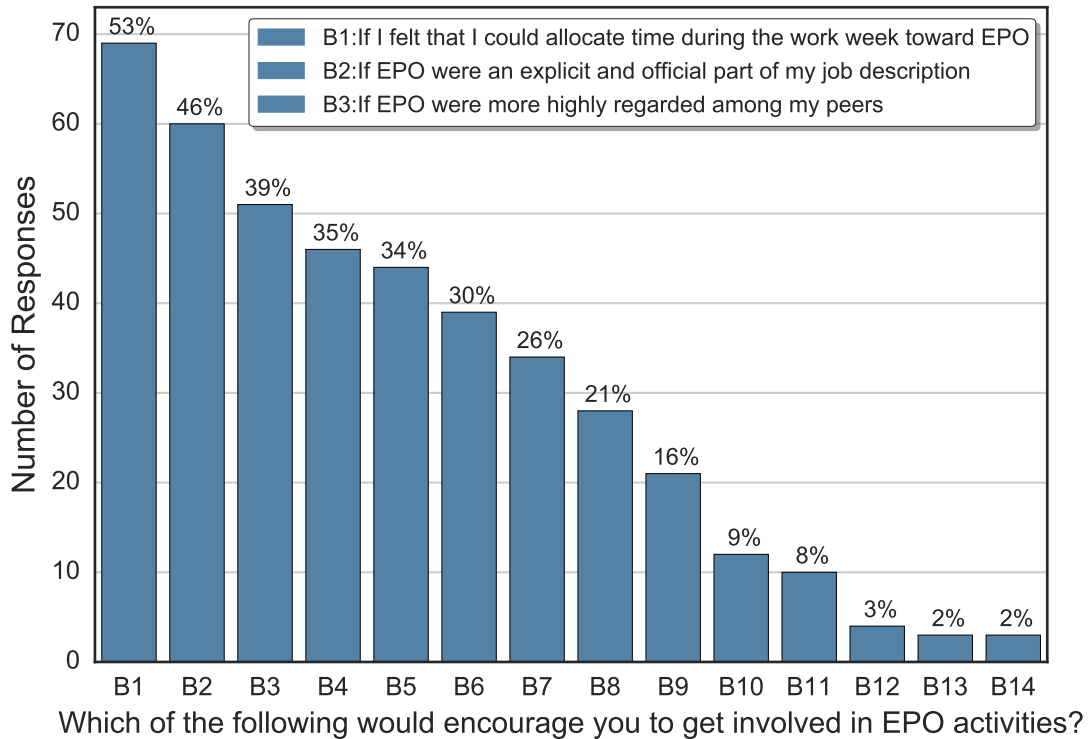


Figure 6.4: Distribution of checked factors which would encourage future EPO engagement. Respondents were provided with a list of possible incentives to encourage participation in EPO activities and asked to check all which might increase their motivation. Respondents could also write in their own responses; these have been combined into the “Other” category. Complete descriptions for provided list of factors, some of which are present in the legend, are given in Table A.2.

### 6.3.3.1 Views of EPO Across the DES Collaboration

Survey respondents were asked to rank the value they believe four DES-related groups place upon EPO. Respondents were asked to provide an answer using a 5-point Likert scale: 1 = NOT AT ALL to 5 = VERY MUCH. Respondents were also given an I DON’T KNOW option. Table 6.2 summarizes the responses for four DES-related groups. The groups chosen for this item were intended to span the scope of an individual scientist’s involvement with DES, from a collaboration-wide level (A. the DES collaboration as a

whole and B. those in collaboration management positions) to more personal interactions with other DES members (C. within a scientific working group or D. local to an institution).

Generally, respondents indicated that each of the four DES groups place mid to high value upon EPO. When asked to rank the view of the DES collaboration as a whole, the mean (standard deviation) of the responses was 3.7 (0.97). When asked to rank the value DES management places upon EPO, the mean (standard deviation) of the responses was 3.5 (1.05). Notably, the number of I DON'T KNOW responses was also highest when asked about the value DES management places on EPO ( $n = 28$ ).

#### **Rank how much you think the following DES groups value EPO.**

DES Group	(Very Little)				(Very Much)		I Don't Know
	1	2	3	4	5		
DES Collaboration	1 (1%)	10 (9%)	40 (35%)	36 (31%)	29 (25%)	15	
DES Management	4 (4%)	10 (10%)	38 (37%)	29 (28%)	22 (21%)	28	
Your DES Working Group	11 (10%)	28 (26%)	29 (27%)	21 (20%)	18 (17%)	24	
DES Members at Your Institution	5 (4%)	22 (19%)	29 (25%)	35 (30%)	26 (22%)	14	

Table 6.2: Responses for the Likert survey item: “Rank how much you think the following DES groups value EPO.” Respondents were asked to rank on a 5-point scale: 1=“Very Little” to 5=“Very Much.” Respondents were also given the opportunity to answer “I Don’t Know.” Percentages listed in the table correspond to the fraction from the total responses using the Likert scale only.

The reported value placed upon EPO in the smaller DES groups was less favorable than that of the groups on the collaboration-wide level. The mean values (standard deviations) of the responses for the working groups and individual institutions were 3.1 (1.24)

and 3.5 (1.15), respectively. But it is important to note that 36% of respondents ( $n = 107$ ) indicated little value (response of 1 or 2) when asked to rank the value of EPO amongst individual science working groups, and 23% of respondents ( $n = 117$ ) indicated little value when asked about DES members at their own institutions.

### **6.3.3.2 Centralized Support for EPO Engagement**

Respondents were asked how DES and other large science collaborations could best support collaboration-wide engagement in EPO. The most popular response (57%) suggested that collaborations build and maintain a repository of talks, slides, curricula, etc., that can be used in various EPO activities (including both DES-sponsored and locally-organized programs). The second most popular response involved funding: 54% of respondents suggested collaborations could incentivize EPO participation by explicitly allocating funding for EPO projects. Another popular response (52%) suggested that collaborations consider EPO as valuable time spent toward science infrastructure, and that this would ultimately lead to returns with high scientific value. These returns might include the ability to access data even after one leaves a collaboration member institution (i.e., data rights) or the ability to be a co-author on any collaboration publication (i.e., authorship rights). Other popular responses included that collaborations hire dedicated EPO staff (48%) and that collaborations could provide communication training for scientists (37%).

In addition to checking predetermined answers for this survey item, respondents had the ability to write in responses. Of the seven written responses, four mentioned the role of collaborations in changing the cultural perspective of EPO within the physics community. Responses included calling for a change of community value, instituting EPO engagement as an important factor in job applications for early career scientists, and calling for changing the perceived cultural norm that engaging in EPO is secondary, in terms of time and status, to research. Another point illuminated by the written responses was the desire to see a quantitative measure of the impact of EPO.

Finally, scientists were asked to answer an open-ended question regarding the value of

centralizing EPO efforts for large science collaborations. Of the 81 responses, 70 were for centralization, seven were against, and four found the question unclear and/or were unsure of the value of a central EPO program. Responses not immediately in favor of centralization included thoughts that an international collaboration should develop EPO programs specific to each participating country and that scientists should not spend their time on efforts not directly related to the project’s primary science goals. These responses also illuminated that respondents had differing views of the meaning of “centralization.” Some respondents interpreted it as an effort to facilitate EPO via making repositories or other means of coordination, while others had a more reductionist view, in which centralized EPO is a mechanism which replaces individual EPO activities. In the latter responses, respondents expressed that collaboration-organized EPO does not provide support to more localized or community-oriented events.

## 6.4 Conclusions

In this article we presented survey results from a case study of the attitudes of astronomers, physicists, and astrophysicists towards EPO. The study was conducted using 131 responses from scientists in the international Dark Energy Survey collaboration. The survey was designed to explore general attitudes towards STEM EPO as well as those in the context of large-scale science collaborations. We note that as participation in the survey was voluntary, it is likely that respondents already had an interest in EPO engagement, resulting in a possible selection bias.

As discussed in Section 6.3.1, we find a disparity between the EPO activities in which respondents are involved (e.g., public presentations and teaching) and those that, in their opinion, would have more impact on the general public (e.g., on-air media and elementary or high school teacher development). We speculate that perhaps the respondents do not know how to personally effect change in the arena of formal education, specifically since it is outside of their professional responsibilities, and that the opportunity to achieve such

development via official organizations may be lacking. The low engagement we find in science writing and on-air media may be similarly explained due to their specialized and freelance nature — not many people have the skill or opportunity to perform such tasks. The true reason for these differences would be interesting to pursue in future studies.

Similar sentiments are reflected in the responses to questions of time commitment to EPO. Respondents reported that they spend less time preparing and engaging in EPO than they would like. This lack of time was also mentioned in Section 6.3.2 as the largest barrier preventing engagement in EPO, along with lack of funding, training and/or skills, and interest in performing organizational duties for EPO activities. As for what currently motivates them to engage in EPO, respondents stated a desire to educate the general public, reach minorities and under-served communities, and inform taxpayers of the work they are doing. Respondents also reported that they experience personal enjoyment from engaging in EPO, consider it as an opportunity for personal growth, and view it as a means to secure future funding (some government agencies require EPO components in their grant proposals). Furthermore, the majority of respondents believe that engaging in EPO-related activities is and should be a personal and professional responsibility of scientists.

Where possible, we performed chi-squared tests to determine any statistically significant differences between the opinions and behaviors of various demographic groups described in Section 6.2.2. In a comparison of *when* respondents engage in EPO, we find a significant difference in the behaviors of tenured versus non-tenured scientists. We hypothesize that this may be because non-tenured scientists feel that engaging in EPO during work hours is not appropriate or that their supervisors would not approve of such a use of work time. Respondents with tenure, however, may feel more in control of their time, or are perhaps even mandated by institutions and/or funding agencies to engage in EPO (particularly undergraduate education and mentorship) during work hours. Unfortunately, our small sample size prohibited our ability to perform this type of analysis for the majority of survey items. We believe that a similar analysis with a much larger

sample size, as well as more carefully designed demographic groupings (e.g., for organizations wishing to increase EPO engagement amongst early career scientists), would be a compelling pursuit for a future study.

Another interesting result of this study is the comparison between individual feelings about EPO, as summarized above, and how scientists perceive the feelings of their colleagues. When consolidating responses from various sections of the survey, we observe that the perceived culture surrounding engagement in EPO in the physics and astronomy academic communities can have an (often negative) effect on scientists' engagement. This perception is consistent with results from other studies exploring physicists' and astronomers' attitudes towards EPO. As more empirical evidence for this effect is collected, it has become clear that to facilitate EPO engagement, scientists in leadership (or mentoring) roles who support EPO engagement will need to better express their opinions in order to cultivate a more supportive and conducive environment.

This perceived stigma is particularly interesting when discussed in the context of broader scientific collaborations. When asked to rate how four different DES groups value EPO, we find that respondents believe working groups and members of their own institution place less value on EPO than the management and collaboration as a whole. We believe this could be due to two factors. First, the primary goal of the science working groups is to engage in research, and thus communicating scientific results outside of academia is not prioritized. The second contributing factor may be that the centralized EPO coordination did not extend throughout the hierarchy of DES infrastructure, i.e., there were no DES EPO representatives actively liaising between the EPO Committee and the working groups. Therefore, there was not an established channel of communication to regularly inform individual working-group members of EPO events. We recognize that despite this disparity across groups, the perceived value placed on EPO is a medium to high value for all groups (Table 6.2). Yet in Figure 6.4, respondents claim that they would be encouraged to engage in more EPO if it were more highly regarded among their peers. It may be that there are general perceptions that 1) while EPO is valued, it must

be secondary to other duties, such as research, or 2) EPO is not valued by the people scientists interact with most regularly (and is instead only valued by funding agencies or those in leadership positions).

Furthermore, the fraction of respondents that indicated that they do not know the value that DES management places upon EPO is curious, given the various communication vehicles available to DES leadership.<sup>13</sup> It is possible that, in general, collaboration members feel removed from the DES leadership and do not feel confident in assigning a value to someone else's opinion. For example, an individual collaboration member may have a much closer rapport with a colleague at his/her institution than someone on the DES management committee. We also posit that while verbal support was given by the DES leadership to the DES EPO Committee [Wolf et al., 2018], the same support was not effectively communicated to the collaboration as a whole.

Responses to items throughout Section 6.3.3 highlight three key messages about centralizing EPO for collaborations. First, the responses suggest that effective collaboration-sponsored EPO programming, at least in the minds of collaboration scientists, requires a team dedicated to program organization, communication, and implementation. For example, building and maintaining a presentation slide and image repository is a substantial task which would require significant time and infrastructure expertise. Second, responses suggest the potential need for reevaluation of the allocation of EPO funding and the associated explicit directives for EPO engagement. This reconsideration of the funding stream is essential with respect to the collaboration leadership who are responsible for managing funds, but also possibly with respect to the greater sources of collaboration funding (i.e., government agencies and private foundations). Third, we find evidence that if collaborations want to foster EPO participation, collaboration leadership and others in positions to affect collaboration culture should work to cultivate a community where spending time

---

<sup>13</sup>As discussed in Wolf et al. [2018], collaboration meetings, collaboration-wide telephone conferences, and the DES LISTSERV are available to the DES leadership to make announcements and update collaboration members.

on EPO is viewed as a positive use of time and resources.

Based on the results presented here, we propose the following recommendations for those wishing to increase EPO participation amongst physicists, astronomers, and astrophysicists:

## **1. For the scientist**

- (a) Engage in discussion about EPO activities with peers to foster open dialogue.

Suggested points for discussion include: merits of EPO engagement, time spent on activities, and assumed perceptions versus reality of beliefs within the academic community. (Sections 6.3.1 and 6.3.2)

- (b) Seek expertise of social science and EPO professionals to learn more about EPO evaluation, assessment design, and impact metrics. Collaborate with these professionals to measure impact of EPO engagement for both intended audiences and participating scientists. (Section 6.3.2)

## **2. For scientists in positions of leadership**

- (a) Explicitly discuss expectations concerning time spent engaging in EPO in scientific job descriptions and interviews, independent of interviewee status, i.e., for graduate students, post-docs, faculty, etc. (Section 6.3.2)

- (b) Clearly outline EPO-related policies and support through different channels: emails, official communications, Memoranda of Understanding (e.g., with science collaborations), and presentations. (Section 6.3.3.1)

- (c) Institute discussion about how science goals and policies can align with EPO goals. (Section 6.3.3.1)

- (d) Create incentives like rewarding investment in EPO with benefits such as data rights and authorship on papers. Collaborate with EPO facilitators and funding agencies to develop further incentives (Section 6.3.3)

- (e) Open communication with funding agencies to discuss sources of EPO funding and how these funds are managed. (Sections 6.3.2 and 6.3.3.2)
- (f) Consider hiring dedicated staff to organize, develop, facilitate, and evaluate EPO activities. (Sections 6.3.2 and 6.3.3.2)

### **3. For EPO organizers and facilitators**

- (a) Survey participating scientists to inform program organization. Develop activities which align with the types of activities in which scientists are already involved. (Section 6.3.1)
- (b) Provide an estimate of required time necessary to participate in an EPO event, keeping in mind that most scientists want to spend 0-3 hours per week on average engaging in EPO activities. (Sections 6.3.1 and 6.3.2)
- (c) Devote resources and time towards infrastructure (e.g., organize and prepare for events, curate presentation materials) to increase scientist engagement during events. (Section 6.3.3.2)
- (d) Clearly identify the roles of EPO organizers and facilitators amongst scientists. Describe how centralized EPO efforts fit into the context of EPO with local institutions and communities, as well as within the greater project. (Section 6.3.3.2)
- (e) Discuss EPO program evaluation design and results with scientists interested in measures of impact. (Section 6.3.3.2)
- (f) Collaborate with scientists in leadership positions and funding agencies to develop incentives for EPO participation. (Section 6.3.3)

# **Appendices**

## **Appendix A**

**Full list of survey item options for  
responses presented in Figures 6.3  
and 6.4.**

**In general, what are the motivating factors for your engagement in EPO? Check all that apply.**

Figure Key	Item Response Text
A1	I want to educate the general public
A2	I personally enjoy engaging with/in EPO - it's fun
A3	I want to inform taxpayers about my research
A4	I want to teach science to school children and/or underserved communities
A5	I am looking for personal growth or experience
A6	I like the creative outlet that EPO activities offer
A7	I hope that my engagement in EPO will help earn me future funding
A8	I am funded to engage in EPO
A9	I am on the job market and think EPO will boost my resume/CV
A10	I want to be famous
A11	I am mandated to engage in EPO by my local institution/department
A12	I am not interested in participating in EPO

Table A.1: Complete list of possible answers for the survey item presented in Figure 6.3. Responses are listed in descending order, i.e., A1 was the most popular response, rather than the order in which they were presented in the survey item.

**Which of the following would encourage you to get involved (or more involved) in  
EPO activities? Check all that apply.**

---

Figure Key	Item Response Text
B1	If I felt that I could allocate time during the work week toward EPO
B2	If EPO were an explicit and official part of my job description
B3	If EPO were more highly regarded among my peers
B4	If the necessary EPO infrastructure already existed and someone else told me how I could help
B5	If EPO were encouraged by my supervisor or the managers of my department/institution/collaboration
B6	If I saw more evidence that EPO makes a positive impact on society
B7	If EPO helped with my career development
B8	If it were easier to obtain funds for EPO activities
B9	If I knew how to efficiently communicate the technical aspects of my work to the public
B10	None of the above
B11	If I shared the same language as my local community
B12	Other
B13	If I shared the same culture as my local community
B14	If I shared the same ethnicity as my local community

---

Table A.2: Complete list of possible answers for the survey item presented in Figure 6.4. Responses are listed in descending order, i.e., B1 was the most popular response, rather than the order in which they were presented in the survey item.

# Bibliography

T. Abbott, F. B. Abdalla, J. Aleksić, S. Allam, A. Amara, D. Bacon, E. Balbinot, M. Banerji, K. Bechtol, A. Benoit-Lévy, G. M. Bernstein, E. Bertin, J. Blazek, C. Bonnett, S. Bridle, D. Brooks, R. J. Brunner, E. Buckley-Geer, D. L. Burke, G. B. Caminha, D. Capozzi, J. Carlsen, A. Carnero-Rosell, M. Carollo, M. Carrasco-Kind, J. Carretero, F. J. Castander, L. Clerkin, T. Collett, C. Conselice, M. Crocce, C. E. Cunha, C. B. D’Andrea, L. N. da Costa, T. M. Davis, S. Desai, H. T. Diehl, J. P. Dietrich, S. Dodelson, P. Doel, A. Drlica-Wagner, J. Estrada, J. Etherington, A. E. Evrard, J. Fabbri, D. A. Finley, B. Flaugher, R. J. Foley, P. Fosalba, J. Frieman, J. García-Bellido, E. Gaztanaga, D. W. Gerdes, T. Giannantonio, D. A. Goldstein, D. Gruen, R. A. Gruendl, P. Guarnieri, G. Gutierrez, W. Hartley, K. Honscheid, B. Jain, D. J. James, T. Jeltema, S. Jouvel, R. Kessler, A. King, D. Kirk, R. Kron, K. Kuehn, N. Kuropatkin, O. Lahav, T. S. Li, M. Lima, H. Lin, M. A. G. Maia, M. Makler, M. Manera, C. Maraston, J. L. Marshall, P. Martini, R. G. McMahon, P. Melchior, A. Merson, C. J. Miller, R. Miquel, J. J. Mohr, X. Morice-Atkinson, K. Naidoo, E. Neilsen, R. C. Nichol, B. Nord, R. Ogando, F. Ostrovski, A. Palmese, A. Papadopoulos, H. V. Peiris, J. Peoples, W. J. Percival, A. A. Plazas, S. L. Reed, A. Refregier, A. K. Romer, A. Roodman, A. Ross, E. Rozo, E. S. Rykoff, I. Sadeh, M. Sako, C. Sánchez, E. Sanchez, B. Santiago, V. Scarpine, M. Schubnell, I. Sevilla-Noarbe, E. Sheldon, M. Smith, R. C. Smith, M. Soares-Santos, F. Sobreira, M. Soumagnac, E. Suchyta, M. Sullivan, M. Swanson, G. Tarle, J. Thaler, D. Thomas, R. C. Thomas, D. Tucker, J. D. Vieira, V. Vikram, A. R. Walker, R. H. Wechsler, J. Weller, W. Wester, L. Whiteway, H. Wilcox, B. Yanny,

Y. Zhang, and J. Zuntz. The dark energy survey: more than dark energy – an overview. *Monthly Notices of the Royal Astronomical Society*, 460(2):1270–1299, 2016. doi: 10.1093/mnras/stw641. URL <http://dx.doi.org/10.1093/mnras/stw641>.

Adam Amara and Alexandre Réfrégier. Systematic bias in cosmic shear: extending the fisher matrix. *Monthly Notices of the Royal Astronomical Society*, 391(1):228–236, 2008. doi: 10.1111/j.1365-2966.2008.13880.x. URL <http://dx.doi.org/10.1111/j.1365-2966.2008.13880.x>.

George Z. Angeli, Jennifer Dunn, Scott C. Roberts, Douglas G. MacMynowski, Anna Segurson, Konstantinos Vogiatzis, and Joeleff Fitzsimmons. Modeling tools to estimate the performance of the thirty meter telescope: An integrated approach. *Proceedings of SPIE*, 5497:237–250, 2004.

S. Arnouts, L. Moscardini, E. Vanzella, S. Colombi, S. Cristiani, A. Fontana, E. Giallongo, S. Matarrese, and P. Saracco. Measuring the redshift evolution of clustering: the hubble deep field south. *Monthly Notices of the Royal Astronomical Society*, 329: 355–366, 2002.

Matthias Bartelmann and Ramesh Narayan. Gravitational lensing and the mass distribution of clusters. *AIP Conference Proceedings*, 336, 1995.

Matthias Bartelmann and Peter Schneider. Weak gravitational lensing. *Physics Reports*, 340:291–472, 2001.

N. Benítez. Bayesian Photometric Redshift Estimation. *ApJ*, 536:571–583, June 2000. doi: 10.1086/308947.

Jon Louis Bentley. Multidimensional binary search trees used for associative searching. *Commun. ACM*, 18(9):509–517, September 1975. ISSN 0001-0782. doi: 10.1145/361002.361007. URL <http://doi.acm.org/10.1145/361002.361007>.

- G. Bernstein and D. Huterer. Catastrophic photometric redshift errors: weak-lensing survey requirements. *MNRAS*, 401:1399–1408, January 2010. doi: 10.1111/j.1365-2966.2009.15748.x.
- G. M. Bernstein and R. Armstrong. Bayesian lensing shear measurement. *Monthly Notices of the Royal Astronomical Society*, 438(1880), 2014.
- G. M. Bernstein and D. Gruen. Resampling Images in Fourier Domain. *PASP*, 126:287, March 2014. doi: 10.1086/675812.
- G. M. Bernstein and M. Jarvis. Shapes and Shears, Stars and Smears: Optimal Measurements for Weak Lensing. *AJ*, 123:583–618, February 2002.
- Gary M. Bernstein, Robert Armstrong, Christina Krawiec, and Marisa C. March. An accurate and practical method for inference of weak gravitational lensing from galaxy images. *Monthly Notices of the Royal Astronomical Society*, 459(4):4467–4484, 2016. doi: 10.1093/mnras/stw879. URL <http://dx.doi.org/10.1093/mnras/stw879>.
- Sarah Bridle, John Shawe-Taylor, Adam Amara, Douglas Applegate, Sreekumar T. Balan, Joel Berge, Gary Bernstein, Hakon Dahle, Thomas Erben, Mandeep Gill, Alan Heavens, Catherine Heymans, F. William High, Henk Hoekstra, Mike Jarvis, Donnacha Kirk, Thomas Kitching, Jean-Paul Kneib, Konrad Kuijken, David Lagatutta, Rachel Mandelbaum, Richard Massey, Yannick Mellier, Baback Moghaddam, Yassir Moudden, Reiko Nakajima, Stephane Paulin-Henriksson, Sandrine Pires, Anais Rassat, Alexandre Refregier, Jason Rhodes, Tim Schrabback, Elisabetta Semboloni, Marina Shmakova, Ludovic van Waerbeke, Dugan Witherick, Lisa Voigt, and David Wittman. Handbook for the great08 challenge: An image analysis competition for cosmological lensing. *Ann. Appl. Stat.*, 3(1):6–37, 03 2009. doi: 10.1214/08-AOAS222. URL <https://doi.org/10.1214/08-AOAS222>.
- T. W. Burns, D. J. O’Connor, and S. M. Stocklmayer. Science communication: A con-

- temporary definition. *Public Understanding of Science*, 12(2):183–202, 2003. doi: 10.1177/09636625030122004.
- B. Casaponsa, A. F. Heavens, T. D. Kitching, L. Miller, R. B. Sarreiro, and E. Martínez-González. Size magnification as a complement to cosmic shear. *Monthly Notices of the Royal Astronomical Society*, 430:2844–2853, 2013.
- C. Chang, M. Jarvis, B. Jain, S. M. Kahn, D. Kirkby, A. Connolly, S. Krughoff, E.-H. Peng, and J. R. Peterson. The effective number density of galaxies for weak lensing measurements in the LSST project. *MNRAS*, 434:2121–2135, September 2013. doi: 10.1093/mnras/stt1156.
- J. Clampitt, C. Sánchez, J. Kwan, E. Krause, N. MacCrann, Y. Park, M. A. Troxel, B. Jain, E. Rozo, E. S. Rykoff, R. H. Wechsler, J. Blazek, C. Bonnett, M. Crocce, Y. Fang, E. Gaztanaga, D. Gruen, M. Jarvis, R. Miquel, J. Prat, A. J. Ross, E. Sheldon, J. Zuntz, T. M. C. Abbott, F. B. Abdalla, R. Armstrong, M. R. Becker, A. Benoit-Lévy, G. M. Bernstein, E. Bertin, D. Brooks, D. L. Burke, A. Carnero Rosell, M. Carrasco Kind, C. E. Cunha, C. B. D’Andrea, L. N. da Costa, S. Desai, H. T. Diehl, J. P. Dietrich, P. Doel, J. Estrada, A. E. Evrard, A. Fausti Neto, B. Flaugher, P. Fosalba, J. Frieman, R. A. Gruendl, K. Honscheid, D. J. James, K. Kuehn, N. Kuropatkin, O. Lahav, M. Lima, M. March, J. L. Marshall, P. Martini, P. Melchior, J. J. Mohr, R. C. Nichol, B. Nord, A. A. Plazas, A. K. Romer, E. Sanchez, V. Scarpine, M. Schubnell, I. Sevilla-Noarbe, R. C. Smith, M. Soares-Santos, F. Sobreira, E. Suchyta, M. E. C. Swanson, G. Tarle, D. Thomas, V. Vikram, and A. R. Walker. Galaxy-galaxy lensing in the dark energy survey science verification data. *Monthly Notices of the Royal Astronomical Society*, 465(4):4204–4218, 2017. doi: 10.1093/mnras/stw2988. URL <http://dx.doi.org/10.1093/mnras/stw2988>.
- L. Dang and P. Russo. How Astronomers View Education and Public Outreach: An Exploratory Study. *Communicating Astronomy with the Public Journal*, 18:16, September 2015.

Dark Energy Survey Collaboration, T. Abbott, F. B. Abdalla, J. Aleksić, S. Allam, A. Amara, D. Bacon, E. Balbinot, M. Banerji, K. Bechtol, A. Benoit-Lévy, G. M. Bernstein, E. Bertin, J. Blazek, C. Bennett, S. Bridle, D. Brooks, R. J. Brunner, E. Buckley-Geer, D. L. Burke, G. B. Caminha, D. Capozzi, J. Carlsen, A. Carnero-Rosell, M. Carollo, M. Carrasco-Kind, J. Carretero, F. J. Castander, L. Clerkin, T. Collett, C. Conselice, M. Crocce, C. E. Cunha, C. B. D’Andrea, L. N. da Costa, T. M. Davis, S. Desai, H. T. Diehl, J. P. Dietrich, S. Dodelson, P. Doel, A. Drlica-Wagner, J. Estrada, J. Etherington, A. E. Evrard, J. Fabbri, D. A. Finley, B. Flaugher, R. J. Foley, P. Fosalba, J. Frieman, J. García-Bellido, E. Gaztanaga, D. W. Gerdes, T. Giannantonio, D. A. Goldstein, D. Gruen, R. A. Gruendl, P. Guarnieri, G. Gutierrez, W. Hartley, K. Honscheid, B. Jain, D. J. James, T. Jeltema, S. Jouvel, R. Kessler, A. King, D. Kirk, R. Kron, K. Kuehn, N. Kuropatkin, O. Lahav, T. S. Li, M. Lima, H. Lin, M. A. G. Maia, M. Makler, M. Manera, C. Maraston, J. L. Marshall, P. Martini, R. G. McMahon, P. Melchior, A. Merson, C. J. Miller, R. Miquel, J. J. Mohr, X. Morice-Atkinson, K. Naidoo, E. Neilsen, R. C. Nichol, B. Nord, R. Ogando, F. Ostrovski, A. Palmese, A. Papadopoulos, H. V. Peiris, J. Peoples, W. J. Percival, A. A. Plazas, S. L. Reed, A. Refregier, A. K. Romer, A. Roodman, A. Ross, E. Rozo, E. S. Rykoff, I. Sadeh, M. Sako, C. Sánchez, E. Sanchez, B. Santiago, V. Scarpine, M. Schubnell, I. Sevilla-Noarbe, E. Sheldon, M. Smith, R. C. Smith, M. Soares-Santos, F. Sobreira, M. Soumagnac, E. Suchyta, M. Sullivan, M. Swanson, G. Tarle, J. Thaler, D. Thomas, R. C. Thomas, D. Tucker, J. D. Vieira, V. Vikram, A. R. Walker, R. H. Wechsler, J. Weller, W. Wester, L. Whiteway, H. Wilcox, B. Yanny, Y. Zhang, and J. Zuntz. The Dark Energy Survey: more than dark energy - an overview. *Monthly Notices of the Royal Astronomical Society*, 460:1270–1299, August 2016. doi: 10.1093/mnras/stw641.

L. J. M. Davies, C. Maraston, D. Thomas, D. Capozzi, R. H. Wechsler, M. T. Busha, M. Banerji, F. Ostrovski, C. Papovich, B. X. Santiago, R. Nichol, M. A. G. Maia, and L. N. da Costa. Detecting massive galaxies at high redshift using the dark energy survey. *Monthly Notices of the Royal Astronomical Society*, 434:296–312, 2013.

- A. Farahi, R. R. Gupta, C. Krawiec, A. A. Plazas, and R. C. Wolf. Astronomers' and physicists' attitudes towards education & public outreach: A case study with the dark energy survey. *arXiv:1804.00591*, 2018.
- B. Flaugher, H. T. Diehl, K. Honscheid, T. M. C. Abbott, O. Alvarez, R. Angstadt, J. T. Annis, M. Antonik, O. Ballester, L. Beaufore, G. M. Bernstein, R. A. Bernstein, B. Bigelow, M. Bonati, D. Boprie, D. Brooks, E. J. Buckley-Geer, J. Campa, L. Cardiel-Sas, F. J. Castander, J. Castilla, H. Cease, J. M. Cela-Ruiz, S. Chappa, E. Chi, C. Cooper, L. N. da Costa, E. Dede, G. Derylo, D. L. DePoy, J. de Vicente, P. Doel, A. Drlica-Wagner, J. Eiting, A. E. Elliott, J. Emes, J. Estrada, A. Fausti Neto, D. A. Finley, R. Flores, J. Frieman, D. Gerdes, M. D. Gladders, B. Gregory, G. R. Gutierrez, J. Hao, S. E. Holland, S. Holm, D. Huffman, C. Jackson, D. J. James, M. Jonas, A. Karcher, I. Karliner, S. Kent, R. Kessler, M. Kozlovsky, R. G. Kron, D. Kubik, K. Kuehn, S. Kuhlmann, K. Kuk, O. Lahav, A. Lathrop, J. Lee, M. E. Levi, P. Lewis, T. S. Li, I. Mandrichenko, J. L. Marshall, G. Martinez, K. W. Merritt, R. Miquel, F. Muñoz, E. H. Neilsen, R. C. Nichol, B. Nord, R. Ogando, J. Olsen, N. Palaio, K. Patton, J. Peoples, A. A. Plazas, J. Rauch, K. Reil, J.-P. Rheault, N. A. Roe, H. Rogers, A. Roodman, E. Sanchez, V. Scarpine, R. H. Schindler, R. Schmidt, R. Schmitt, M. Schubnell, K. Schultz, P. Schurter, L. Scott, S. Serrano, T. M. Shaw, R. C. Smith, M. Soares-Santos, A. Stefanik, W. Stuermer, E. Suchyta, A. Sypniewski, G. Tarle, J. Thaler, R. Tighe, C. Tran, D. Tucker, A. R. Walker, G. Wang, M. Watson, C. Weaverdyck, W. Wester, R. Woods, B. Yanny, and The DES Collaboration. The dark energy camera. *The Astronomical Journal*, 150(5):150, 2015.
- M. Garcia-Fernandez, E. Sanchez, I. Sevilla-Noarbe, E. Suchyta, E. M. Huff, E. Gaztanaga, J. Aleksić, R. Ponce, F. J. Castander, B. Hoyle, T. M. C. Abbott, F. B. Abdalla, S. Allam, J. Annis, A. Benoit-Lévy, G. M. Bernstein, E. Bertin, D. Brooks, E. Buckley-Geer, D. L. Burke, A. Carnero Rosell, M. Carrasco Kind, J. Carretero, M. Crocce, C. E. Cunha, C. B. D'Andrea, L. N. da Costa, D. L. DePoy, S. Desai, H. T. Diehl,

T. F. Eifler, A. E. Evrard, E. Fernandez, B. Flaugher, P. Fosalba, J. Frieman, J. García-Bellido, D. W. Gerdes, T. Giannantonio, D. Gruen, R. A. Gruendl, J. Gschwend, G. Gutierrez, D. J. James, M. Jarvis, D. Kirk, E. Krause, K. Kuehn, N. Kuropatkin, O. Lahav, M. Lima, N. MacCrann, M. A. G. Maia, M. March, J. L. Marshall, P. Melchior, R. Miquel, J. J. Mohr, A. A. Plazas, A. K. Romer, A. Roodman, E. S. Rykoff, V. Scarpine, M. Schubnell, R. C. Smith, M. Soares-Santos, F. Sobreira, G. Tarle, D. Thomas, A. R. Walker, W. Wester, and The DES Collaboration. Weak lensing magnification in the dark energy survey science verification data. *Monthly Notices of the Royal Astronomical Society*, 476(1):1071–1085, 2018. doi: 10.1093/mnras/sty282.  
URL <http://dx.doi.org/10.1093/mnras/sty282>.

Mauro Giavalisco. The properties of lyman-break galaxies at redshift  $z \approx 3$ . *The Hubble Deep Field*, 1998.

*WindMaster & WindMaster Pro Ultrasonic Anemometer: User Manual*. Gill Instruments Limited, 2010.

André Heck and Claus Madsen. *Astronomy communication*, volume 290. Springer Science & Business Media, 2013.

H. Hildebrandt, J. Pielorz, T. Erben, L. van Waerbeke, P. Simon, and P. Capak. Cars: The cfhtls-archive-research survey ii. weighing dark matter halos of lyman-break galaxies at  $z = 3 - 5$ . *Astronomy & Astrophysics*, 498(3):725–736, 2009a.

H. Hildebrandt, L. van Waerbeke, and T. Erben. Cars: The cfhtls-archive-research survey iii. first detection of cosmic magnification in samples of normal high-z galaxies. *Astronomy & Astrophysics*, 507(2):683–691, 2009b.

E. M. Huff and G. J. Graves. Magnificent Magnification: Exploiting the Other Half of the Lensing Signal. *ApJ*, 780:L16, January 2014. doi: 10.1088/2041-8205/780/2/L16.

- D. Huterer, M. Takada, G. Bernstein, and B. Jain. Systematic errors in future weak-lensing surveys: requirements and prospects for self-calibration. *MNRAS*, 366:101–114, February 2006. doi: 10.1111/j.1365-2966.2005.09782.x.
- O. Ilbert, S. Arnouts, H. J. McCracken, M. Bolzonella, E. Bertin, O. Le Fâvre, Y. Mellier, G. Zamorani, R. Pelláš, A. Iovino, L. Tresse, V. Le Brun, D. Bottini, B. Garilli, D. Maccagni, J. P. Picat, R. Scaramella, M. Scoggio, G. Vettolani, A. Zanichelli, C. Adami, S. Bardelli, A. Cappi, S. Charlot, P. Ciliegi, T. Contini, O. Cucciati, S. Foucaud, P. Franzetti, I. Gavignaud, L. Guzzo, B. Marano, C. Marinoni, A. Mazure, B. Meneux, R. Merighi, S. Paltani, A. Pollo, L. Pozzetti, M. Radovich, E. Zucca, M. Bondi, A. Bongiorno, G. Busarello, S. de La Torre, L. Gregorini, F. Lamareille, G. Mathez, P. Merluzzi, V. Ripepi, D. Rizzo, and D. Vergani. Accurate photometric redshifts for the cfht legacy survey calibrated using the vimos vlt deep survey. *Astronomy & Astrophysics*, 457:841–856, 2006.
- O. Ilbert, P. Capak, M. Salvato, H. Aussel, H. J. McCracken, D. B. Sanders, N. Scoville, J. Kartaltepe, S. Arnouts, E. Le Floc'h, B. Mobasher, Y. Taniguchi, F. Lamareille, A. Leauthaud, S. Sasaki, D. Thompson, M. Zamojski, G. Zamorani, S. Bardelli, M. Bolzonella, A. Bongiorno, M. Brusa, K. I. Caputi, C. M. Carollo, T. Contini, R. Cook, G. Coppa, O. Cucciati, S. de la Torre, L. de Ravel, P. Franzetti, B. Garilli, G. Hasinger, A. Iovino, P. Kampczyk, J.-P. Kneib, C. Knobel, K. Kovac, J. F. Le Borgne, V. Le Brun, O. Le Fèvre, S. Lilly, D. Looper, C. Maier, V. Mainieri, Y. Mellier, M. Mignoli, T. Murayama, R. Pelló, Y. Peng, E. Pérez-Montero, A. Renzini, E. Ricciardelli, D. Schiminovich, M. Scoggio, Y. Shioya, J. Silverman, J. Surace, M. Tanaka, L. Tasca, L. Tresse, D. Vergani, and E. Zucca. Cosmos photometric redshifts with 30-bands for 2-deg2. *The Astrophysical Journal*, 690(2):1236, 2009. URL <http://stacks.iop.org/0004-637X/690/i=2/a=1236>.
- O. Ilbert, P. Capak, M. Salvato, H. Aussel, E. Ricciardelli, D. Schiminovich, M. Scoggio, J. Kartaltepe, S. Arnouts, E. Le Floc'h, B. Mobasher, Y. Taniguchi, F. Lamareille,

A. Leauthaud, S. Sasaki, D. Thompson, M. Zamojski, G. Zamorani, S. Bardelli, M. Bolzonella, A. Bongiorno, M. Brusa, K. I. Caputi, C. M. Carollo, T. Contini, R. Cook, G. Coppa, O. Cucciati, S. de la Torre, L. de Ravel, P. Franzetti, B. Garilli, G. Hasinger, A. Iovino, P. Kampczyk, J.-P. Kneib, C. Knobel, K. Kovac, J. F. Le Borgne, V. Le Brun, O. Le Fèvre, S. Lilly, D. Looper, C. Maier, V. Mainieri, Y. Mellier, M. Mignoli, T. Murayama, R. Pellò, Y. Peng, E. Pérez-Montero, A. Renzini, E. Ricciardelli, D. Schiminovich, M. Scoggio, Y. Shioya, J. Silverman, J. Surace, M. Tanaka, L. Tasca, L. Tresse, D. Vergani, and E. Zucca. Cosmos Photometric Redshifts with 30-Bands for 2-deg<sup>2</sup>. *ApJ*, 690:1236–1249, January 2009. doi: 10.1088/0004-637X/690/2/1236.

Bhuvnesh Jain. Magnification effects as measures of large-scale structure. *The Astrophysical Journal Letters*, 580(1):L3, 2002. URL <http://stacks.iop.org/1538-4357/580/i=1/a=L3>.

M. Jarvis, E. Sheldon, J. Zuntz, T. Kacprzak, S. L. Bridle, A. Amara, R. Armstrong, M. R. Becker, G. M. Bernstein, C. Bennett, C. Chang, R. Das, J. P. Dietrich, A. Drlica-Wagner, T. F. Eifler, C. Gangkofner, D. Gruen, M. Hirsch, E. M. Huff, B. Jain, S. Kent, D. Kirk, N. MacCrann, P. Melchior, A. A. Plazas, A. Refregier, B. Rowe, E. S. Rykoff, S. Samuroff, C. Sánchez, E. Suchyta, M. A. Troxel, V. Vikram, T. Abbott, F. B. Abdalla, S. Allam, J. Annis, A. Benoit-Lévy, E. Bertin, D. Brooks, E. Buckley-Geer, D. L. Burke, D. Capozzi, A. Carnero Rosell, M. Carrasco Kind, J. Carretero, F. J. Castera, J. Clampitt, M. Crocce, C. E. Cunha, C. B. D’Andrea, L. N. da Costa, D. L. DePoy, S. Desai, H. T. Diehl, P. Doel, A. Fausti Neto, B. Flaugher, P. Fosalba, J. Frieman, E. Gaztanaga, D. W. Gerdes, R. A. Gruendl, G. Gutierrez, K. Honscheid, D. J. James, K. Kuehn, N. Kuropatkin, O. Lahav, T. S. Li, M. Lima, M. March, P. Martini, R. Miquel, J. J. Mohr, E. Neilsen, B. Nord, R. Ogando, K. Reil, A. K. Romer, A. Roodman, M. Sako, E. Sanchez, V. Scarpine, M. Schubnell, I. Sevilla-Noarbe, R. C. Smith, M. Soares-Santos, F. Sobreira, M. E. C. Swanson, G. Tarle, J. Thaler, D. Thomas,

A. R. Walker, and R. H. Wechsler. The des science verification weak lensing shear catalogues. *Monthly Notices of the Royal Astronomical Society*, 460(2):2245–2281, 2016. doi: 10.1093/mnras/stw990. URL <http://dx.doi.org/10.1093/mnras/stw990>.

Mike Jarvis and Bhuvnesh Jain. On combining lensing shear information from multiple filters. *Journal of Cosmology and Astroparticle Physics*, 2008(01):003, 2008. URL <http://stacks.iop.org/1475-7516/2008/i=01/a=003>.

David R Johnson, Elaine Howard Ecklund, and Anne E Lincoln. Narratives of science outreach in elite contexts of academic science. *Science Communication*, 36(1):81–105, 2014.

S. Jouvel, J.-P. Kneib, O. Ilbert, G. Bernstein, S. Arnouts, T. Dahlen, A. Ealet, B. Milillard, H. Aussel, P. Capak, A. Koekemoer, V. Le Brun, H. McCracken, M. Salvato, and N. Scoville. Designing future dark energy space missions. I. Building realistic galaxy spectro-photometric catalogs and their first applications. *A&A*, 504:359–371, September 2009. doi: 10.1051/0004-6361/200911798.

Melissa A Kenney, Jeffrey S Dukes, Karen R Lips, and Jessica J Hellmann. Engagement 2.0: increasing our collective impact. *Frontiers in Ecology and the Environment*, 14(8):403–403, 2016.

K. Kuijken. GaaP: PSF- and aperture-matched photometry using shapelets. *A&A*, 482:1053–1067, May 2008. doi: 10.1051/0004-6361:20066601.

Konrad Kuijken, Catherine Heymans, Hendrik Hildebrandt, Reiko Nakajima, Thomas Erben, Jelte T. A. de Jong, Massimo Viola, Ami Choi, Henk Hoekstra, Lance Miller, Edo van Uitert, Alexandra Amon, Chris Blake, Margot Brouwer, Axel Buddekkie, Ian Fenech Conti, Martin Eriksen, Aniello Grado, Joachim Harnois-Déraps, Ewout Helmich, Ricardo Herbonnet, Nancy Irisarri, Thomas Kitching, Dominik Klaes, Francesco La Barbera, Nicola Napolitano, Mario Radovich, Peter Schneider, Cristóbal

Sifón, Gert Sikkema, Patrick Simon, Alexandru Tudorica, Edwin Valentijn, Gijs Verdoes Kleijn, and Ludovic van Waerbeke. Gravitational lensing analysis of the kilo-degree survey. *Monthly Notices of the Royal Astronomical Society*, 454(4):3500–3532, 2015. doi: 10.1093/mnras/stv2140. URL <http://dx.doi.org/10.1093/mnras/stv2140>.

C. Laigle, H. J. McCracken, O. Ilbert, B. C. Hsieh, I. Davidzon, P. Capak, G. Hasinger, J. D. Silverman, C. Pichon, J. Coupon, H. Ausse, D. Le Borgne, K. Caputi, P. Cassata, Y.-Y. Chang, F. Civano, J. Dunlop, J. Fynbo, J. S. Kartaltepe, A. Koekemoer, O. Le Favre, E. Le Floc'h, A. Leauthaud, S. Lilly, L. Lin, S. Marchesi, B. Milvang-Jensen, M. Salvato, D. B. Sanders, N. Scoville, V. Smolcic, M. Stockmann, Y. Taniguchi, L. Tasca, S. Toft, Mattia Vaccari, and J. Zab. The cosmos2015 catalog: Exploring the  $1 < z < 6$  universe with half a million galaxies. *The Astrophysical Journal Supplement Series*, 224(2), 2016.

Tod R. Lauer. Combining undersampled dithered images. *Publications of the Astronomical Society of the Pacific*, 111(756):227, 1999. URL <http://stacks.iop.org/1538-3873/111/i=756/a=227>.

R. Laureijs, J. Amiaux, S. Arduini, J. . Auguères, J. Brinchmann, R. Cole, M. Cropper, C. Dabin, L. Duvet, A. Ealet, and et al. Euclid Definition Study Report. *ArXiv e-prints*, October 2011.

Jean-Marc Lévy-Leblond. About misunderstandings about misunderstandings. *Public Understanding of Science*, 1(1):17–21, 1992.

Mathew S. Madhavacheril, Patrick McDonald, Neelima Sehgal, and Anze Slosar. Building unbiased estimators from non-gaussian likelihoods with application to shear estimation. *Journal of Cosmology and Astroparticle Physics*, 2015(01):022, 2015. URL <http://stacks.iop.org/1475-7516/2015/i=01/a=022>.

Rachel Mandelbaum, Uros Seljak, Christopher M. Kauffmann, Guinevere and Hirata, and Jonathan Brinkmann. Galaxy halo masses and satellite fractions from galaxy-galaxy lensing in the Sloan Digital Sky Survey: stellar mass, luminosity, morphology and environment dependencies. *Monthly Notices of the Royal Astronomical Society*, 368(2):715–731, 2006. doi: 10.1111/j.1365-2966.2006.10156.x. URL <http://dx.doi.org/10.1111/j.1365-2966.2006.10156.x>.

Rachel Mandelbaum, Barnaby Rowe, Robert Armstrong, Deborah Bard, Emmanuel Bertin, James Bosch, Dominique Boutigny, Frederic Courbin, William A. Dawson, Annamaria Donnarumma, Ian Fenech Conti, Raphael Gavazzi, Marc Gentile, Mandeep S. S. Gill, David W. Hogg, Eric M. Huff, M. James Jee, Tomasz Kacprzak, Martin Kilbinger, Thibault Kuntzer, Dustin Lang, Wentao Luo, Marisa C. March, Philip J. Marshall, Joshua E. Meyers, Lance Miller, Hironao Miyatake, Reiko Nakajima, Fred Maurice Ngolé Mboula, Guldariya Nurbaeva, Yuki Okura, Stéphane Paulin-Henriksson, Jason Rhodes, Michael D. Schneider, Huanyuan Shan, Erin S. Sheldon, Melanie Simet, Jean-Luc Starck, Florent Sureau, Malte Tewes, Kristian Zarb Adami, Jun Zhang, and Joe Zuntz. Great3 results – i. systematic errors in shear estimation and the impact of real galaxy morphology. *Monthly Notices of the Royal Astronomical Society*, 450(3):2963–3007, 2015. doi: 10.1093/mnras/stv781. URL <http://dx.doi.org/10.1093/mnras/stv781>.

B. Ménard and M. Bartelmann. Cosmological information from quasar-galaxy correlations induced by weak lensing. *Astronomy & Astrophysics*, 2002(3):784–795, 2002.

Jon D Miller. The measurement of civic scientific literacy. *Public understanding of science*, 7(3):203–223, 1998.

C. B. Morrison, R. Scranton, B. Ménard, S. J. Schmidt, and J. A. Tyson. Tomographic magnification of Lyman-break galaxies in the Deep Lens Survey. *Monthly Notices of the Royal Astronomical Society*, 426:2489–2499, 2012.

National Research Council. *Astronomy and Astrophysics in the New Millennium*. The National Academies Press, Washington, DC, 2001. ISBN 978-0-309-07031-7. doi: 10.17226/9839.

National Research Council. *New Worlds, New Horizons in Astronomy and Astrophysics*. The National Academies Press, Washington, DC, 2010. ISBN 978-0-309-15799-5. doi: 10.17226/12951.

T. Pottebaum and D.G. MacMynowski. Buffeting of large telescope: Wind tunnel measurements of the flow inside a generic enclosure. *Journal of Fluids and Structures*, 22: 3–19, 2006.

B. T. P. Rowe, M. Jarvis, R. Mandelbaum, G. M. Bernstein, J. Bosch, M. Simet, J. E. Meyers, T. Kacprzak, R. Nakajima, J. Zuntz, H. Miyatake, J. P. Dietrich, R. Armstrong, P. Melchior, and M. S. S. Gill. GALSIM: The modular galaxy image simulation toolkit. *Astronomy and Computing*, 10:121–150, April 2015. doi: 10.1016/j.ascom.2015.02.002.

Barnaby Rowe, Christopher Hirata, and Jason Rhodes. Optimal linear image combination. *The Astrophysical Journal*, 741(1):46, 2011. URL <http://stacks.iop.org/0004-637X/741/i=1/a=46>.

E. Rozo and F. Schmidt. Weak Lensing Mass Calibration with Shear and Magnification. *ArXiv e-prints*, September 2010.

E. Rozo, E. S. Rykoff, A. Abate, C. Bonnett, M. Crocce, C. Davis, B. Hoyle, B. Leistedt, H. V. Peiris, R. H. Wechsler, T. Abbott, F. B. Abdalla, M. Banerji, A. H. Bauer, A. Benoit-Lévy, G. M. Bernstein, E. Bertin, D. Brooks, E. Buckley-Geer, D. L. Burke, D. Capozzi, A. Carnero Rosell, D. Carollo, M. Carrasco Kind, J. Carretero, F. J. Castander, M. J. Childress, C. E. Cunha, C. B. D’Andrea, T. Davis, D. L. DePoy, S. Desai, H. T. Diehl, J. P. Dietrich, P. Doel, T. F. Eifler, A. E. Evrard, A. Fausti Neto, B. Flaugher, P. Fosalba, J. Frieman, E. Gaztanaga, D. W. Gerdes, K. Glazebrook,

D. Gruen, R. A. Gruendl, K. Honscheid, D. J. James, M. Jarvis, A. G. Kim, K. Kuehn, N. Kuropatkin, O. Lahav, C. Lidman, M. Lima, M. A. G. Maia, M. March, P. Martini, P. Melchior, C. J. Miller, R. Miquel, J. J. Mohr, R. C. Nichol, B. Nord, C. R. O’Neill, R. Ogando, A. A. Plazas, A. K. Romer, A. Roodman, M. Sako, E. Sanchez, B. Santiago, M. Schubnell, I. Sevilla-Noarbe, R. C. Smith, M. Soares-Santos, F. Sobreira, E. Suchyta, M. E. C. Swanson, J. Thaler, D. Thomas, S. Uddin, V. Vikram, A. R. Walker, W. Wester, Y. Zhang, and L. N. da Costa. redmagic: selecting luminous red galaxies from the des science verification data. *Monthly Notices of the Royal Astronomical Society*, 461(2):1431–1450, 2016. doi: 10.1093/mnras/stw1281. URL <http://dx.doi.org/10.1093/mnras/stw1281>.

M. D. Schneider, D. W. Hogg, P. J. Marshall, W. A. Dawson, J. Meyers, D. J. Bard, and D. Lang. Hierarchical Probabilistic Inference of Cosmic Shear. *ApJ*, 807:87, July 2015. doi: 10.1088/0004-637X/807/1/87.

Ryan Scranton, Brice Ménard, Gordon T. Richards, Robert C. Nichol, Adam D. Myers, Bhuvnesh Jain, Alex Gray and Matthias Bartelmann, Robert J. Brunner, and Andrew J. Connolly. Detection of cosmic magnification with the Sloan Digital Sky Survey. *The Astrophysical Journal*, 633(2), 2005.

S. Sharma, J. Bland-Hawthorn, K. V. Johnston, and J. Binney. *Astrophysical Journal*, 730(1), 2011.

Erin S. Sheldon. An implementation of bayesian lensing shear measurement. *Monthly Notices of the Royal Astronomical Society: Letters*, 444(1):L25–L29, 2014. doi: 10.1093/mnrasl/slu104. URL <http://dx.doi.org/10.1093/mnrasl/slu104>.

Michael B Shermer. The view of science: Stephen Jay Gould as historian of science and scientific historian, popular scientist and scientific popularizer. *Social Studies of Science*, 32(4):489–524, 2002.

Charles C. Steidel, Mauro Giavalisco, Max Pettini, Mark Dickinson, and Kurt L. Adelberger. Spectroscopic confirmation of a population of normal star-forming galaxies at redshifts  $z > 3$ . *The Astrophysical Journal Letters*, 462(1):L17, 1996. URL <http://stacks.iop.org/1538-4357/462/i=1/a=L17>.

E. Suchyta, E. M. Huff, J. Aleksić, P. Melchior, S. Jouvel, N. MacCrann, A. J. Ross, M. Crocce, E. Gaztanaga, K. Honscheid, B. Leistedt, H.V. Peiris, E. S. Rykoff, E. Sheldon, T. Abbott, F. B. Abdalla, S. Allam, M. Banerji, A. Benoit-Lévy, E. Bertin, D. Brooks, D. L. Burke, A. Carnero Rosell, M. Carrasco Kind, J. Carretero, C. E. Cunha, C. B. D’Andrea, L. N. da Costa, D. L. DePoy, S. Desai, H. T. Diehl, J. P. Dietrich, P. Doel, T. F. Eifler, J. Estrada, A. E. Evrard, B. Flaugher, P. Fosalba, J. Frieman, D. W. Gerdes, D. Gruen, R. A. Gruendl, D. J. James, M. Jarvis, K. Kuehn, N. Kuropatkin, O. Lahav, M. Lima, M. A. G. Maia, M. March, J. L. Marshall, C. J. Miller, R. Miquel, E. Neilsen, R. C. Nichol, B. Nord, R. Ogando, W. J. Percival, K. Reil, A. Roodman, M. Sako, E. Sanchez, V. Scarpine, I. Sevilla-Noarbe, R. C. Smith, M. Soares-Santos, F. Sobreira, M. E. C. Swanson, G. Tarle, J. Thaler, D. Thomas, V. Vikram, A. R. Walker, R. H. Wechsler, and Y. Zhang. No galaxy left behind: accurate measurements with the faintest objects in the dark energy survey. *Monthly Notices of the Royal Astronomical Society*, 457(1):786–808, 2016. doi: 10.1093/mnras/stv2953. URL <http://dx.doi.org/10.1093/mnras/stv2953>.

M. Takada. Subaru Hyper Suprime-Cam Project. In N. Kawai and S. Nagataki, editors, *American Institute of Physics Conference Series*, volume 1279 of *American Institute of Physics Conference Series*, pages 120–127, October 2010. doi: 10.1063/1.3509247.

Charlotte Thorley. *Physicists and Outreach: Implications of schools physics outreach programmes from the perspective of the participating physicists*. PhD thesis, UCL (University College London), 2016.

R. F. J. van der Burg, H. Hildebrandt, and T. Erben. The UV galaxy luminosity function

at  $z = 3\text{--}5$  from the CFHT Legacy Survey Deep fields. *A&A*, 523:A74, November 2010. doi: 10.1051/0004-6361/200913812.

L. Van Waerbeke. Shear and magnification: Cosmic complementarity. *Monthly Notices of the Royal Astronomical Society*, 401:2093–2100, 2010.

R. C. Wolf, A. K. Romer, and B. Nord. New Science, New Media: An Assessment of the Online Education and Public Outreach Initiatives of The Dark Energy Survey. *arXiv:1804.00591*, 2018.

J. Zhang, W. Luo, and S. Foucaud. Accurate shear measurement with faint sources. *Journal of Cosmology and Astroparticle Physics*, 1:024, January 2015. doi: 10.1088/1475-7516/2015/01/024.

J. Zuntz, T. Kacprzak, L. Voigt, M. Hirsch, B. Rowe, and S. Bridle. IM3SHAPE: a maximum likelihood galaxy shear measurement code for cosmic gravitational lensing. *MNRAS*, 434:1604–1618, September 2013. doi: 10.1093/mnras/stt1125.